cigre Turkey

EISSN 2791-6049

TEPES

TURKISH JOURNAL OF ELECTRICAL POWER AND ENERGY SYSTEMS

VOLUME 3 • ISSUE 1 • FEBRUARY 2023

AVES

tepesjournal.org

cigre Turkey

TEPES
TURKISH JOURNAL OF
ELECTRICAL POWER
AND ENERGY SYSTEMS

AVES

Founder
İbrahim KARA

General Manager
Ali ŞAHİN

Finance Coordinator
Elif YILDIZ ÇELİK

Journal Managers
İrem SOYSAL
Bahar ALBAYRAK
Deniz KAYA
Irmak BERBEROĞLU

Publications Coordinators
Gökhan ÇİMEN
Arzu ARI
Alara ERGİN
Hira Gizem FİDAN
İrem ÖZMEN

Project Coordinators
Doğan ORUÇ
Sinem Fehime KOZ

Contact
Address : Büyükdere Cad. No: 105/9 Şişli, İstanbul, Turkey
Phone : +90 212 217 17 00
E-mail : info@avesyayincilik.com

cigre Turkey

TEPES
TURKISH JOURNAL OF
ELECTRICAL POWER
AND ENERGY SYSTEMS

TEPES
TURKISH JOURNAL OF
ELECTRICAL POWER
AND ENERGY SYSTEMS

AIMS AND SCOPE

Turkish Journal of Electrical Power and Energy Systems (TEPES) is an international, scientific, open access periodical published in accordance with independent, unbiased, and double-blinded peer-review principles. The journal is the official online-only publication with the support of Association of Turkish Electricity Industry (TESAB) and led by CIGRE Turkish National Committee. and it is published biannually in April and October. The publication language of the journal is English.

TEPES aims to contribute to the literature by publishing manuscripts at the highest scientific level on all fields of electrical power and energy systems. The journal publishes original research and review articles that are prepared in accordance with ethical guidelines.

The scope of the journals includes but not limited to:

1. Power Generation, Transmission and Distribution
- Conventional and renewable power generation
- Transmission systems
- Distribution Systems, automation and control
- Energy efficiency
- Electromagnetic analysis and compatibility in power systems
- HVDC and flexible AC transmission system (FACTS)
- Renewable energy technologies and system
- Transmission and distribution equipment
- Insulated cables
- Overhead lines
- Substations
- Electrical Power System Protection
- Smart-Grid
- Plasma physics and the pulsed power technology
- Information systems and telecommunication
- Electric vehicles and charging networks
- Measurement
- Power System control
- Demand Response

2. Power System Management
- Power system development and economics
- Power system operation, planning and control
- Power system environmental performance
- Power system technical performance
- Electricity markets and regulation
- Load modeling, estimation and forecast

3. High-Voltage Techniques
- Measurement systems
- Electrical materials
- Emerging test techniques
- Insulation condition and coordination in power systems
- Over-voltage, lightning protection and grounding
- Ultra-High Voltage (UHV) technologies
- Electrical installations

4. Electrical Machines
- Power electronics
- Electrical Machines and Drives
- Power transformers and reactors
- Design of Electrical Machines for Sustainable Energy Applications

TEPES is currently indexed in DOAJ, EBSCO, Gale and CNKI.

The target audience of the journal includes academicians, specialists, researchers and professionals who are working and interested in the field of electrical power and energy systems.

The editorial and publication processes of the journal are shaped in accordance with the guidelines of the Institute of Electrical and Electronics Engineers (IEEE), the World Commission on the Ethics of Scientific Knowledge and Technology (COMEST), Council of Science Editors (CSE), Committee on Publication Ethics (COPE), European Association of Science Editors (EASE), and National Information Standards Organization (NISO). The journal is in conformity with the Principles of Transparency and Best Practice in Scholarly Publishing (doaj.org/bestpractice).

Processing and publication are free of charge with the journal. No fees are requested from the authors at any point throughout the evaluation and publication process. All manuscripts must be submitted via the online submission system, which is available at www.tepesjournal.org. The journal guidelines, technical information, and the required forms are available on the journal's web page.

All expenses of the journal are covered by the CIGRE Turkish National Committee. Potential advertisers should contact the Editorial Office. Advertisement images are published only upon the Editor-in-Chief's approval.

Statements or opinions expressed in the manuscripts published in the journal reflect the views of the author(s) and not the opinions of the CIGRE Turkish National Committee, editors, editorial board, and/or publisher; the editors, editorial board, and publisher disclaim any responsibility or liability for such materials.

You can find the current version of the Instructions to Authors at https://tepesjournal.org/.

Editor in Chief: Belgin EMRE TÜRKAY
Address: Department of Electrical Engineering, İstanbul Technical University (ITU) Faculty of Electrical and Electronics Engineering, İstanbul, Turkey
E-mail: info@tepesjournal.org

Publisher: AVES
Address: Büyükdere Cad., 105/9 34394 Mecidiyeköy, Şişli, İstanbul, Turkey
Phone: +90 212 217 17 00
Fax: +90 212 217 22 92
E-mail: info@avesyayincilik.com

cigre Turkey

TEPES
TURKISH JOURNAL OF
ELECTRICAL POWER
AND ENERGY SYSTEMS

CONTENTS

*These papers are selected from CIGRE Turkey - Third Power Systems Conference (GSK 2022).

TEPES
TURKISH JOURNAL OF
ELECTRICAL POWER
AND ENERGY SYSTEMS

TEPES, Vol. 3, Issue. 1, 1, 2023

REVIEWER SUMMARY

1st – 2nd Volume Index Reviewer List

January 2021 – December 2022

Each year thousands of reviewers contribute their expertise to peer review, a process that contributes critically to the quality of the Turkish Journal of Electrical Power and Energy Systems. The editors and the authors of the papers submitted to the Turkish Journal of Electrical Power and Energy Systems are grateful for the help of all our reviewers. Here we acknowledge, with special thanks, those who reviewed between January 2021 and December 2022.

Tahir Çetin Akıncı
Alper Nabi Akpolat
İsmail Hakkı Altaş
Cenk Andıç
Saffet Ayasun
Timur Aydemir
Esra Aydın
Murat Ayanoğlu
Selva Bal
Ümmühan Başaran Filiz
Duygu Bayram
Matthias Bickermann
Yusuf Biçer
Reşat Çelikel
Melih Soner Çeliktaş
Recep Çakmak
Erkan Danacı
Mohamed Darwish
Tuğçe Demirdelen
Onur Demirel
Başak Doğru Mert
Soham Dutta
Mehmet Kubilay Eker
Ali M. Eltamaly
Lale Erdem Atılgan
Murat Fahrioğlu
R. Ganesan
istemihan Genç
Arnab Ghosh
Murat Gökçek
Murat Göl
Mehmet Gülbahçe
Sıtkı Güner
Merve Güleryüz Halaçlı
Halime Hızarcı
Suat İlhan
Murat İspirli
Ersan Kabalcı
Özcan Kalenderli
Canan Karatekin
Gülfeza Kardaş
Derya Ahmet Kocabaş
Fatih Küçüktezcan
Şule Kuşdoğan
Ahmet Merev
Fatih Mehmet Nuroğlu
Joseph S. Ojo
Yasemin Önal
Salih Barış Öztürk
Hacer Öztura
Subhranshu Padhee
Göktürk Poyrazoğlu
Mikail Pürlü
Carlos Renedo
Surender Reddy Salkuti
Reza Sirjani
Davut Solyalı
M. Cengiz Taplamacıoğlu
Ahmet Teke
Dimitrios Tsiamitros
Ayşegül Uçar
Metin Varan
Fahri Vatansever
Ding-Jiang Xue
Celal Yaşar
Cenk Yavuz
Serpil Yılmaz
Nuran Yörükeren
Emrah Zerdali

TEPES
TURKISH JOURNAL OF
ELECTRICAL POWER
AND ENERGY SYSTEMS

TEPES, Vol. 3, Issue. 1, 2-11, 2023 **DOI:** 10.5152/tepes.2022.22028

RESEARCH ARTICLE

Optimal Distributed Generation Allocation in Practical Distribution System in the Presence of Plug-in Electric Vehicles

Kola Sampangi Sambaiah

[1]Department of Electronics and Communication Engineering, PES University, School of Engineering, Karnataka, India

Cite this article as: K. S. Sambaiah, "Optimal distributed generation allocation in practical distribution system in the presence of plug-in electric vehicles," *Turk J Electr Power Energy Syst.,* 2023; 3(1), 2-11.

ABSTRACT

Due to the rising interest in sustainable transportation efforts, the adoption rate of plug-in electric vehicles (PEVs) in the transportation sector has grown significantly. However, a rise in PEVs will create an additional load demand on the electrical distribution system (EDS), which leads to increased system power loss and bus voltage deviation. Hence, the additional load must be balanced through auxiliary generation units known as distributed generation (DG) which can be integrated into EDS that minimize system power loss and bus voltage deviation. In the present study, Harris hawk's optimization technique has been implemented for optimal DG allocation in the presence of PEVs. To crisscross the feasibility of the technique, a daily load curve has been considered with various load demand patterns in a day of 24 h. The optimization technique has been implemented and tested on practical 28 – bus EDS which is in Kakdwip, West Bengal, India.

Index Terms— Distributed generation, distribution system, Harris hawk's optimization, plug-in electric vehicles, power loss minimization

I. INTRODUCTION

Currently, the world is facing various economic and environmental issues due to the increased demand for electrical energy. It was noticed that in the past few decades, due to urbanization and industrialization, this demand has been increasing in rapid phase. Since conventional power-generating stations utilize fossil fuels, greenhouse gas (GHG) is emitted causing harmful effects on the environment. However, demand for electrical energy is escalating gradually. Hence, auxiliary generation through distributed generation (DG) is one of the viable solutions for escalating electric demand. It is noticed that the appropriate allocation (location and size) of DG into the existing electric distribution system (EDS) will minimize system power loss and bus voltage deviation. However, inappropriate DG allocation will have an adverse impact on EDS. Hence, optimal DG allocation is a complex combinatorial optimization problem. Various reviews on DG allocation methods and techniques have been presented in [1–3].

Several authors used various techniques for solving DG allocation problems in EDS for power loss minimization as a major objective. Ackermann et al. have reviewed the significance and concern to give a general definition of distributed power production in competitive energy markets [4]. In the past few decades, several researchers have used various techniques to solve DG allocation problems. Initially, researchers have implemented analytical methods for solving DG allocation problems in EDS. In [5], researchers used rules of thumb also known as a golden rule or 2/3rd rule for DG allocation in an EDS. Hung et al. have implemented an analytical expression using the exact loss formula for single DG allocation and quick loss calculation in EDS [6]. Aman et al. have implemented a novel index method considering the system power stability index for DG allocation in EDS [7]. Hung et al. have implemented an analytical expression using Elgerd's loss formula for the allocation of both dispatchable and non-dispatchable renewable DG with various power factor operations [8]. Viral et al. have implemented a self-correction algorithm with reduced search space for enhancing computational speed to allocate multiple DG [9]. Ghosh et al. have developed a simple conventional search method for evaluating the cost of losses and DG [10].

In [11], researchers have used the Kalman filter algorithm and power loss sensitivity index for identifying DG size and location, respectively. In the past few years, researchers are implementing heuristic or meta-heuristic algorithms for DG allocation in distribution systems. In [12], researchers have used an artificial bee colony algorithm for DG allocation in variable loading conditions.

Corresponding author: Kola Sampangi Sambaiah, **E-mail:** sambaiahks@gmail.com

Received: September 20, 2022
Accepted: November 1, 2022
Publication Date: December 16, 2022

In [13], a bacterial foraging optimization algorithm has been used to solve DG allocation problem by considering techno-economic benefits. Sultana and Roy have implemented an oppositional krill herd algorithm for allocation of various energy sources in EDS [14]. In [15], researchers have used a bat algorithm for allocation of solar photovoltaic arrays in distribution system. Sultana et al. have used grey wolf optimizer (GWO) for multiple DG the allocation in distribution systems for loss minimization [16]. In [17], researchers have used flower pollination algorithm for allocation of different types of DGs in standard distribution systems. In [18], researchers have implemented symbiotic organisms search algorithm for power loss minimization through DG allocation. In [19], researchers have implemented ant lion optimization for the allocation of different types of DGs in standard distribution systems. Tanvar et al. evaluated techno-economic benefits of DG allocation in distribution systems using a combinational method of analytical and particle swarm optimization [20]. In [21], researchers have used whale optimization algorithm for the allocation of different types of DGs and evaluated the system reliability in standard distribution systems.

In recent years, researchers have shifted from single algorithm to combination of two or more algorithms to exchange qualities of algorithms for obtaining optimal results. In [22], researchers have implemented a combinational technique that consists of genetic algorithm and particle swarm optimization for power loss minimization through multiple DG allocation. A genetic-based tabu search technique has been implemented for renewable DG allocation in EDS [23]. Jamian et al. have implemented evolutionary particle swarm optimization which is based on ranking procedure for DG allocation [24]. Sanjay et al. have implemented hybrid GWO for multiple DG allocation in standard distribution systems [25]. In [26], researcher has implemented water cycle algorithm for solar- and wind-based generation system allocation in practical distribution systems considering power loss minimization as main objective. Venkatareddy et al. have implemented Jaya optimization algorithm for the allocation of mixed solar and wind energy source in EDS for loss minimization [27]. Several researchers have considered load on distribution systems is varying from 50% to 160%, which is linear variation. However, in practical, scenario distribution system with different loads residential, commercial, and agricultural has stochastic load variation. Hence, in the present study, stochastic nature of daily load curve of practical distribution system has been considered for more realistic feasibility of DG allocation in the presence of plug-in electric vehicles (PEVs).

Main Points

- The complex combinatorial problem of distributed generation allocation in the presence of plug-in electric vehicles has been solved using Harris hawk's optimization technique.
- The technique has been implemented and tested on practical distribution system.
- To crisscross the practicality of the technique, daily load curve has been considered with various load demand patterns in a day of 24 h.
- The present study will serve as a source for researchers and distribution network operators.

Concerns about emissions of greenhouse gas have prompted a trend toward zero-emission PEVs, which are likely to play a vital role in transforming the road transportation system. In [28], researchers have solved dynamic economic dispatch problem with PEVs charging pattern in daily load demand of 24 h using a multi-objective biogeography-based optimization. Yang et al. implemented teaching a learning-based optimization for solving similar optimization problem considering multiple PEVs integration [29]. In [30], researchers have presented relationship between penetration of PEVs and load demand increase in distribution system and solved this through effective load modeling technique. Injeti et al. have implemented a bio-inspired optimization algorithm for solving DG allocation in the presence of PEVs problem considering stochastic load demand pattern [31]. In [32, 33], researchers have discussed the impact and prospects of PEV charging pattern and energy source allocation on grid. An investigation of the barriers to the adoption of electric vehicles and vehicle-to-grid technology in India has been presented in [34]. However, it is observed from the literature that very few researchers have considered the impact of PEVs integration and DG allocation with various charging conditions.

In the present study, charging behavior of PEVs is considered for two different scenarios which are based on probability distribution of charging time. These two scenarios are evaluated through certain count of PEVs and later integrated into the load pattern of a day of the distribution system. The impact of PEVs charging behavior is evaluated. Since integration of PEVs creates additional demand on the system and deteriorates its performance, optimal DG allocation must be carried out. In the present study, a novel Harris hawk's optimization (HHO) technique has been implemented to solve the optimal DG allocation in the presence of the PEVs.

The present article is structured as a formulation of mathematical model illustrated in section II; implementation of HHO technique for optimal DG allocation in the presence of PEVs in section III analysis of system for various charging patterns of PEVs without DG allocation, section IV presents simulation results attained after optimal DG allocation using HHO, and section V presents conclusion and future directions of the current study.

II. PROBLEM FORMULATION

The practical influence of PEVs charging behavior and DG allocation into distribution system must be evaluated appropriately to avoid deterioration of power quality and system reliability.

A. Objective Function

The major objective of the current optimization problem is to minimize daily active power in the distribution system. The daily active power loss can be curtailed by minimizing active power loss index (APLI). Here, APLI is considered as the ration of daily active power loss of the system with and without DG allocation which is given as $P_{daily\ loss}^{DG}$ and $P_{daily\ loss}$, respectively.

$$OF = min\left\{APLI\right\} \tag{1}$$

$$APLI = \frac{P_{daily\ loss}^{DG}}{P_{daily\ loss}} = \frac{\sum_{t=1}^{24} P_{t,loss}^{DG}}{\sum_{t}^{24} P_{t,loss}} \tag{2}$$

where $P_{t,loss}^{DG}$ and $P_{t,loss}$ are the t^{th} hour active power loss of the system with and without DG allocation, respectively.

The power loss and voltage profile as noticed from the literature are contradictory in nature; due to this reason, in the present study, voltage deviation index (VDI) has been evaluated to check the feasibility of the technique.

$$VDI = min\sum_{t=1}^{24}\left\{\frac{V_1 - V_{t,j}}{V_1}\right\} \quad \forall j = 2,..,N_{bus} \; and \; V_1 = 1.05 \; p.u. \tag{3}$$

where $V_{t,j}$ is the bus voltage at j^{th} bus at t^{th} hour.

B. System Constraints

1) Equality Constraints

System equality constraints refer to balance of active and reactive powers.

$$P_{t,sub} + P_{t,DG} = P_{t,PEV} + P_{t,demand} + P_{t,loss} \tag{4}$$

$$Q_{t,sub} = Q_{t,demand} + Q_{t,loss} \tag{5}$$

where $P_{t,sub}$ and $Q_{t,sub}$ are the active and reactive power from the substation at t^{th} hour; $P_{t,loss}$ and $Q_{t,loss}$ are the active and reactive power loss of the system at t^{th} hour; $P_{t,demand}$ and $Q_{t,demand}$ are the active and reactive power demand at t^{th} hour; $P_{t,DG}$ power generated from DG at t^{th} hour; $P_{t,PEV}$ active load demand of PEV at t^{th} hour.

2) Inequality Constraints

The following are the inequality constraints:

$$0.95 \le V_{t,j} \le 1.05 \tag{6}$$

$$P_{min}^{DG} \le P_t^{DG} \le P_{max}^{DG} \tag{7}$$

$$Q_{min}^{DG} \le Q_t^{DG} \le Q_{max}^{DG} \tag{8}$$

III. METHODOLOGY

A. Harris Hawks' Optimization

Heidari et al. proposed a novel population-based optimization technique known as HHO. It is a nature-inspired optimization technique. The optimization technique is inspired by the hunting behavior of predatory birds which are found in the USA, especially the southern portion of Arizona lives in steady communities called Harris' hawk (Parabuteo unicinctus). These birds possess a unique cooperative behavior of foraging with other members of the family living in a similar group. However, other birds will normally discover and attacks the prey, alone. This bird desert predator demonstrates advanced team hunting abilities in tracking, surrounding (encircling), flushing out, and finally attacking the prospective prey. During the non-breeding season, these birds are smart enough to offer dinner parties for several individuals. In the raptor realm, these birds are known as genuinely cooperative predators. The team mission of these birds starts at morning twilight. These birds often sit on power poles and giant trees within their territory. The strategic moves of these birds are well-planned because they know their family team. To catch a prey, Harris' hawks use one of the seven killing strategy known as surprise pounce. During the hunt, these hawks use this intelligent strategy to detect and attack the fleeing rabbit beyond the cover from various directions and converges simultaneously. The assault may be accomplished quickly by catching the astonished victim in a few seconds, but depending on the prey's fleeing ability and habits, the seven kills may entail repeated, short-length, fast dives nearby the prey over many minutes. Harris' hawks can exhibit a range of pursuit methods depending on the complexity and a prey's fleeing habits. When the best hawk (leader) stoops at the prey and becomes disoriented, the hunt is resumed by other team members. The escaping rabbit can be confused through these alternating hunt resume behaviors. The main advantage of such cooperative tactics is that the birds can pursue the detected rabbit to exhaustion, which cannot reestablish its defensive abilities by baffling the predators. In general, among other hawks, one effective and skillful hawk will quickly catch the exhausted rabbit and shares it with the others. The main behavior of Harris' hawks can be observed from nature. The major phases of HHO are exploratory and exploitative. These phases are inspired by the different attacking strategies of Harris' hawks which are exploring a prey and surprise pounce [35].

1) Exploration Phase

In general, Harris' hawks have powerful eyes to identify and chase prey. However, sometimes, it is not easy to identify the prey. Hence, the hawks must wait and examine the desert area to identify a prey which may take several hours. In the present optimization, the candidate solutions are the hawks and the best candidate solution in every move will be taken as near optimum or intended prey. The hawks randomly sit in some locations and follow two strategies to identify a prey. In HHO, for each perching strategy, there will be an equal chance q is considered. First strategy is based on distance between position of the rabbit and other family members and the second strategy is based on perch on tall trees randomly inside the home region. These two strategies are formulated as follows:

$$Y(t+1) = \begin{cases} Y_{rand}(t) - r_1 * \left|Y_{rand}(t) - 2 * r_2 * Y(t)\right| & q \ge 0.5 \\ \left(Y_{rabbit}(t) - Y_m(t)\right) - r_3 * \left(lb + r_4 * (ub - lb)\right) & q < 0.5 \end{cases} \tag{9}$$

where $Y_m(t)$ and $Y(t+1)$ are the hawks' position vector for the present and subsequent iteration t; r_1, r_2, r_3, r_4, and q are random numbers updated in every iteration between 0 and 1; $Y_{rand}(t)$ is current population randomly chosen hawk; $Y_{rabbit}(t)$ is the prey or rabbit position; $lb \, and \, ub$ are lower and upper limits of variables; $Y_m(t)$ is the hawks' current population average position.

$$Y_m(t) = \frac{1}{N}\sum_{i=1}^{N} Y_i(t) \tag{10}$$

where $Y_i(t)$ specifies each hawk position in iteration t; N indicates overall hawks.

2) Transition from Exploration to Exploitation

The HHO algorithm transitions from exploration to exploitation and then switches between different exploitative actions depending on the prey's fleeing energy. During the escape activity, a prey's energy level drops significantly. The prey's energy to escape is modeled as:

$$E = 2 * \left(1 - \frac{t}{T}\right) * E_0 \tag{11}$$

where E is the prey's escaping energy; T is the maximum iteration number; t is the current iteration; and E_0 is prey's initial escaping energy. The value of E_0 varies from $-1 \text{ to} +1$ for two different scenarios of rabbit escaping energy. If E_0 value is decreasing from $0 \text{ to} -1$, the rabbit is physically declining. The rabbit will strengthen when E_0 value is increasing from $0 \text{ to} +1$. When the prey's fleeing strength is less than one, HHO will improve the local search for the finest choices in the vicinity.

3) Exploitation Phase

The Harris' hawks conduct the surprise pounce in this phase by attacking the target prey discovered in the previous phase. Prey, on the other hand, frequently attempts to flee from harmful circumstances. As a result, different pursuing techniques emerge in real-world settings. The HHO proposed four different ways to mimic the attacking stage based on prey fleeing behaviors and pursuit strategies of Harris' hawks. Preys are continually trying to get away from dangerous circumstances. Assume r is the probability of a prey successfully escaping $(r < 0.5)$ or unable to escape $(r \geq 0.5)$ before a surprise pounce. Irrespective of prey's trails, the hawks will engage in a harsh or soft besiege to capture it. Prey encircle is performed from various directions, softly or hardly, depending on the prey's residual energy. The prey's escaping energy (E) is utilized to simulate this strategy and allow the HHO to switch flip between the processes of soft and hard besiege. The hard besiege happens when $|E| < 0.5$ and soft besiege occurs when $|E| \geq 0.5$.

a) Soft Besiege

Soft besiege will be performed by the hawks when the rabbit is failed to escape after trying some misleading random jumps with enough energy (i.e., $r \geq 0.5 \, and \, |E| \geq 0.5$). The following rules mimic this behavior:

$$Y(t+1) = \Delta Y(t) - E * \left|J * Y_{rabbit}(t) - Y(t)\right| \tag{12}$$

$$\Delta Y(t) = Y_{rabbit}(t) - Y(t) \tag{13}$$

$$J = 2 * (1 - r_5) \tag{14}$$

where $\Delta Y(t)$ is the variation of rabbit position vector at iteration t; J is rabbit jump strength during escaping procedure; r_5 is random number between 0 and 1. The nature of rabbit moment is simulated randomly in each iteration when J value changes.

b) Hard Besiege

Hard besiege will be performed by the hawks when the rabbit has exhausted and has less energy to escape (i.e., $r \geq 0.5 \, and \, |E| < 0.5$). The hawks finally execute the surprise pounce by encircling the prey. The present locations are updated using the following equation:

$$Y(t+1) = Y_{rabbit}(t) - \left|\Delta X(t)\right| * E \tag{15}$$

c) Soft Besiege with Progressive Rapid Dives

Before the surprise pounce, a soft besiege is planned, but the rabbit can effectively escape with enough energy (i.e., $r < 0.5 \, and \, |E| \geq 0.5$). This process is further intelligent than the earlier case. In competitive circumstances when hawks wish to grab the prey, they use the skill of choosing the best possible dive.

$$A = Y_{rabbit}(t) - E * \left|J * Y_{rabbit}(t) - Y(t)\right| \tag{16}$$

Earlier dive results will be compared with current movement possible results to identify good dive among two. If it is not satisfactory (when hawks find that the rabbit is performing more misleading movements), hawks start to execute irregular, sudden, and quick dives when advancing the rabbit. For diving, hawks chose levy flight (LF) patterns as follows:

$$Z = A + LF(D) \times S \tag{17}$$

where LF is levy flight function [36]; D is problem dimension; S is $1 \times D$ sized random generated vector.

As a result, the ultimate approach for updating hawk locations during the soft besiege phase can be achieved via (18) shown below.

$$Y(t+1) = \begin{cases} A & if \, F(A) < F(Y(t)) \\ Z & if \, F(Z) < F(Y(t)) \end{cases} \tag{18}$$

Only the better location of A or Z will be chosen as the next spot in each phase. This approach is used by all search agents.

d) Hard Besiege with Progressive Rapid Dives

Before the surprise pounce, a hard besiege is planned to catch and kill the prey. The rabbit is not having sufficient energy to escape (i.e., $r < 0.5 \, and \, |E| < 0.5$). In this scenario, hawks will try to reduce the gap between them and escape prey.

As a result, the ultimate approach for updating hawk locations during the hard besiege phase can be achieved via (18). However, A and Z will be updated as follows:

$$A = Y_{rabbit}(t) - E * \left|J * Y_{rabbit}(t) - Y_m(t)\right| \tag{19}$$

$$Z = A + LF(D) \times S \tag{20}$$

B. Implementation of Harris Hawks' Optimization for Optimal Distributed Generation Allocation in the Presence of Plug-in Electric Vehicles

The sequence of steps involved to employ present optimization technique for optimal DG allocation in the presence of PEVs is given as follows:

Step 1: Initialize the algorithm parameter values (N and T are population size and maximum number of iterations, respectively) as per the requirement.

Step 2: Input the bus and line data for the load flow study program [37].

Step 3: Assign the lower and upper limit for variables (DG locations and sizes).

Step 4: With above lower and upper limits generate a solution set of random variables (search hawks).

Step 5: Using the direct approach method for load flow, evaluate the objective function for different set of randomly generated variables using equation (1).

Step 6: Identify the optimal value of the objective function through identification of best hawk position using equation (9).

Step 7: In every step, for each hawk, the values of E, E_0 and J have to be updated using (11).

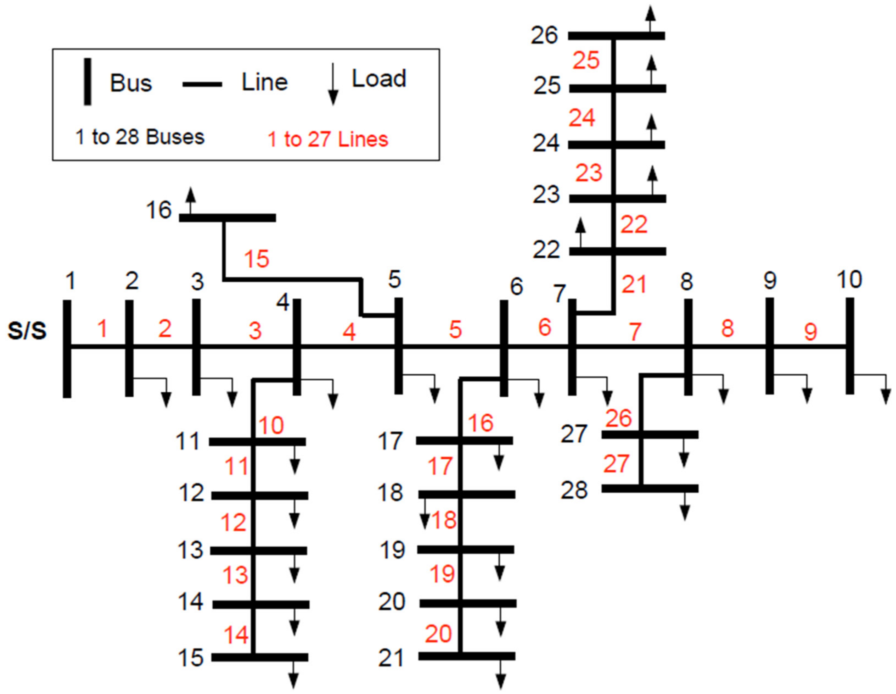

Fig. 1. Single line diagram of 28 – bus system.

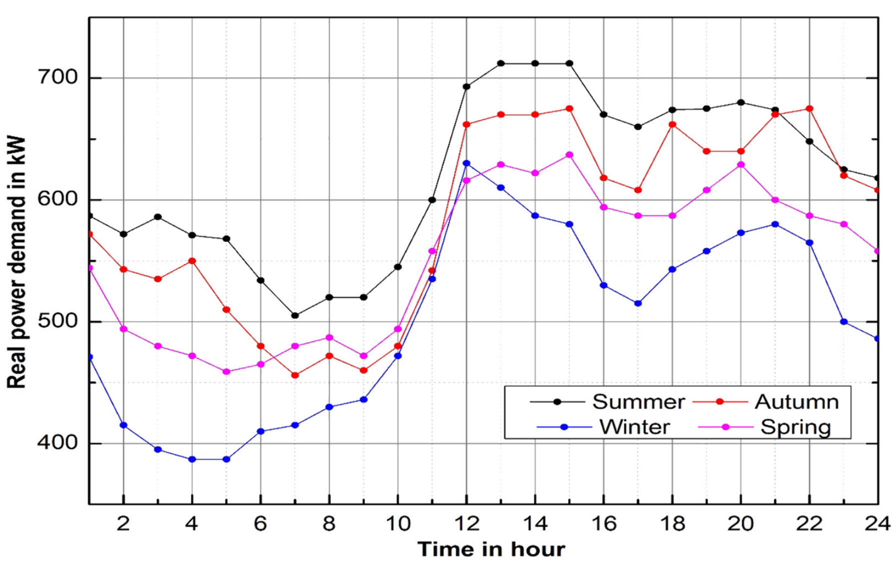

Fig. 2. Daily load demand pattern of 28 – bus system

Step 8: If $E \geq 1$, update the hawks position using , else go to next step.

Step 9: If $E \geq 0.5$, proceed to next step, else jump to step 11.

Step 10: If $r \geq 0.5$, update the hawks position using (12), else update using the equation (18) and jump to step 12.

Step 11: If $r < 0.5$, update the hawks position using (18), else update using the equation (18) and jump to step 13.

Step 12: If $E < 0.5$, update the hawks position using (16), proceed to next step, else jump to step 13.

Step 13: Check for the stopping criteria or maximum number iterations. If yes, display the values of DG location and size, else go to step 4 and repeat.

IV. RESULTS AND DISCUSSION

A practical 28 – bus distribution system which is in Kakdwip, West Bengal, India, has been considered for the analysis of the present optimization technique. The single-line diagram of the distribution

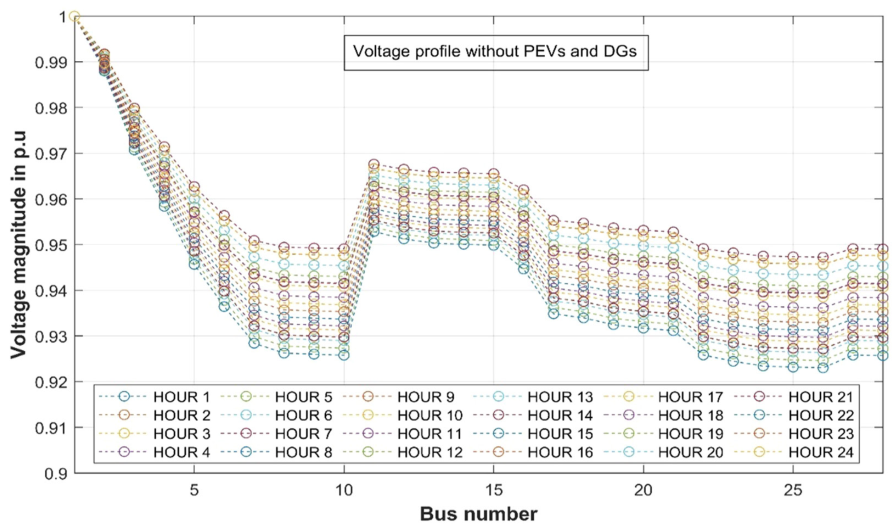

Fig. 3. Voltage profile of the system without PEVs and DGs. PEVs, plug-in electric vehicles; DG, distributed generations.

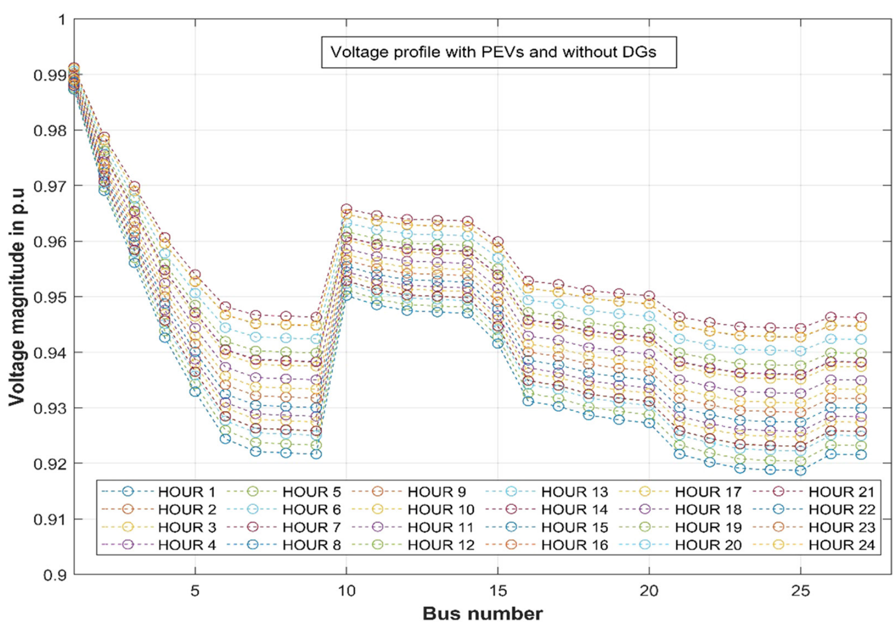

Fig. 4. Voltage profile of the system with PEVs and without DGs. PEVs, plug-in electric vehicles; DG, distributed generations.

system is illustrated in Fig. 1. The bus and line data of the system are taken from [38]. The seasonally varying load demand on the system is considered from [39]. However, for the present study, the daily load demand is considered as peak demand on the system during summer season for 24 hours as illustrated in Fig. 2. The present system has been assessed based on three different cases.

Case i: Actual system assessment without PEVs and DGs (base case);

Case ii: System assessment with PEVs and without DGs;

Case iii: System assessment with PEVs and DGs (optimal case).

A. Actual System Assessment without Plug-in Electric Vehicles and Distributed Generations (Base Case)

The present simulation has been implemented in MATLAB® version R2021b installed on laptop of Core i7 6500U CPU @ 2.5 GHz, 8GB RAM. A direct approach for distribution system load flow studies has been used for load flow analysis [37]. The total real and reactive power demand on the system is 761 kW and 776.41 kVAr, respectively. The network has maximum power demand of 947 kVA. The

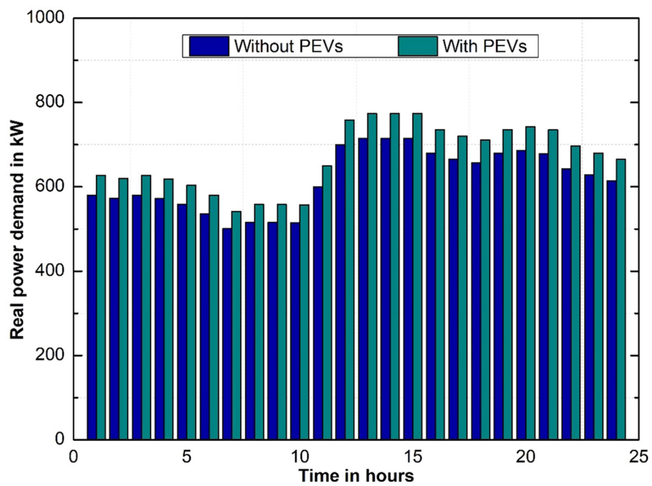

Fig. 5. Real power demand with and without PEVs. PEVs, plug-in electric vehicles.

TABLE I.
COMPARISON OF VARIOUS NETWORK PARAMETERS WITHOUT AND WITH PEVS LOAD

Network Parameter	Without PEVs	With PEVs
Daily real power demand of the system in kWh	18264	19951.5
Daily real power loss of the system in kWh	1243.44	1376.16
Minimum bus voltage in p.u.	0.9230 at 13th hour	0.9186 at 13th hour
Maximum bus voltage in p.u.	0.9917 at 9th hour	0.9912 at 7th hour

PEVs, plug-in electric vehicles.

active power loss of the system is 68.81 kW. The voltage profile of the network without PEVs and DGs is illustrated in Fig. 3.

B. System Assessment with Plug-in Electric Vehicles and without Distributed Generations

To assess the effect of PEVs addition on distribution system performance, it has been considered that each bus will have five PEVs (i.e., a total of $27 \times 5 = 135$ PEVs). However, the additional electric demand due to PEVs will be supplied by the slack bus.

TABLE II.
DAILY REAL POWER DEMAND AND LOSS ON THE SYSTEM FOR THREE DIFFERENT CASES

Time in Hour	System Without PEVs and DGs		System With PEVs and Without DGs		System With PEVs and DGs	
	Load in kW	Loss in kW	Load in kW	Loss in kW	Load in kW	Loss in kW
1	580	33.07	627.33	36.54	627.33	14.55
2	572.65	32.27	620	35.65	620	14.33
3	580	33.07	627	36.54	627	14.55
4	572	32.14	619	35.51	619	14.26
5	558	30.58	603.66	33.77	603.66	13.84
6	536	28.09	580	31.017	580	13.13
7	500.78	24.39	541.94	26.91	541.94	12.25
8	515.62	25.81	558	28.5	558	12.5
9	515.62	25.81	558	28.5	558	12.5
10	514.8	25.77	557.17	28.44	557.17	12.51
11	600	35.68	649.32	39.42	649.32	15.477
12	700	49.67	758.38	54.95	758.38	20.94
13	714.8	51.81	773.6	57.34	773.6	21.87
14	714.8	51.76	773.6	57.29	773.6	21.82
15	714.8	51.76	773.6	57.29	773.6	21.82
16	679.68	46.4	735.55	51.33	735.55	19.49
17	665.62	44.43	720.33	49.13	720.33	18.72
18	657.03	43.22	711	47.79	711	18.24
19	680	46.44	735.55	51.38	735.55	19.54
20	686	47.14	742.32	52.44	742.32	19.96
21	678.9	46.44	734.71	51.3	734.71	19.53
22	643	41.35	696.6	45.71	696.6	17.49
23	628.9	39.36	680	43.5	680	16.75
24	614.48	37.52	665.38	41.47	665.38	16.09

PEVs, plug-in electric vehicles; DG, distributed generations.

It has been considered that the penetration of low, medium, and pure battery-based PEVs are 45%, 25%, and 30%, with battery capacity of 15, 25, and 40 kWh, respectively [29]. It is also expected that the state of charge of home-returned PEVs is 50%. Hence, overall electric demand due to PEVs per bus per day is $5*(15\times0.45+25\times0.25+40\times0.30)*0.5=62.5\,kW$ and total demand for electric distribution system required per day is $62.5*27=1687.5\,kW$. The voltage profile of the network with PEVs and without DGs is illustrated in Fig. 4. The real power demand on the network without and with PEVs is illustrated in Fig. 5.

The comparison between various parameters of distribution system without and with PEVs load is presented in Table I. It can be observed that subsequent increase in the system real power demand after PEVs load integration. From Table I, it is noticed that due to the PEVs load demand of 1687.5 kW, the daily real power demand of distribution network is increased by 9%.

C. System Assessment with Plug-in Electric Vehicles and Distributed Generations (Optimal Case)

The actual real power demand on the electric distribution network has increased due to PEVs load. Hence, integration of DGs shares increased real power demand on the network. The DGs considered for allocation will inject only real power generation. For optimal DG allocation, HHO algorithm has been implemented. Table II presents the daily real power demand and loss on the system for three different cases. The voltage profile of the network with PEVs and DGs is illustrated in Fig. 6. Fig. 7 illustrates the daily real power loss variation

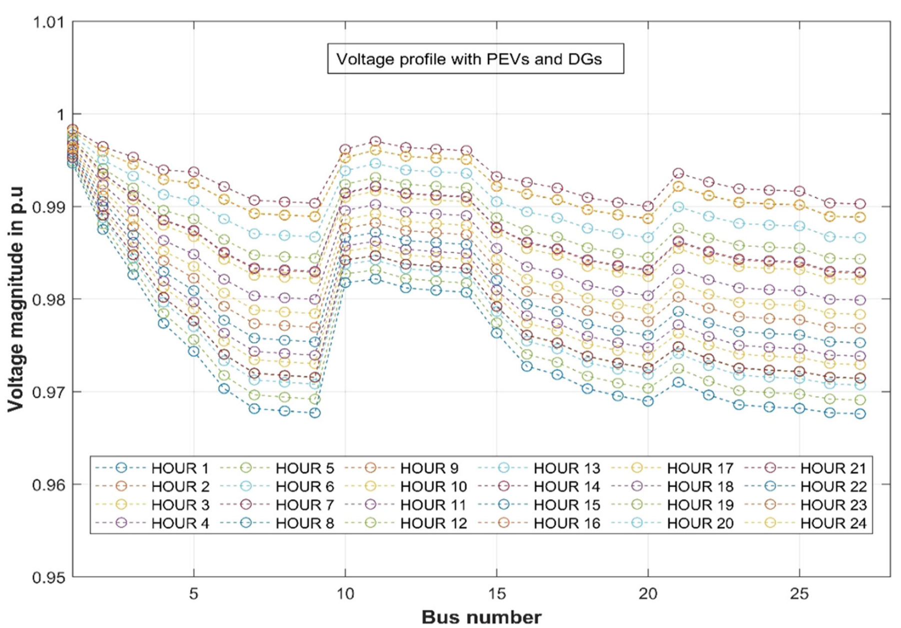

Fig. 6. Voltage profile of the system with PEVs and DGs. PEVs, plug-in electric vehicles; DG, distributed generations.

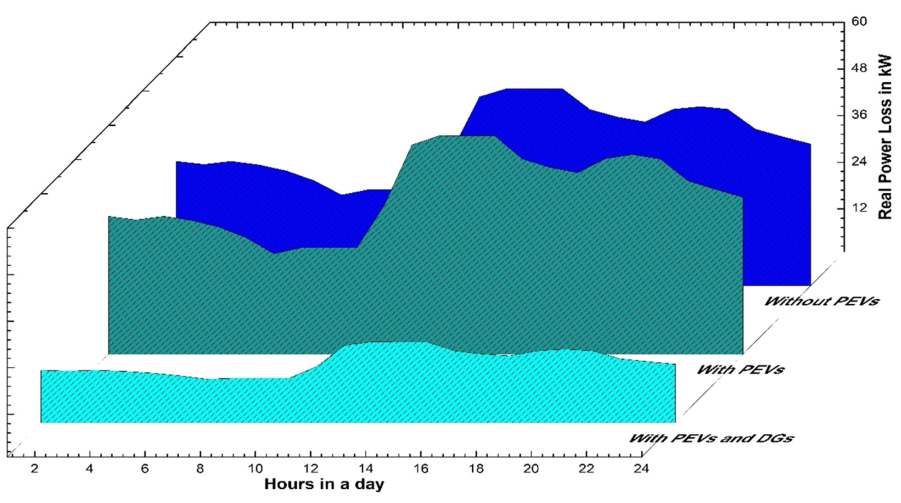

Fig. 7. Power loss reduction from base case to optimal case.

TABLE III.
OPTIMAL RESULTS OBTAINED AFTER DG INTEGRATION IN THE PRESENCE OF PEVS

Parameter	HHO
DG size in kW @ bus location	236 @ 5
	204 @ 11
	250 @ 21
Daily real power loss in kW	402.157
% Daily real power loss reduction	77.06
Minimum bus voltage in p.u.	0.9675 at 13th hour
Maximum bus voltage in p.u.	0.9983 at 7th hour

PEVs, plug-in electric vehicles; HHO, Harris hawks' optimization.

for different cases. It can be observed that the daily real power loss is increased after PEVs load and decreased when DGs are allocated appropriately in the network.

It is noticed from Table II that rise in load demand causes increase in power loss every hour for normal system and system with PEVs load. However, for system with PEVs and DGs, power loss has reduced.

Table III shows the optimal results obtained after DG allocation in the presence of PEVs. It is noticed from Table III that significant amount of power loss has been reduced from base case to optimal case of system using HHO algorithm. The minimum bus voltage has been increased from 0.9230 to 0.9675 at 13th hour. The power loss reduction from base case to optimal case can be noticed from Fig. 7.

V. CONCLUSION AND FUTURE DIRECTIONS

In the present article, a practical 28-bus Indian distribution system is considered for assessing the effect of PEVs along with DG allocation. The load pattern of daily real power demand for 24 hours is considered. The active power loss of the system is 68.81 kW. It can be observed that subsequent increase in the system real power demand after PEVs load integration is 1687.5 kW, and the daily real power demand of distribution network is increased by 9%. The objective function is framed to minimize the daily active power loss using repetitive direct approach for load flow analysis. Harris hawk's optimization algorithm is implemented to minimize the objective function. The superiority of HHO for solving the optimization problem of optimal DG allocation in practical distribution system in the presence of PEVs is discussed. It can be observed that the daily real power loss is increased after PEVs load and decreased when DGs are allocated appropriately in the network. The voltage profile of the network with PEVs and DGs has been improved. From the simulation results obtained, it is concluded that by using the HHO algorithm, the system performance is enhanced. The future direction of the work is considering PEVs simultaneously as a load and DG, with its charging and discharging habits considered during off and on peak hour demand. For further reduction of system losses and to enhance the performance, researchers can extend the vehicle to grid technology as one of the DGs to the already existing DGs.

Peer-review: Externally peer-reviewed.

Acknowledgement: The author would like to thank the management of People's Education Society (PES University), Bengaluru for supporting this research work.

Declaration of Interests: The author has no conflicts of interest to declare.

Funding: The author declared that this study has received no financial support.

REFERENCES

1. S. S. Kola, "A review on optimal allocation and sizing techniques for DG in distribution systems," *Int. J. Renew. Energy Res. (IJRER)*, vol. 8, no. 3, pp. 1236–1256, 2018.
2. I. A. Quadri, S. Bhowmick, and D. Joshi, "A comprehensive technique for optimal allocation of distributed energy resources in radial distribution systems," *Appl. Energy*, vol. 211, pp. 1245–1260, 2018. [CrossRef]
3. K. S. Sambaiah, and T. Jayabarathi, "Loss minimization techniques for optimal operation and planning of distribution systems: A review of different methodologies," *Int. Trans. Electr. Energy Syst.*, vol. 30, no. 2, p. e12230, 2020. [CrossRef]
4. T. Ackermann, G. Andersson, and L. Söder, "Distributed generation: A definition," *Electr. Power Syst. Res.*, vol. 57, no. 3, pp. 195–204, 2001. [CrossRef]
5. H. L. Willis, "Analytical methods and rules of thumb for modeling DG-distribution interaction," 2000 Power Engineering Society Summer Meeting (Cat. No. 00CH37134), vol. 3. IEEE Publications, Seattle, WA, USA; 2000, pp. 1643-1644.
6. D. Q. Hung, N. Mithulananthan, and R. C. Bansal, "Analytical expressions for DG allocation in primary distribution networks," *IEEE Trans. Energy Convers.*, vol. 25, no. 3, pp. 814–820, 2010. [CrossRef]
7. M. M. Aman, G. B. Jasmon, H. Mokhlis, and A. H. A. Bakar, "Optimal placement and sizing of a DG based on a new power stability index and line losses," *Int. J. Electr. Power Energy Syst.*, vol. 43, no. 1, pp. 1296–1304, 2012. [CrossRef]
8. D. Q. Hung, N. Mithulananthan, and R. C. Bansal, "Analytical strategies for renewable distributed generation integration considering energy loss minimization," *Appl. Energy*, vol. 105, pp. 75–85, 2013. [CrossRef]
9. R. Viral, and D. K. Khatod, "An analytical approach for sizing and siting of DGs in balanced radial distribution networks for loss minimization," *Int. J. Electr. Power Energy Syst.*, vol. 67, pp. 191–201, 2015. [CrossRef]
10. S. Ghosh, S. P. Ghoshal, and S. Ghosh, "Optimal sizing and placement of distributed generation in a network system," *Int. J. Electr. Power Energy Syst.*, vol. 32, no. 8, pp. 849–856, 2010. [CrossRef]
11. S. H. Lee, and J. W. Park, "Optimal placement and sizing of multiple DGs in a practical distribution system by considering power loss," *IEEE Trans. Ind. Appl.*, vol. 49, no. 5, pp. 2262–2270, 2013. [CrossRef]
12. F. S. Abu-Mouti, and M. E. El-Hawary, "Optimal distributed generation allocation and sizing in distribution systems via artificial bee colony algorithm," *IEEE Trans. Power Deliv.*, vol. 26, no. 4, pp. 2090–2101, 2011. [CrossRef]
13. M. Kowsalya, and Kowsalya M, "Optimal size and siting of multiple distributed generators in distribution system using bacterial foraging optimization," *Swarm Evol. Comput.*, vol. 15, pp. 58–65, 2014. [CrossRef]
14. S. Sultana, and P. K. Roy, "Oppositional krill herd algorithm for optimal location of distributed generator in radial distribution system," *Int. J. Electr. Power Energy Syst.*, vol. 73, pp. 182–191, 2015. [CrossRef]
15. S. K. Sudabattula, and K. M, "Optimal allocation of solar based distributed generators in distribution system using Bat algorithm," *Perspect. Sci.*, vol. 8, pp. 270–272, 2016. [CrossRef]

16. U. Sultana, A. B. Khairuddin, A. S. Mokhtar, N. Zareen, and B. Sultana, "Grey wolf optimizer based placement and sizing of multiple distributed generation in the distribution system," *Energy*, vol. 111, pp. 525–536, 2016. [CrossRef]
17. P. D. P. Reddy, V. C. V. Reddy, and T. G. Manohar, "Application of flower pollination algorithm for optimal placement and sizing of distributed generation in distribution systems," *J. Electr. Syst. Inf. Technol.*, vol. 3, no. 1, pp. 14–22, 2016. [CrossRef]
18. B. Das, V. Mukherjee, and D. Das, "DG placement in radial distribution network by symbiotic organisms search algorithm for real power loss minimization," *Appl. Soft Comput.*, vol. 49, pp. 920–936, 2016. [CrossRef]
19. V. C. Veera Reddy, "Ant Lion optimization algorithm for optimal sizing of renewable energy resources for loss reduction in distribution systems," *J. Electr. Syst. Inf. Technol.*, vol. 5, no. 3, pp. 663–680, 2018.
20. S. S. Tanwar, and D. K. Khatod, "Techno-economic and environmental approach for optimal placement and sizing of renewable DGs in distribution system," *Energy*, vol. 127, pp. 52–67, 2017. [CrossRef]
21. V. C. Veera Reddy, "Optimal renewable resources placement in distribution networks by combined power loss index and whale optimization algorithms," *J. Electr. Syst. Inf. Technol.*, vol. 5, no. 2, pp. 175–191, 2018.
22. M. H. Moradi, and M. Abedini, "A combination of genetic algorithm and particle swarm optimization for optimal distributed generation location and sizing in distribution systems with fuzzy optimal theory," *Int. J. Green Energy*, vol. 9, no. 7, pp. 641–660, 2012. [CrossRef]
23. M. Gandomkar, M. Vakilian, and M. J. E. P. C. Ehsan, "A genetic–based tabu search algorithm for optimal DG allocation in distribution networks," *Electr. Power Compon. Syst.*, vol. 33, no. 12, pp. 1351–1362, 2005. [CrossRef]
24. J. J. Jamian, M. W. Mustafa, and H. Mokhlis, "Optimal multiple distributed generation output through rank evolutionary particle swarm optimization," *Neurocomputing*, vol. 152, pp. 190–198, 2015. [CrossRef]
25. R. Sanjay, T. Jayabarathi, T. Raghunathan, V. Ramesh, and N. Mithulananthan, "Optimal allocation of distributed generation using hybrid grey wolf optimizer," *IEEE Access*, vol. 5, pp. 14807–14818, 2017. [CrossRef]
26. K. S. Sambaiah, "Renewable energy source allocation in electrical distribution system using water cycle algorithm," *Mater. Today Proc.*, vol. 58, pp. 20–26, 2022. [CrossRef]
27. P. Venkatareddy, K. S. Sambaiah, and S. N., "Optimal Mix and allocation of Solar and Wind Energy Sources in Active Distribution System Using Jaya Optimization Algorithm," Trends in Electrical, Electronics, Computer Engineering Conference (TEECCON). pp. 45–49, 2022. [CrossRef]
28. H. Ma, Z. Yang, P. You, and M. Fei, "Multi-objective biogeography-based optimization for dynamic economic emission load dispatch considering plug-in electric vehicles charging," *Energy*, vol. 135, pp. 101–111, 2017. [CrossRef]
29. Z. Yang, K. Li, Q. Niu, Y. Xue, and A. Foley, "A self-learning TLBO based dynamic economic/environmental dispatch considering multiple plug-in electric vehicle loads," *J. Mod. Power Syst. Clean Energy*, vol. 2, no. 4, pp. 298–307, 2014. [CrossRef]
30. K. Qian, C. Zhou, M. Allan, and Y. Yuan, "Modeling of load demand due to EV battery charging in distribution systems," *IEEE Trans. Power Syst.*, vol. 26, no. 2, pp. 802–810, 2010. [CrossRef]
31. S. K. Injeti, and V. K. Thunuguntla, "Optimal integration of DGs into radial distribution network in the presence of plug-in electric vehicles to minimize daily active power losses and to improve the voltage profile of the system using bio-inspired optimization algorithms," *Prot. Control Mod. Power Syst.*, vol. 5, no. 1, pp. 1–15, 2020.
32. H. L. Li, X. M. Bai, and W. Tan, "Impacts of plug-in hybrid electric vehicles charging on distribution grid and smart charging," In IEEE International Conference on Power System Technology (POWERCON). IEEE Publications, 2012, pp. 1–5.
33. J. Y. Yong, V. K. Ramachandaramurthy, K. M. Tan, and N. Mithulananthan, "A review on the state-of-the-art technologies of electric vehicle, its impacts and prospects," *Renew. Sustain. Energy Rev.*, vol. 49, pp. 365–385, 2015. [CrossRef]
34. K. S. Sambaiah, "A study on challenges in adoption of electric vehicle and vehicle-to grid-technologies in india," *Turk J. Electr. Power Energy Syst.*, 2022. [CrossRef]
35. A. A. Heidari, S. Mirjalili, H. Faris, I. Aljarah, M. Mafarja, and H. Chen, "Harris hawks optimization: Algorithm and applications," *Future Gener. Comput. Syst.*, vol. 97, pp. 849–872, 2019. [CrossRef]
36. G. G. Wang, "Moth search algorithm: A bio-inspired metaheuristic algorithm for global optimization problems," *Memetic Comput.*, vol. 10, no. 2, pp. 151–164, 2018. [CrossRef]
37. J. H. Teng, "A direct approach for distribution system load flow solutions," *IEEE Trans. Power Deliv.*, vol. 18, no. 3, pp. 882–887, 2003. [CrossRef]
38. D. Das, H. S. Nagi, and D. P. Kothari, "Novel method for solving radial distribution networks," *IEE Proc. Gener. Transm. Distrib.*, vol. 141, no. 4, pp. 291–298, 1994. [CrossRef]
39. P. Kayal, and C. K. Chanda, "Optimal mix of solar and wind distributed generations considering performance improvement of electrical distribution network," *Renew. Energy*, vol. 75, pp. 173–186, 2015. [CrossRef]

TEPES
TURKISH JOURNAL OF
ELECTRICAL POWER
AND ENERGY SYSTEMS

TEPES, Vol. 3, Issue. 1, 12-19, 2023 **DOI:** 10.5152/tepes.2023.22030

RESEARCH ARTICLE

Design, Optimization, and Performance Improvement of Synchronous Reluctance Motor for Micro-Mobility Vehicles

Erdal Bekiroğlu, Sadullah Esmer

Department of Electrical and Electronics Engineering, Bolu Abant İzzet Baysal University, Bolu, Turkey

Cite this article as: E. Bekiroglu and S. Esmer, "Design, optimization, and performance improvement of synchronous reluctance motor for micro-mobility vehicles," *Turk J Electr Power Energy Syst.,* 2023; 3(1), 12-19.

ABSTRACT

In this study, design, optimization, and performance improvement of a 2-kW synchronous reluctance motor (SynRM) have been performed for micro-mobility electric vehicles. The finite-element method has been used for analyses. At first, SynRM has been designed in Ansys Maxwell with initial stator and rotor parameters. Then, stator and rotor parameters of SynRM have been optimized by using a genetic algorithm. Thus, the torque capacity of SynRM has been increased and the torque ripple has been reduced. In addition, the performance of optimized SynRM has been investigated by adding magnets to its rotor. Designed SynRM and permanent magnet-supported SynRM have been compared. It has been seen that the permanent magnet-supported SynRM produces higher torque with higher efficiency and less torque ripple. Simulation results proved that the permanent magnet-supported SynRM can be used successfully in micro-mobility class electric vehicles.

Index Terms—Micro-mobility, electric vehicles, genetic algorithm, optimization, synchronous reluctance motor

I. INTRODUCTION

Nowadays, electric transportation vehicles have become one of the most popular topics. There are also many academic studies about these electric vehicles. Interest in electric vehicles is increasing to eliminate problems such as noise and chemical pollution. Micro-mobility has also been a focus of this interest, due to both the advantages of being an electric vehicle and the advantages of cost and practicality. Micro-mobility is a category that represents low-power and low-speed electric transportation vehicles. These vehicles are mostly preferred for short-distance journeys. Recently, studies on the micro-mobility electric vehicle have increased [1-6]. Some of these studies focused on the socio-economic and environmental relationship of micro-mobility class electric vehicles [2, 5], while others focused on electric motor design and control for these vehicles [3, 4], [6]. The balance between the performance expected from the electric motor in electric vehicle and its cost is very important. In addition, many parameters such as torque density, thermal limit, fault tolerance, reliability, torque ripple, longevity, and efficiency are valuable in choosing electric machines [7]. Various motor types such as permanent magnet synchronous motor (PMSM), DC motor (DCM), induction motor (IM), switched reluctance motor (SRM), and brushless DC motor (BLDC) are used in electric vehicles [8]. According to the superiority of these motors, the motor to be used in the electric vehicle is selected. The DCM has the ease of speed control, but efficiency and reliability of DCM are low because it has a brush and commutator. Magnet motors such as PMSM and BLDC have high-power factor, low torque ripple, and high efficiency. However, they have high cost and thermal limitations [9]. SRM has advantages such as simple structure, reliability, and low cost, but it has disadvantages such as low-power factor and high torque ripple [3]. IMs have the advantages of simple construction, low maintenance, and low torque ripple, but also have the disadvantage of low efficiency and low-power density [10]. Magnet motors are often used in electric vehicles, including micro-mobility. The use of magnets contributes to the improvement of motor performance, such as higher torque density and higher efficiency. However, magnets also have disadvantages such as high cost, limited availability in nature, and demagnetization due to temperature. Thus, studies in which the amount of magnets is reduced in motor design attract attention [11].

SynRM is a preferable choice for electric vehicles. SynRM has a simple and robust structure. Rotor of SynRM does not have any windings or magnets. The rotor's anisotropy structure creates the reluctance force. SynRM generates torque thanks to the reluctance force [12]. High efficiency, long life, robustness, and low cost are the advantages of SynRM. It also has disadvantages such as low-power

Corresponding author: Sadullah Esmer, **E-mail:** sadullahesmer@ibu.edu.tr

Received: December 12, 2022
Accepted: December 26, 2022
Publication Date: January 18, 2023

TABLE I.
SYNRM'S TARGETED DESIGN CRITERIA

Parameters	Values
Number of phase	3
Power (kW)	2
Speed (rpm)	650
Torque (Nm)	>8
Tork ripple (%)	<15
Efficiency (%)	>90
Maximum phase current (A)	<20
DC bus voltage (V)	48
Frequency (Hz)	50

SynRM, synchronous reluctance motor.

factor and high torque ripple [13]. Magnets are also added for performance increase in SynRM. A permanent magnet-assisted synchronous reluctance motor (PMaSynRM) has higher efficiency, torque/power density, and lower torque ripple than SynRM [14].

There are many studies in the literature about SynRMs and PMaSynRMs. In one of studies, the symmetrical and asymmetrical flux barrier structure of SynRM has been compared. A symmetrical flux barrier structure generated more stable torque than asymmetric flux barrier structure [15]. In [16], the effects of different barrier structures on SynRM's performance have been observed. In [17], the change in the performance of SynRM with the application of the skewing method in the rotor has been investigated. In [18-20], SynRM is designed for low-power and high-power electric vehicles. In [21], PMaSynRM and internal permanent magnet synchronous motor (IPMSM) for use in electric vehicles have been compared. The performances of these motors have been investigated for three different situations. In [22], a 7.5-kW PMaSynRM has been analyzed for use in light electric vehicles. In [23], PMaSynRM is designed for light electric vehicles. The designed PMaSynRM produces 1 kW of power and 12.87 Nm of torque. The designed PMaSynRM offers 91% efficiency. In [24], optimization and design of 1-kW PMaSynRM have been carried out. The effect of magnets on the performance of PMaSynRM has been investigated. Optimized PMaSynRM has 85%

Main Points

- This paper proposes the design of SynRM for use in micro-mobility electric vehicles.
- The design, optimization, and performance improvement of the proposed SynRM are presented.
- This study revealed the effects of permanent magnet on the performance of SynRM.
- The efficiency, torque, torque ripple, and power factor of the designed permanent magnet-supported SynRM have been investigated.

TABLE II.
INITIAL PARAMETERS FOR STATOR AND ROTOR OF SYNRM

Parameters	Values	Parameters	Values
Stator		Rotor	
Hs0 (mm)	0.5	H (mm)	1
Hs1 (mm)	1	W (mm)	1
Hs2 (mm)	8.2	R (mm)	1
Bs0 (mm)	2.5	R0 (mm)	10
Bs1 (mm)	10.6	Rb (mm)	15
Bs2 (mm)	12.8	Y0 (mm)	7
Rs (mm)	6.4	B0 (mm)	7
Out diameter (mm)	150	Out diameter (mm)	100
In diameter (mm)	101	In diameter (mm)	25
Length (mm)	72	Length (mm)	72

SynRM, synchronous reluctance motor.

efficiency, 12.8% torque ripple, and 11.89 Nm output torque. In [25], design and analysis have been carried out for PMaSynRM to work in two different modes. When the designed PMaSynRM is examined, it is seen that it produces 1.2 Nm torque with 62.7% efficiency at 563 rpm in washing mode. In the spinning mode, it produces 0.48 Nm torque with 83.3% efficiency at 13 krpm.

In this study, the design, optimization, and performance improvement of SynRM for micro-mobility electric vehicles were provided.

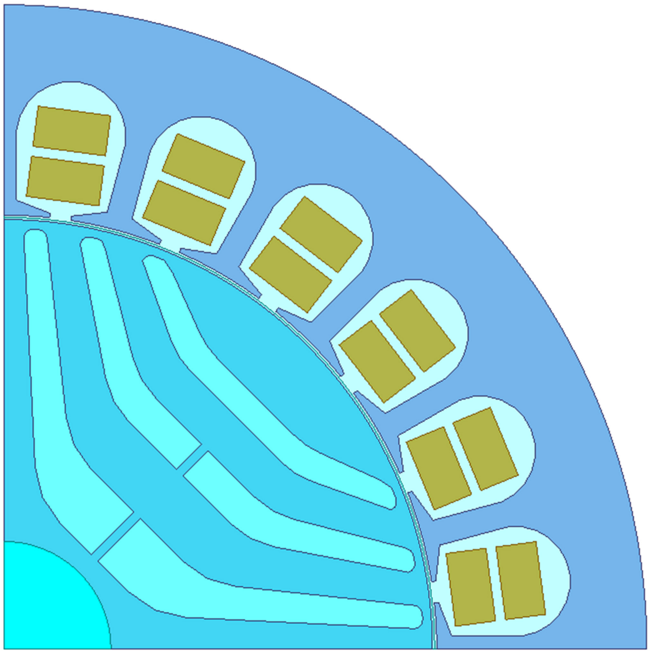

Fig. 1. Design of SynRM using initial parameters.

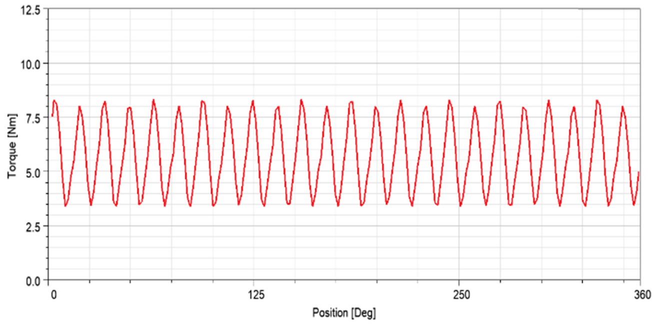

Fig. 2. Torque graph of SynRM when using the initial parameters.

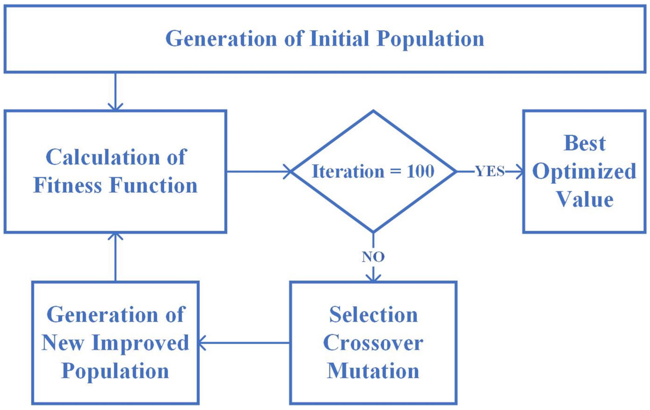

Fig. 3. Flowchart of Genetic Algorithm.

A 2-kW SynRM with three phases and four poles was optimized to meet the targeted requirements. Optimization was performed on the rotor and stator parameters of SynRM. GA has been selected for optimization. Machine Toolkit plugin in Ansys Maxwell was used to simulate the performance of permanent magnet-supported SynRM. The performance of the optimized SynRM was investigated by adding magnets to its rotor. It was observed that the efficiency and torque capability of SynRM increased, as well torque ripple decreased with magnet-supported design . The simulation results showed that the designed permanent magnet-supported SynRM offers favorable torque, efficiency, and torque ripple characteristics to be used in a micro-mobility electric vehicle.

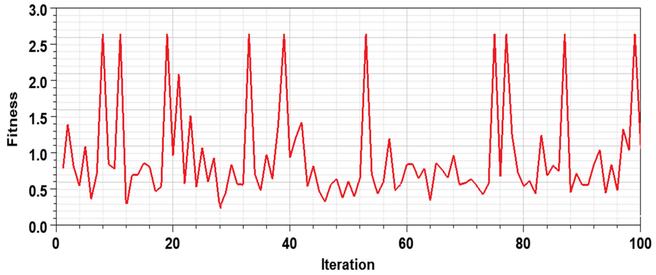

Fig. 4. Torque Ripple Graph of SynRM During Optimization Process with GA.

TABLE III.
VALUES OF OPTIMIZED PARAMETERS

Parameters	Values
Tooth width (mm)	7
Slot depth (mm)	18
Slot opening (mm)	3
First barrier thickness (mm)	3.56
First barrier angle offset (°)	4
Second barrier thickness (mm)	3.41
Second barrier angle offset (°)	4
Third barrier thickness (mm)	3.23
Third barrier angle offset (°)	4

II. DESIGN OF SYNRM

In this study, a SynRM design with high torque capability, high efficiency, and low torque ripple is aimed for micro-mobility class electric vehicles. Similar studies in the literature have been taken as reference for the characteristics of this targeted electric motor. The desired properties of the targeted SynRM are shown in Table I.

Geometric parameters such as stator and rotor are defined before the design of SynRM. SynRM's initial geometric parameters are given in Table II.

SynRM is primarily designed in Ansys Maxwell using initial parameters. SynRM has high torque ripple when designed with initial parameters. This torque ripple is approximately 80.6%. It is understood that

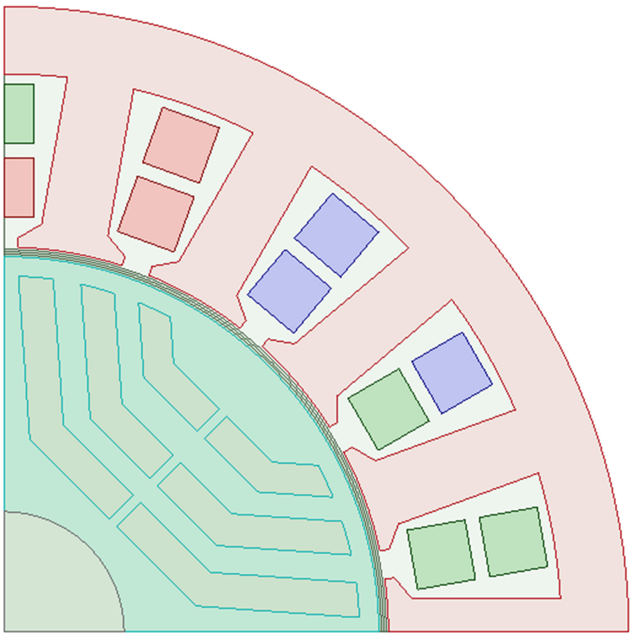

Fig. 5. Structure of SynRM with optimized stator and rotor parameters.

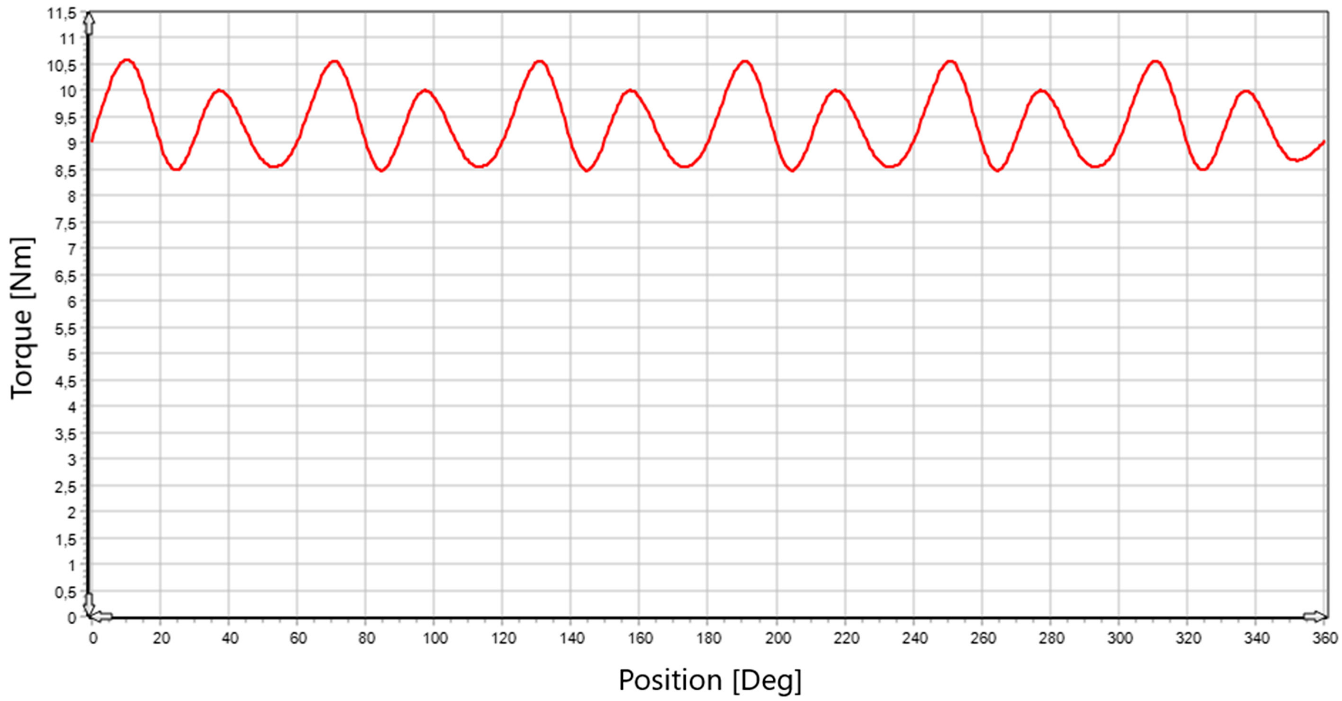

Fig. 6. Torque graph of optimized SynRM.

this torque ripple is not low enough. The average of torque produced by SynRM is 5.95 Nm. The torque is also not as high as the target torque output. The designed SynRM's structure is given in Fig. 1. The torque graph of designed SynRM is shown in Fig. 2.

III. OPTIMIZATION OF SYNRM

When SynRM is designed using initial parameters, lower performance than the targeted criteria is acquired. Therefore, it is necessary to optimize the design parameters. Optimization has been performed on geometric parameters of SynRM such as stator and rotor to meet the targeted features. In this section, it has been purposed to reach the targeted features by optimizing the parameters of SynRM. Genetic algorithm (GA) was preferred for optimization.

A. Genetic Algorithm

GA is an optimization technique that uses genetic code logic [26]. The flowchart of the GA is given in Fig. 3. This optimization purposes to find the parameters that will minimize the torque ripple. Therefore, the fitness function has been determined over the torque ripple. Torque ripple (T_{dal}) and fitness function (f_u) are given in (1) and (2), respectively.

$$T_{dal} = \frac{T_{maks} - T_{min}}{T_{ort}} \times 100 \tag{1}$$

$$f_u = min\left(T_{dal}\right) \tag{2}$$

The number of children and individuals in GA has been determined as 30. Total iteration number is 100.

Parameters to be optimized with GA are slot opening, slot depth, and tooth width for stator of SynRM, the thickness of the three flux barriers, and the barrier angle offset of the three flux barriers for the rotor of SynRM.

B. Optimization With Genetic Algorithm

Optimization with GA has been performed to reduce torque ripple and increase the torque capacity of SynRM. The optimization process

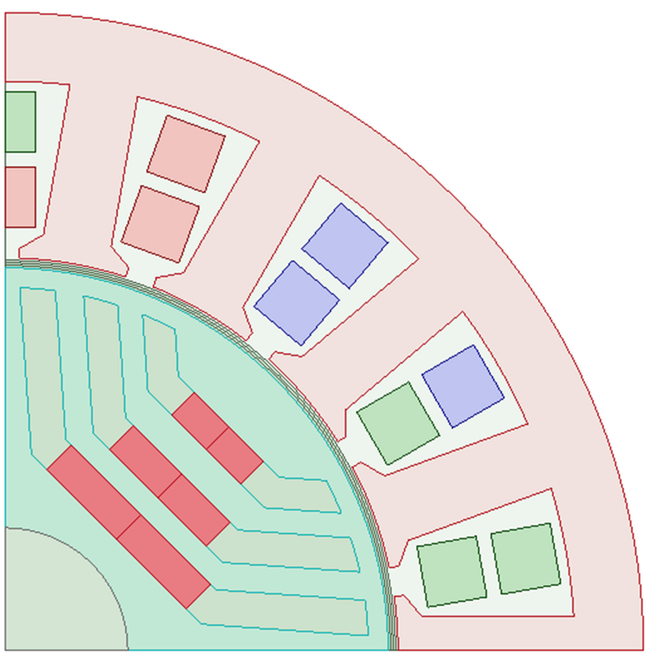

Fig. 7. Structure of permanent magnet supported SynRM.

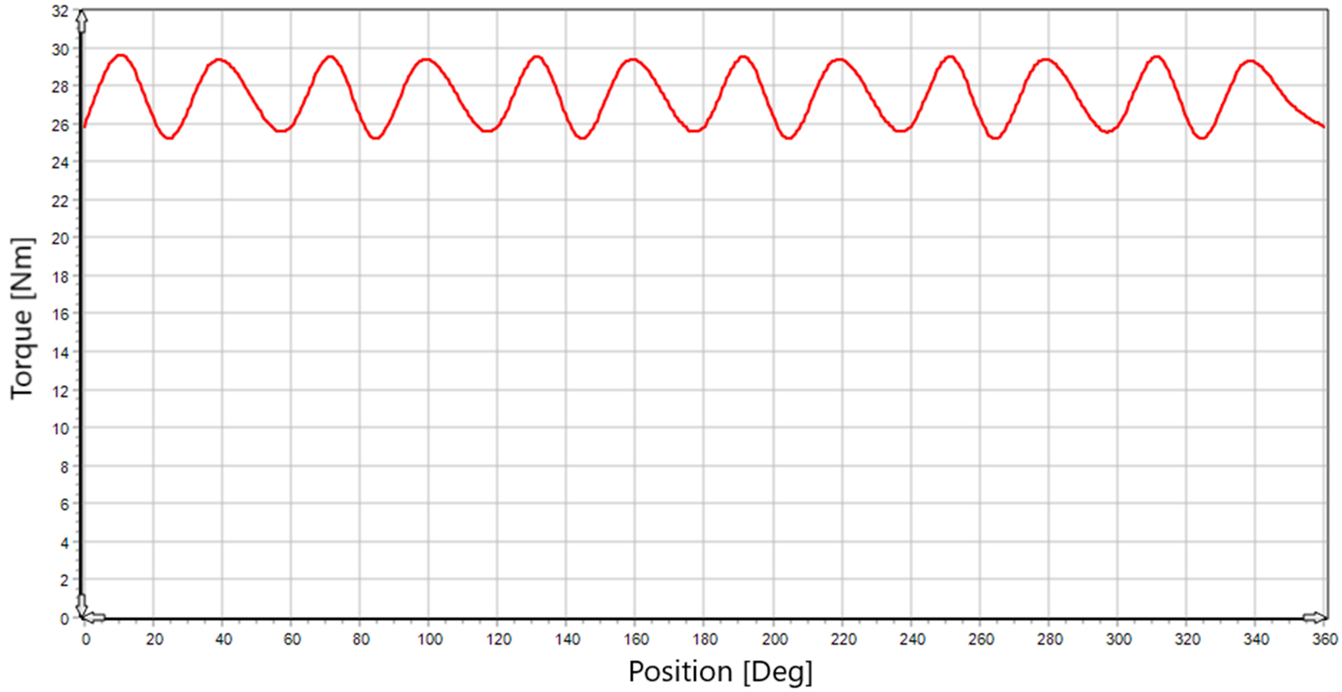

Fig. 8. Torque graph of permanent magnet supported SynRM.

with GA is shown in Fig. 4. Since the minimization of torque ripple is determined as a fitness function in GA, the lowest fitness value shows the least torque ripple. The lowest torque ripple during a total of 100 iterations was obtained at 28. The best parameters obtained with the optimization are shown in Table III.

Fig. 4 shows that the parameters optimized with GA closely affect the torque ripple of SynRM. Therefore, successfully defining stator and rotor of SynRM parameters is important for SynRM's performance. Fig. 5 shows the optimized stator and rotor structure of SynRM.

Fig. 6 shows the torque graph produced by SynRM after optimization. The average of torque produced by optimized SynRM is 9.36 Nm. According to Fig. 6, the torque ripple of optimized SynRM has been reduced to 20.95%.

IV. PERMANENT MAGNET-SUPPORTED SYNRM

The performance of the optimized SynRM is improved by adding magnets to the centers of the flux barriers in the SynRM's rotor.

TABLE IV.
TORQUE AND TORQUE RIPPLE VALUES OF SYNRM

Parameters	SynRM Without Optimization	Optimized SynRM	Permanent Magnet-Supported SynRM
Average of torque (Nm)	5.95	9.36	27.42
Torque ripple (%)	80.60	20.95	14.80

SynRM, synchronous reluctance motor.

Magnet-supported SynRM has lower torque ripple, higher efficiency, and higher torque density [14]. Magnets added to the rotor of SynRM are N35UH type magnets. The structure of magnet-supported SynRM is shown in Fig. 7.

With the addition of magnets to the rotor of the SynRM, torque density and torque ripple are improved. Thus, the torque ripple of

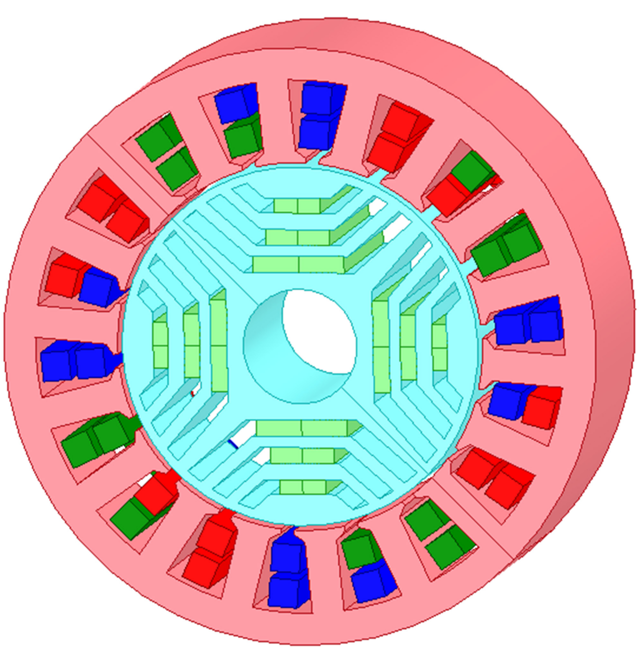

Fig. 9. Structure of the permanent magnet supported SynRM.

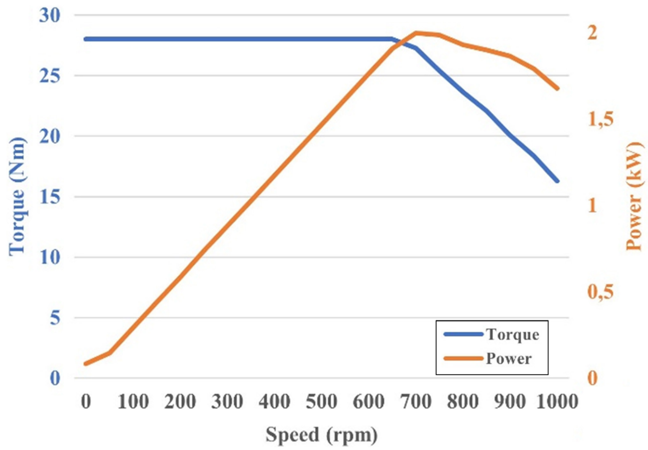

Fig. 10. Torque-speed-power graph of permanent magnet supported SynRM.

the magnet-supported SynRM has been reduced to 14.8% as can be seen in Fig. 8. The average of torque produced by magnet-supported SynRM is 27.42 Nm. Phase currents of magnet-supported SynRM have been investigated. The peak value of the currents is 20 A and the rms value of the phase currents is 14 A.

During the design of SynRM process, the highest torque and lowest torque ripple have been achieved by adding magnets to SynRM. The values of torque and torque ripple of SynRM are shown in Table IV.

V. PERFORMANCE OF THE PERMANENT MAGNET-SUPPORTED SYNRM

SynRM has advantages such as low cost, simple manufacturability, and high efficiency. However, SynRM has the disadvantage of high torque ripple [27]. However, by optimizing the stator and rotor parameters and adding magnets to the rotor, torque ripple has been significantly reduced. The structure of the performance-improved SynRM is given in Fig. 9. Permanent magnet-supported SynRM's performance has been simulated with the Machine Toolkit plugin in Ansys Maxwell. With the simulation, power factor map, power torque–speed graphics, and efficiency map of magnet-supported SynRM have been achieved.

Fig. 10 shows that the magnet-supported SynRM generates a 27.42 Nm torque up to 650 rpm. It can also produce 16–27 Nm torque between 650 rpm and 1000 rpm. The SynRM has a peak power of 2 kW, and this peak power is reached at 700 rpm.

When the SynRM is compared with the motors presented in the literature [3, 24, 25], the permanent magnet-supported SynRM has high efficiency and high torque. The efficiency of an electrical machine along the axes of speed and torque is shown on the efficiency map. For energy efficiency, it is required for an electric machine to operate at peak efficiency. However, the increase in total losses reduces the efficiency of the machine. The permanent magnet-supported SynRM's efficiency map and power factor map have been given in Fig. 11. The highest efficiency of the permanent magnet-supported SynRM has been calculated as 98.5% and the average efficiency calculated as

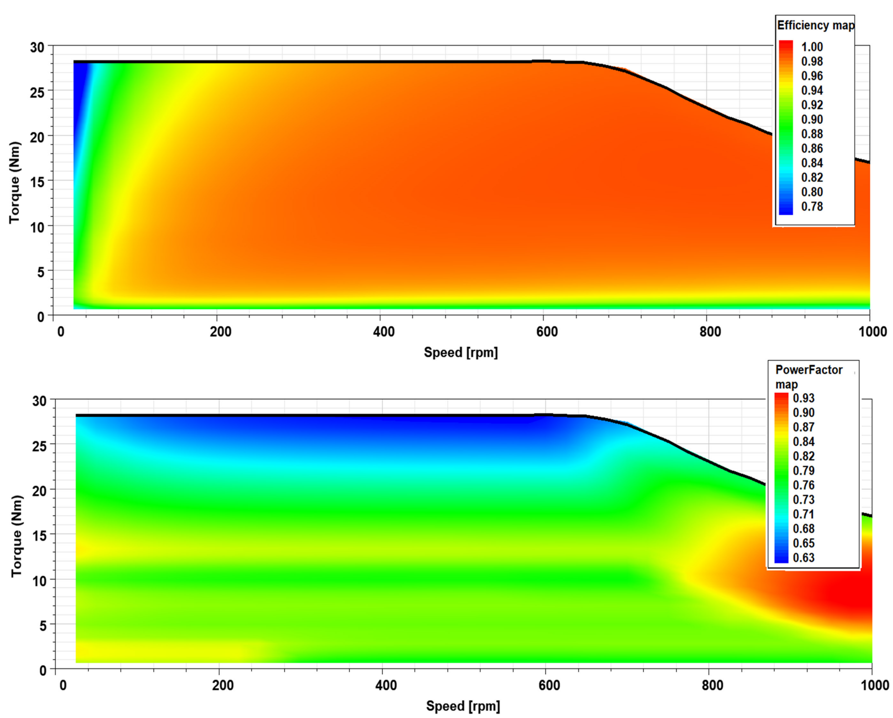

Fig. 11. Efficiency map and power factor map of permanent magnet supported SynRM.

TABLE V.
COMPARISON OF THE PROPOSED SYNRM WITH ELECTRIC MOTORS IN THE LITERATURE

	Torque (Nm)	Torque Ripple (%)	Efficiency (%)	Power (kW)
SRM [3]	8.00	64.60	–	0.3
PMaSynRM [24]	11.89	12.80	85.00	1
PMaSynRM [14]	16.68	7.10	91.65	2.2
SynRM [28]	14.10	18.00	88.90	2.2
PMSM [29]	18.00	1.30	95.71	2.2
Proposed SynRM	27.42	14.80	98.50	2

PmaSynRM, permanent magnet-assisted synchronous reluctance motor; PMSM, permanent magnet synchronous motor; SRM, switched reluctance motor; SynRM, synchronous reluctance motor.

96%. Optimization of SynRM's parameters and magnet support increased the efficiency.

The power factor shows how effectively electrical energy is used by electric motors. The designed PMaSynRM has a power factor greater than 0.8 over a wide range. Eventually, the high-power factor of SynRM enables the electric vehicle to operate more efficiently.

The analyses results show that the magnet-supported SynRM meets the targeted requirements. Table V shows a comparison of the electric motors in the literature and the proposed SynRM. It has been showed that this study offers a higher efficiency and higher torque compared with the studies presented in the literature. There are motors that produce less torque ripple than the proposed SynRM. However, it has seen that these electric motors have lower torque capability and efficiency than the proposed SynRM.

VI. CONCLUSION

In this paper, design, optimization, and performance improvement of SynRM used as an electric machine of a micro-mobility electric vehicle have been presented. SynRM is a preferable motor for electric motor in micro-mobility electric vehicles because of its high torque capability, high efficiency, and low cost, but torque ripple is a problem to be solved. Therefore, optimization of SynRM's stator and rotor parameters with GA and performance improvement by adding magnets to the rotor of the optimized SynRM has been performed in this study. Ansys Motor-Cad and Ansys Maxwell programs have been used for design and analyses. Analyses have been performed using the finite-element method. The torque speed–power graph, efficiency map, and power factor map of magnet-supported SynRM have been obtained and investigated. According to the simulation results, the highest efficiency of magnet-supported SynRM is 98.5% and the average is 96%. The results show that optimization and magnet support greatly improve the performance values of SynRM. It has been observed that the designed permanent magnet-supported SynRM produces higher torque and higher efficiency compared to the electric motors in the literature. The analyses and simulation results have demonstrated that the permanent magnet-supported SynRM successfully provides the targeted efficiency, torque ripple, and torque. The results pointed out that the permanent magnet-supported SynRM is practicable and effective for micro-mobility electric vehicle.

Peer-review: Externally peer-reviewed.

Declaration of Interests: The author has no conflicts of interest to declare.

Funding: The author declared that this study has received no financial support.

REFERENCES

1. E. Bekiroğlu, and S. Esmer, "Design and optimization of synchronous reluctance motor for micro-mobility vehicles," Power Systems Conference III. Ankara, 2022.
2. H. Güldür, F. Karaçor, S. Hatipoglu, and K. Cubuk, "A new mode of urban transportation: E-scooter and suggestions for application Türkiye," *Gazi Mühendislik Bilim Derg.*, vol. 8, no. 1, pp. 60–73, 2022. [CrossRef]
3. S. Koyuncu, U. Tuncer, A. Dalcali, and S. Oncu, "External rotor 6/8 switched reluctance motor design for E-bike; external rotor 6/8 switched reluctance motor design for E-Bike," 10th Int. Conf. Renew. Energy Res. Appl., vol. 2021, 2021. [CrossRef]
4. A. K. Mishra, B. S. Rajpurohit, and R. Kumar, "Revampment of surface permanent magnet synchronous motor design for ameliorated torque profile in e-mobility applications,", *IET Electrical Syst. in Trans.*, vol. 11, no. 2, pp. 99–108, 2021. [CrossRef]
5. R. L. Abduljabbar, S. Liyanage, and H. Dia, "The role of micro-mobility in shaping sustainable cities: a systematic literature review," *Transp. Res. D*, vol. 92, 2021. [CrossRef]
6. B. Poudel, T. Watson, and W. Li, "Learning to control DC motor for micromobility in real time with reinforcement learning," 25th Int. Conf. Intell. Transp. Syst. IEEE Publications, 2022, pp. 1248–1254. [CrossRef]
7. L. Shao, A. E. H. Karci, D. Tavernini, A. Sorniotti, and M. Cheng, "Design approaches and control strategies for energy-efficient electric machines for electric vehicles—A review" *IEEE Access*, vol. 8, pp. 116900–116913, 2020. [CrossRef]
8. H. Kaymaz, and M. F. Demir, "Elektrikli otomobiller için çekiş motor tip seçimi," *Marmara Univ.*, vol. 2, no. 1, pp. 35–41, 2020. [CrossRef]
9. W. Cai, X. Wu, M. Zhou, Y. Liang, and Y. Wang, "Review and development of electric motor systems and electric powertrains for new energy vehicles," *Automot. Innov.*, vol. 4, no. 1, pp. 3–22, 2021. [CrossRef]
10. G. Pellegrino, A. Vagati, B. Boazzo, and P. Guglielmi, "Comparison of induction and PM synchronous motor drives for EV application including design examples," *IEEE Trans. Ind. Appl.*, vol. 48, no. 6, pp. 2322–2332, 2012. [CrossRef]
11. J. D. Widmer, R. Martin, and M. Kimiabeigi, "Electric vehicle traction motors without rare earth magnets," *Sustain. Mater. Technol.*, vol. 3, pp. 7–13, 2015. [CrossRef]
12. M. A. Kabir, and I. Husain, "Application of a multilayer AC winding to design synchronous reluctance motors," *IEEE Trans. Ind. Appl.*, vol. 54, no. 6, pp. 5941–5953, 2018. [CrossRef]
13. M. Murataliyev, M. Degano, M. Di Nardo, N. Bianchi, and C. Gerada, "Synchronous reluctance machines: A comprehensive review and technology comparison," *Proc. IEEE*, vol. 110, no. 3, pp. 382–399, 2022. [CrossRef]
14. S. Jia, P. Zhang, D. Liang, M. Dai, and J. Liu, "Design and comparison of three different types of IE4 efficiency machines," 22nd Int. Conf. Electr. Mach. Syst. ICEMS, 2019. [CrossRef]

15. M. Sanada, K. Hiramoto, S. Morimoto, and Y. Takeda, "Torque ripple improvement for synchronous reluctance motor using asymmetric flux barrier arrangement," Conf. Rec. - IAS Annu. Meet. IEEE Ind. Appl. Soc., vol. 1, 2003, pp. 250–255. [CrossRef]
16. N. Bianchi, S. Bolognani, D. Bon, and M. D. Pré, "Rotor flux-barrier design for torque ripple reduction in synchronous reluctance and PM-assisted synchronous reluctance motors," *IEEE Trans. Ind. Appl.*, vol. 45, no. 3, pp. 921–928, 2009. [CrossRef]
17. P. Lazari, J. Wang, and B. Sen, "3-D effects of rotor step-skews in permanent magnet-assisted synchronous reluctance machines," *IEEE Trans. Magn.*, vol. 51, no. 11, pp. 1–4, 2015.
18. J.-C. Son, J.-M. Ahn, J. Lim, and D.-K. Lim, "Optimal design of PMa-SynRM for electric vehicles exploiting adaptive-sampling kriging algorithm," *IEEE Access*, vol. 9, pp. 41174–41183, 2021. [CrossRef]
19. D. B. Herrera, E. Galvan, and J. M. Carrasco, "Synchronous reluctance motor design based EV powertrain with inverter integrated with redundant topology," *IECON*, vol. 2015, pp. 3851–3856, 2015. [CrossRef]
20. D. Herrera, J. Villegas, E. Galvan, and J. M. Carrasco, "Powertrain EV synchronous reluctance motor design with redundant topology with novel control," *IET Electr. Power Appl.*, vol. 13, no. 11, pp. 1647–1659, 2019. [CrossRef]
21. S. Rawat, and K. R. R., "Electrical parametric design of permanent magnet machine for high power urban electric vehicles,". Motion Control. Conf. IEEE Publications, 2022, pp. 639–647. [CrossRef]
22. A.-M. Nicorici, C. Oprea, and C. Martis, "Performance evaluation of a 7.5 kW permanent magnet assisted synchronous reluctance machine for light electric vehicles," Int. Conf. Expo. Electr. Power Eng., 2018, pp. 129–132. [CrossRef]
23. A. Bozkurt, A. F. Baba, and Y. Oner, "Design of outer-rotor permanent-magnet-assisted synchronous reluctance motor for electric vehicles," *Energies*, vol. 14, no. 13, 2021. [CrossRef]
24. I. P. Abeyrathne, M. S. Toulabi, S. Filizadeh, and A. M. Gole, "Performance enhancement of a SynRM and PMaSynRM using a Cartesian coordinates-based rotor design optimization," 24th Int. Conf. Electr. Mach. Syst., 2021, pp. 1429–1434. [CrossRef]
25. A. Tap, L. Xheladini, M. Yılmaz, M. Imeryuz, T. Asan, and L. T. Ergene, "Comprehensive design and analysis of a PMaSynRM for washing machine applications," *IET Electr. Power Appl.*, vol. 12, no. 9, pp. 1311–1319, 2018. [CrossRef]
26. K. F. Man, K. S. Tang, and S. Kwong, *Genetic Algorithms*, 1st ed. London: Springer, 1999.
27. J. C. Li, M. Xin, Z. N. Fan, and R. Liu, "Design and experimental evaluation of a 12 kW large synchronous reluctance motor and control system for elevator traction," *IEEE Access*, vol. 8, pp. 34256–34264, 2020. [CrossRef]
28. N. G. Ozcelik, U. E. Dogru, M. Imeryuz, and L. T. Ergene, "Synchronous Reluctance Motor vs. induction Motor at Low-Power Industrial Applications: Design and Comparison," *Energies*, vol. 12, no. 11, p. 2190, 2019. [CrossRef]
29. H. Yetiş, and T. GÖKTAŞ, "'Comparative design of permanent magnet synchronous motors for low-power industrial applications,' *balk*," *J. Electr. Comput. Eng.*, vol. 8, no. 3, pp. 218–224, 2020.

cigre Turkey

TEPES
TURKISH JOURNAL OF
ELECTRICAL POWER
AND ENERGY SYSTEMS

TEPES, Vol. 3, Issue. 1, 20-27, 2023 **DOI:** 10.5152/tepes.2023.22031

RESEARCH ARTICLE

Investigation of the Effect of Corona Ring Design Parameters on Electric Field Distribution by Finite Element Method

Mete Uzar[1], Yunus Berat Demirol[2], Mehmet Aytaç Çınar[3], Bora Alboyacı[4]

[1]TEİAŞ (Turkish Electricity Transmission Corporation), Operations Department, Ankara, Turkey
[2]Genetek Güç, Enerji Ltd. Şti., Kocaeli University Technopark, Kocaeli, Turkey
[3]Department of Occupational Health and Safety, Kocaeli University, Izmit Vocational School, Kocaeli, Turkey
[4]Department of Electrical Engineering, Kocaeli University, Faculty of Engineering, Kocaeli, Turkey

Cite this article as: M. Uzar, Y. B. Demirol, M. A. Çınar and B. Alboyacı, "Investigation of the effect of corona ring design parameters on electric field distribution by finite element method," *Turk J Electr Power Energy Syst.*, 2023; 3(1), 20-27.

ABSTRACT

Insulators and auxiliary equipment are used to provide electrical isolation in energy transmission. The high electric field distribution on the composite insulators causes a decrease in the hydrophobicity and increases the aging of the insulator over time. Corona rings are used to balance the electric field distribution with insulators. The corona rings used are designed according to thickness, diameter, and height parameters. In this study, the design parameters of the corona ring used in composite insulators are evaluated by finite element analysis. In this context, different types of corona rings were modeled in real scale in the computer environment and transferred to the Ansys Electronics Suite finite element software program. Analyses were performed with appropriate analysis settings and material definitions. Different design parameters were examined in the analysis, and the results were interpreted and shown in detail in the article. As a result, the necessity of system evaluation with finite element analyses in designing insulation systems used in energy transmission has been demonstrated.

Index Terms—Composite insulator, corona ring, electric field, finite element analysis

I. INTRODUCTION

High-voltage insulators are used in overhead lines to provide isolation between poles and conductors. Insulators used in high voltage can be manufactured using porcelain, glass, or composite material. Insulators made of composite material have advantages such as lightness, flexibility, dirt repellent, impact, and pressure resistance. One of the most important parameters for composite insulators is hydrophobicity. It provides better insulation properties, especially in dirty and humid environmental conditions, compared to other insulator types [1]. However, the continuous corona discharge observed on the insulator surface or at the metal junctions close to the insulator surface causes a decrease in the hydrophobic property of the composite insulator.

The loss of the composite insulator's hydrophobic property is considered the insulator's aging. For this reason, the electric field strength in the critical areas for the composite insulator should always be kept under control. In addition, partial discharge due to high electric field distribution causes local heating in equipment [2]. In order not to cause aging of the composite insulator by losing its hydrophobic property, the maximum electric field strength values for the outer surface in contact with the air are limited but have been examined in some studies. According to Council on Large Electric Systems (CIGRE) brochure 284, published in 2005, it should be 6–10 kV/cm [3]. It is stated as 4.5 kV/cm [4] for the Electric Power Research Institute (EPRI), which published its studies in 2008, and 3.5 kV/cm [5] for (independent laboratory specializing in high voltage testing (STRI), which published its investigations in 2011. As a result of artificial aging experiments, it is stated that these values can change according to different weather conditions [6].

Corona ring is used to limit the electric field distribution on the surfaces of the endpoints of the composite insulator [7]. The electric field distribution on the composite insulator surface changes according to the design parameters of the corona ring used. In addition, the electric field distribution formed on the surface of the corona ring is also an important parameter. Corona discharge may occur due to high electric field distribution on the surface of the corona ring,

Corresponding author: Yunus Berat Demirol, **E-mail:** yunusberat.demirol@genetek.com.tr

Received: December 15, 2022
Accepted: December 29, 2022
Publication Date: February 9, 2023

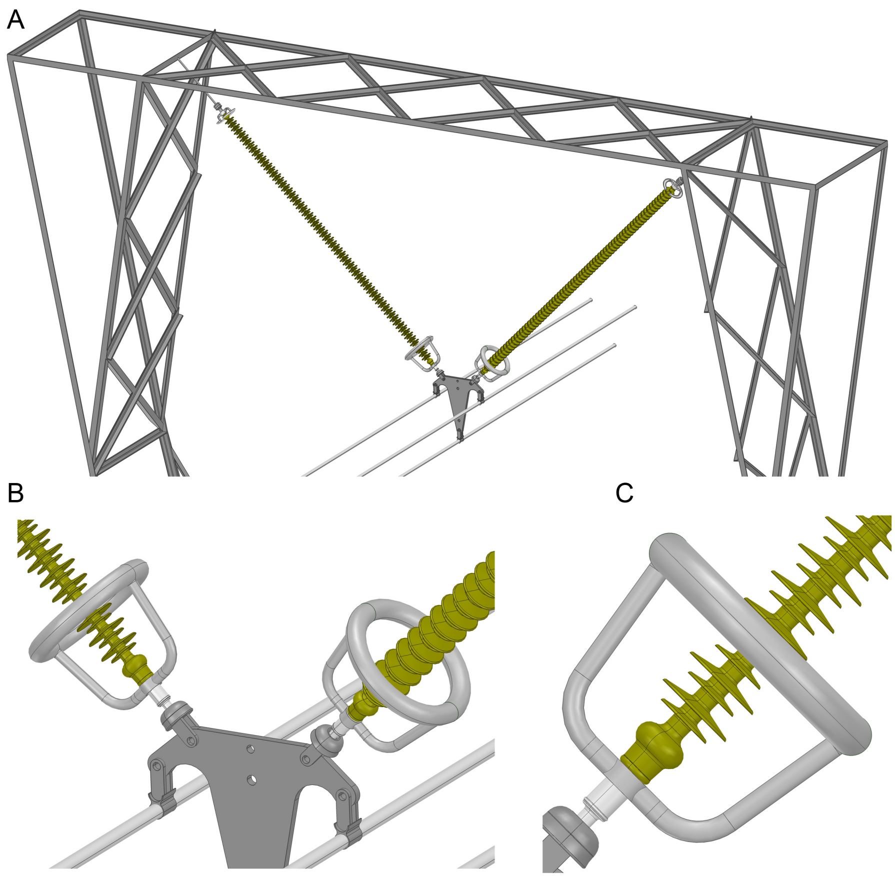

Fig. 1. Three-dimensional model of the isolation system. (a) Pole-insulator structure. (b) Corona ring view-1. (c) Corona ring view-2.

which is in a metal structure. In this context, various studies have been carried out in the literature regarding the maximum electric field distribution that can occur on the surface of metal components. Accordingly, it is recommended that the electric field on metal surfaces be at most 18 kV/cm for STRI [5].

There are various studies on the corona ring design in the literature. In [8], the design parameters of the corona rings used in glass insulators were evaluated together with analysis studies, and field tests and inferences for optimization were made. In [9–11], the effects of the design parameters of the corona rings on the electric field distribution formed on the composite insulator surface were investigated. In [12], the isolation performances of the corona rings used in composite insulators were tested in a laboratory environment. In [13], the effect of the design parameters of the glass insulator and the corona ring on the electric field distribution was evaluated together. In [14], the applications of adding glass insulators to composite insulators and using the corona ring were assessed.

Main Points

- The effect of the corona ring design parameters on the electric field distribution has been investigated.
- Corona ring design parameters are critical and decisive in the design of the high voltage insulation system.
- The electric field distribution on the composite insulator and the corona ring surface decreases when the metal diameter increases.
- As the diameter increases, the electric field distribution becomes more balanced.
- The height of the corona ring affects the maximum electric field distribution and the form of the field distribution.

In this study, the composite insulator system was modeled, and the electric field intensities on both the composite insulator surface and

TABLE I.
COMPOSITE INSULATOR PROPERTIES

Lightning impulse withstand voltage	**>1665 kV**
System frequency withstand voltage	>680 kV
Creep distance	10 570 mm
Arc distance	3040 mm
Mechanical load resistance	210 kN
Total number of pods	135

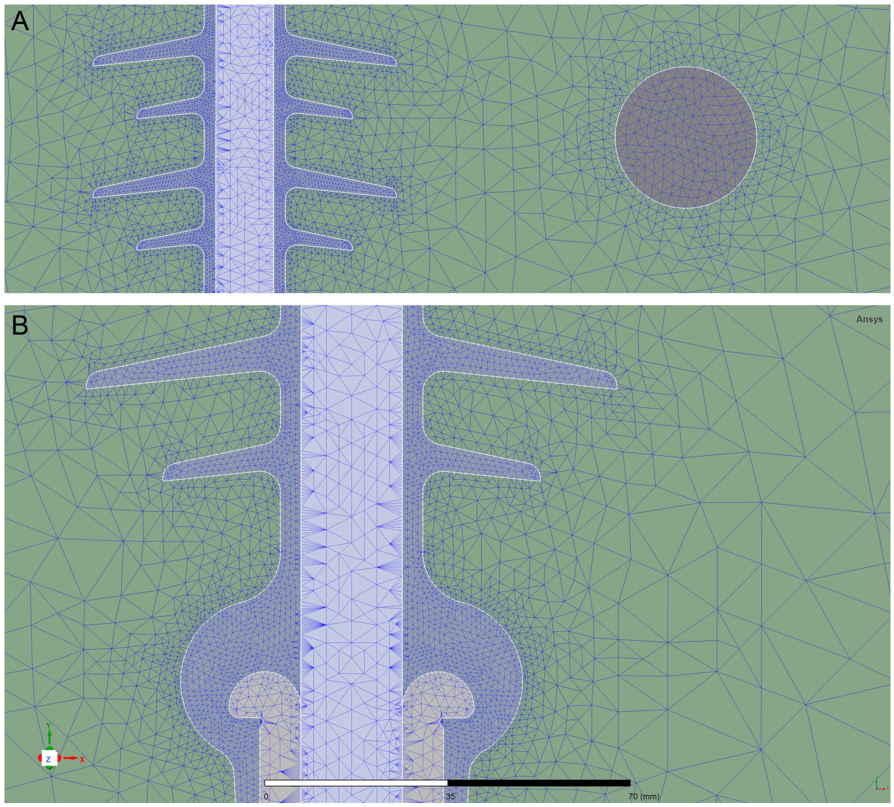

Fig. 2. Mesh structure created in the models: (a) view-1 and (b) view-2.

the corona ring surface were evaluated according to different design parameters.

In this context, the effect of the corona ring design parameters on the electric field distribution has been investigated. For this purpose, composite insulator system with corona ring is modeled in real scale in computer environment. Then, with Ansys Electronics suite finite element software, parametric analysis studies were carried out. It is seen that these analyzes are critical and decisive in the design of the corona ring.

In this context, the properties of the composite insulator and the corona ring are shown in section-II. Then, modeling studies are explained. In section-III, the investigated parameters of the corona ring are shown. The analysis results according to the change of three different design parameters are explained in the figures. Finally, an

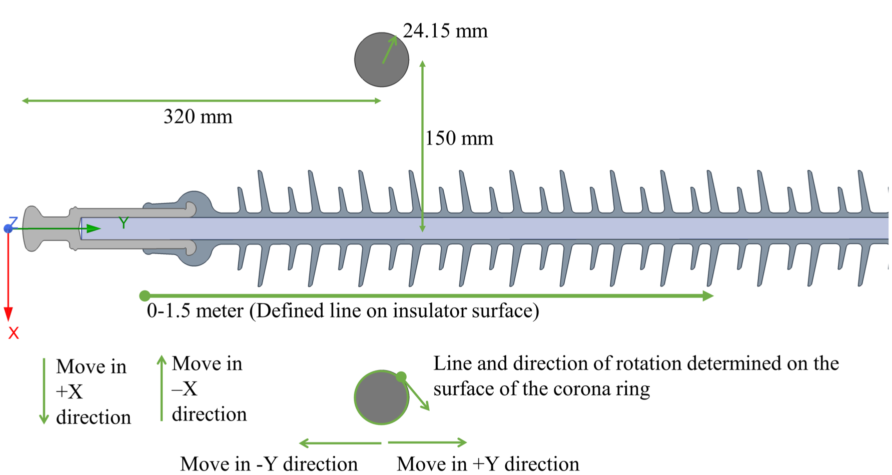

Fig. 3. Corona ring parameters.

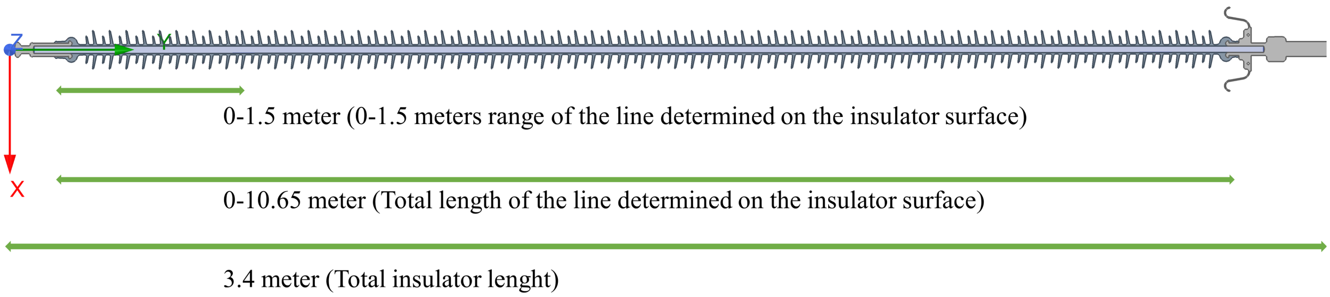

Fig. 4. Composite insulator dimensions.

analysis study was conducted in which all design parameters were evaluated together. The results obtained in the conclusion section are shown comparatively.

II. MODELING METHODS

Theoretical methods for electric field calculations are insufficient due to the complex geometrical structure of power system equipment. In this context, numerical methods such as the finite element method can be used. With the finite element method, a finite number of mesh structures are created on the relevant geometry, and Maxwell's equations are solved on this mesh structure. Ansys Electronics Suite finite element software was used in this study. In order to perform analyses in the finite element software, model geometries must be created, and appropriate material definitions must be made. The

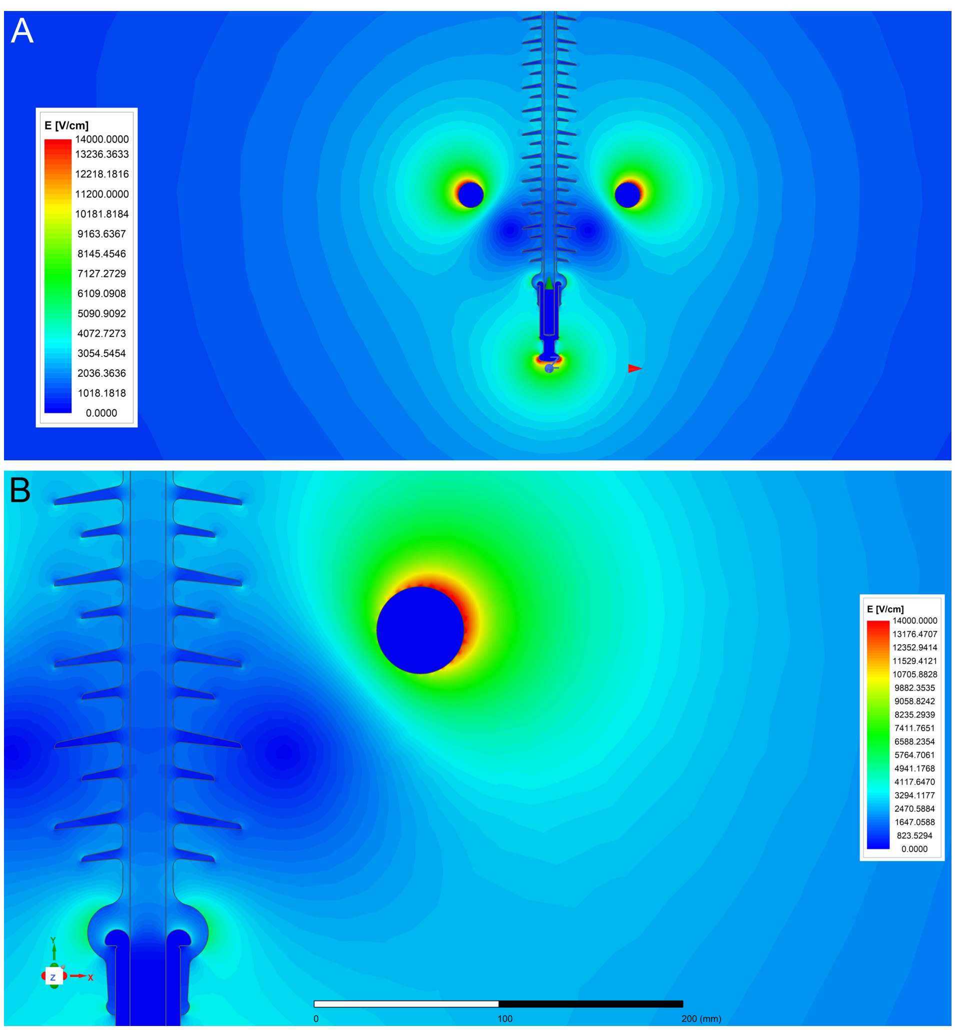

Fig. 5. Electric field distribution occurred in the reference design: (a) view-1 and (b) view-2.

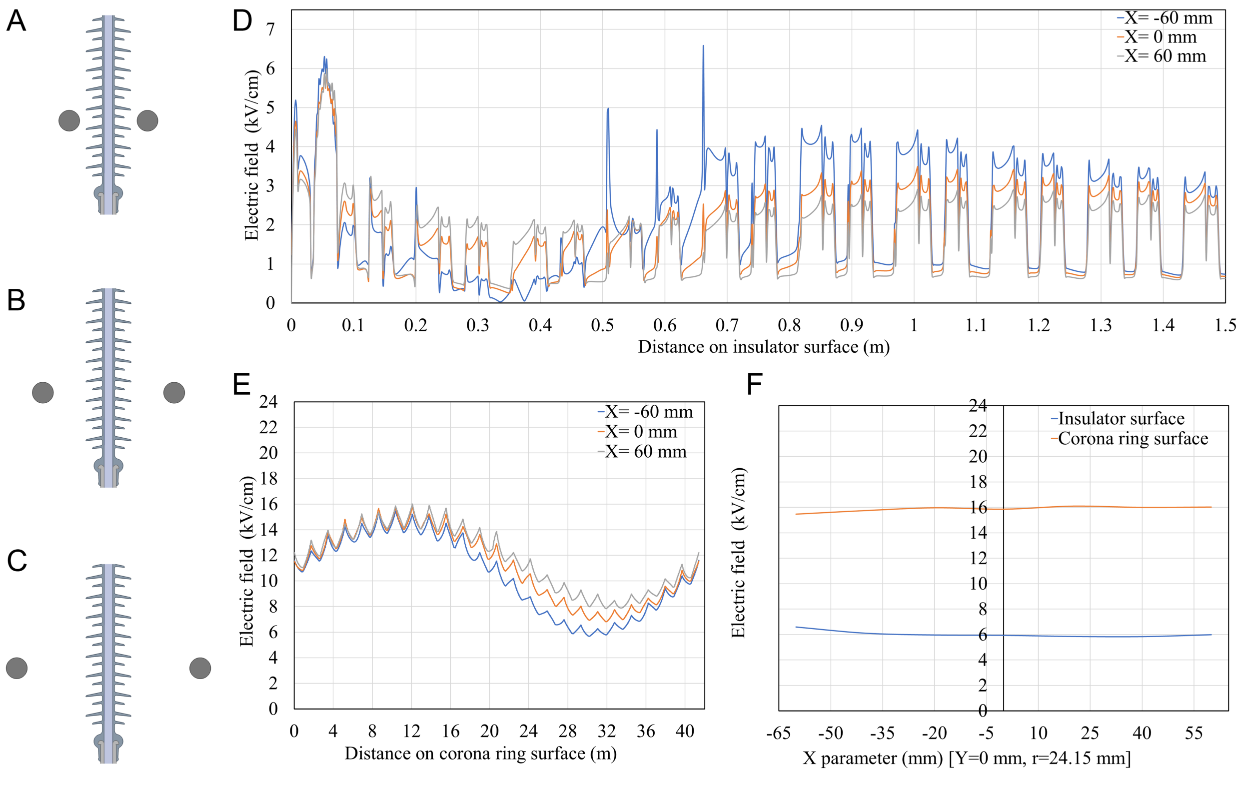

Fig. 6. Electric field distributions according to the change of corona ring radius.

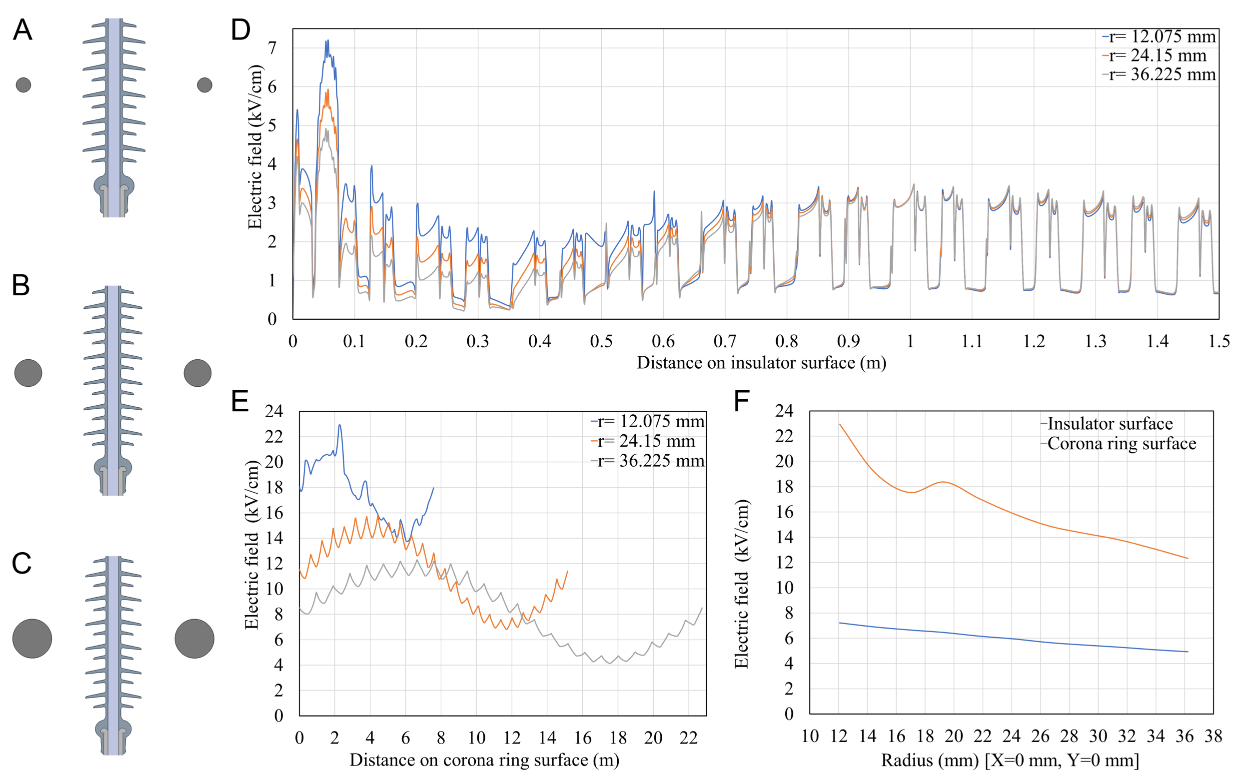

Fig. 7. Electric field distributions according to the change of corona ring metal radius.

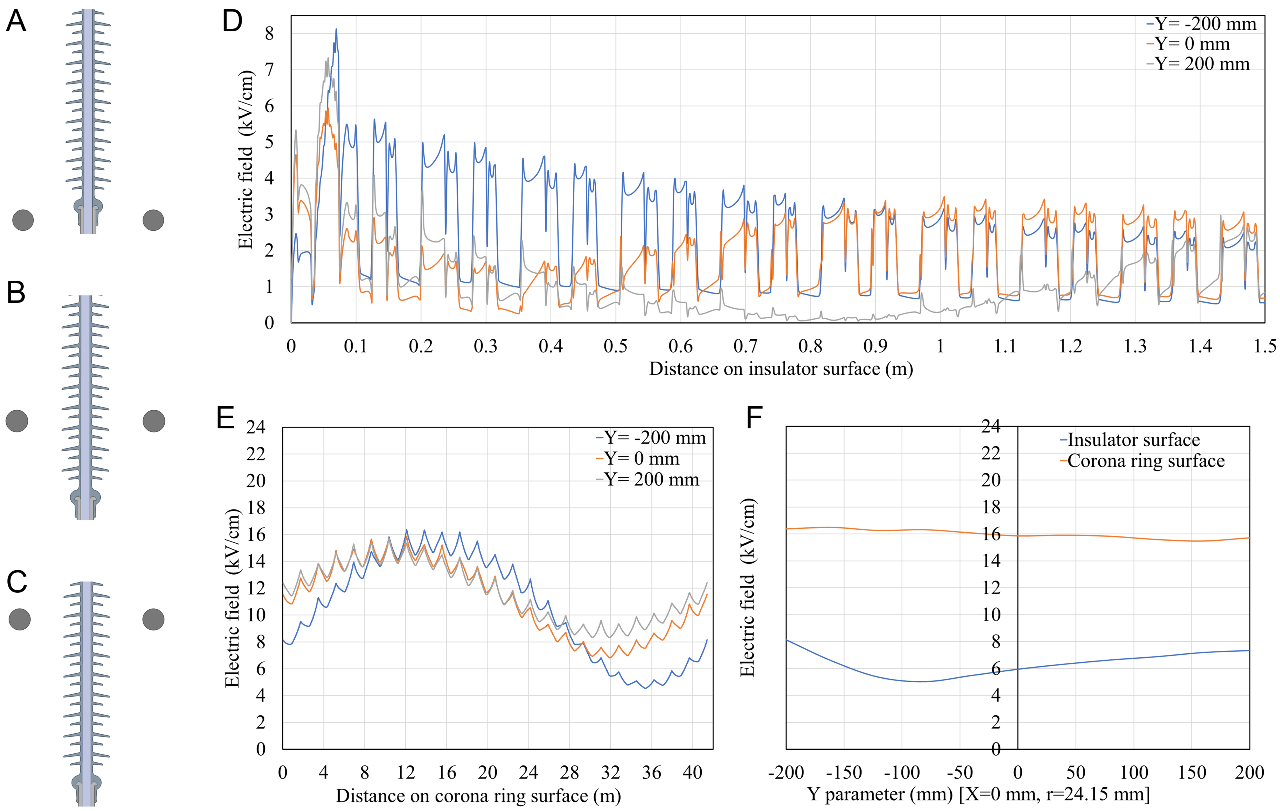

Fig. 8. Electric field distributions according to the change of corona ring height.

three-dimensional view of the isolation system examined with the analysis is shown in Fig. 1. Composite and insulator properties are shown in Table I.

The mesh structure created on the equipment is shown in Fig. 2. “128 Gb 1866 Mhz” memory, “NVIDIA Quadro K2000” graphics card, and two “Intel Xenon E5-2683 v3” processors were used in the workstation where the analyses were performed.

III. ANALYSIS STUDIES

Along with the analyses, the changes of three parameters in the corona ring were examined separately and together. In this context, the variation of the metal radius of the corona ring (24.15 mm in the reference model), the variation of the radius (150 mm in the reference model), and the change in the height (320 mm in the reference model) are examined. The effect of each of these parameters was analyzed separately, and then an analysis was carried out in which all parameters were evaluated together. The composite insulator and corona ring are shown in Figs. 3 and 4, respectively. Analyses were carried out in a two-dimensional working plane. The structure shown in Fig. 3 is a sectional view of the structure shown in Fig. 1c. The change in the geometric structure of the corona ring also affects the minimum arc distance. In this study, arc distances were not examined; only electric field distributions were examined. The minimum arc distances that occur depending on the corona ring design in the system design should also be taken into consideration in the system design.

TABLE II.
PARAMETER VALUES IN THE EXAMINED CASES

Case	*X* (mm)	*Y* (mm)	*r* (mm)
1	0	−120	24.15 < *r* < 36.225
2	0	−80	24.15 < *r*< 36.225
3	0	−40	24.15 < *r* < 36.225
4	0	0	24.15 < *r* < 36.225
5	20	−120	24.15 < *r* < 36.225
6	20	−80	24.15 < *r* < 36.225
7	20	−40	24.15 < *r* < 36.225
8	20	0	24.15 < *r* < 36.225
9	40	−120	24.15 < *r* < 36.225
10	40	−80	24.15 < *r* < 36.225
11	40	−40	24.15 < *r* < 36.225
12	40	0	24.15 < *r* < 36.225
13	60	−120	24.15 < *r* < 36.225
14	60	−80	24.15 < *r* < 36.225
15	60	−40	24.15 < *r* < 36.225
16	60	0	24.15 < *r* <36.225

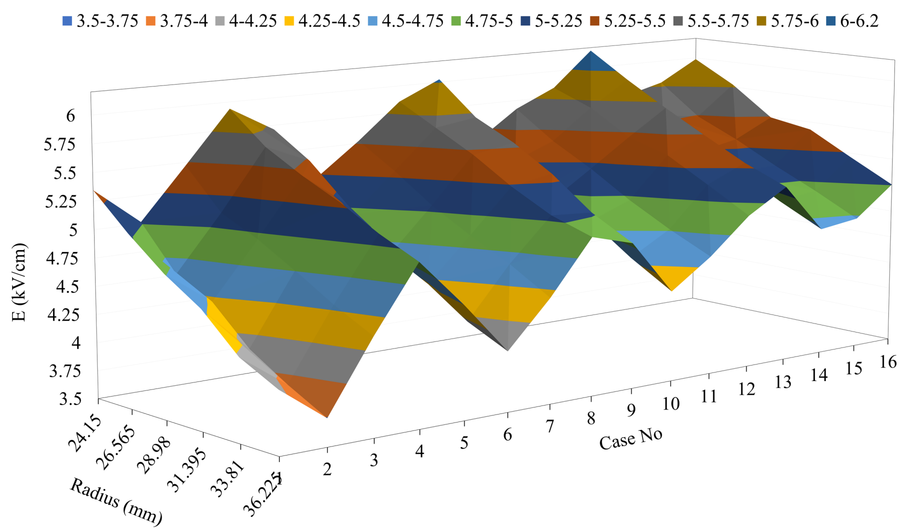

Fig. 9. Maximum electric field distributions on the composite insulator surface for 96 different states.

A. Investigation of Metal Radius Variation

The electric field distribution formed in the reference state is shown in Fig. 5. The metal radius variation of the corona ring is examined in this section. The parameter with a reference value of 24.15 mm has been changed between 12.075 mm and 36.225 mm. The electric field distribution profile formed on the composite insulator and corona ring surface is shown in Fig. 7d for reference values and extreme values. Maximum electric field values are shown in Fig. 7f. It is seen that the increase in the metal diameter of the corona ring has a positive effect on the composite insulator and the corona ring in terms of electric field distribution.

B. Examining Radius Variation

The parameter whose reference value is 150 mm has been shifted between +60 mm and –60 mm. The electric field distribution profile formed on the composite insulator and corona ring surface is shown in Fig. 6d for reference and extreme values. Maximum electric field values are shown in Fig. 6f. It is seen that the increase in the diameter of the corona ring makes the electric field distribution formed on the composite insulator surface more balanced. Although there is no significant change in the maximum electric field value when the diameter decreases, it is seen that the electric field distribution on the links after the corona ring line increases. It is seen that the change in diameter does not have a significant effect on the maximum electric field intensity on the corona ring surface.

C. Examining Altitude Change

The height variation of the corona ring is examined in this section. The parameter whose reference value is 320 mm has been shifted between +200 mm and –200 mm. The electric field distribution profile formed on the composite insulator and corona ring surface is shown in Fig. 8 for reference and extreme values. Maximum electric

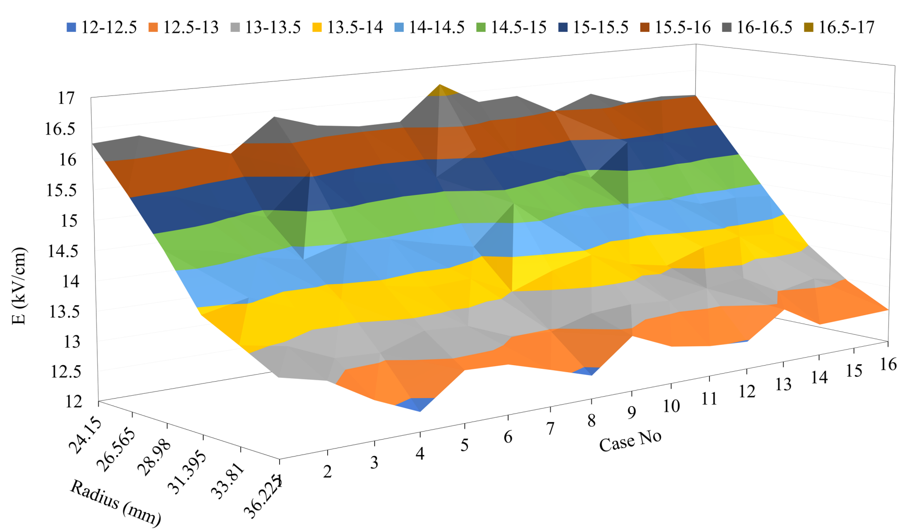

Fig. 10. Maximum electric field distributions on the corona ring surface for 96 different states.

field values are shown in Fig. 8f. The height change affects the maximum electric field strength and field profile. As can be seen in Fig. 8f, the variation on the composite insulator is not linear.

D. Evaluation of All Situations Together

A total of 96 designs were evaluated depending on three parameters to understand the effect of all situations simultaneously. Evaluated situations are shown in Table II. In these cases, the electric field distribution on the composite insulator is shown in Fig. 9, and the electric field distribution on the corona ring is shown in Fig. 10.

IV. DISCUSSION

As a result of the analyses carried out, it is seen that the corona ring design parameters affect the electric field distribution both on the insulator surface and on the corona ring. It is seen that the electric field distribution on both the composite insulator and the corona ring surface decreases when the corona ring metal diameter is increased. It is seen that the diameter of the corona ring does not have a significant effect on the maximum electric field strength. On the other hand, it is seen that the diameter changes the form of the electric field distribution. As the diameter increases, the electric field distribution becomes more balanced. The height of the corona ring affects the maximum electric field distribution and the form of the field distribution. The electric field distribution does not change linearly according to the height of the corona ring. This study investigated the effect of the design parameters of the corona ring on the electric field distribution. The results show the necessity of performing and interpreting electric field analyses with the finite element method while designing the isolation system.

Peer-review: Externally peer-reviewed.

Declaration of Interests: The authors declare that they have no competing interest.

Funding: This study received no funding.

REFERENCES

1. L. Lan, and R. S. Gorur, “Computation of ac wet flashover voltage of ceramic and composite insulators,” *IEEE Trans. Dielect. Electr. Insul.*, vol. 15, no. 5, pp. 1346–1352, 2008. [CrossRef]
2. B. Alboyacı, M. A. Çınar, Y. B. Demirol, and A. Ince, “Evaluation of the effect of structural defects in the heat-shrink cable terminal on electric field distribution,” *Eng. Fail. Anal.*, vol. 132, no. 105920, pp. 1–15, 2022. [CrossRef]
3. CIGRE Technical Brochure 284 - Use of corona rings to control the electrical field along transmission line composite insulators, WG B2.03, 2005. https://e-cigre.org/publication/284-use-of-corona-rings-to-control-the-electrical-field-along-transmission-line-composite-insulators
4. A. J. Phillips *et al.*, “Electric fields on AC composite transmission line insulators,” *IEEE Trans. Power Deliv.*, vol. 23, no. 2, pp. 823–830, 2008. [CrossRef]
5. I. Gutman, J. Lundquist, V. Dubickas, L. Carlshem, and R. Kleveborn. Design of Corona / Arcing Rings When Replacing Cap-and- Pin Insulators By Composite Insulators, XVII International Symposium on High Voltage Engineering, Hannover, Germany, August 22-26 2011. http://vlabs.iitkgp.ac.in/vhvlab/html/pages/CD/topics_a-h/A-007-GUT-F.pdf
6. A. J. Phillips, A. J. Maxwell, C. S. Engelbrecht, and I. Gutman, “Electric-field limits for the design of grading rings for composite line insulators,” *IEEE Trans. Power Deliv.*, vol. 30, no. 3, pp. 1110–1118, 2015. [CrossRef]
7. IEEE. *IEEE Guide for Application of Composite Insulators*, 2001. [CrossRef]
8. S. Ilhan, and A. Ozdemir, “380 kV corona ring optimization for AC voltages”, *IEEE Trans. Dielect. Electr. Insul.*, vol. 18, no. 2, pp. 408–417, 2011. [CrossRef]
9. J. Li, Z. Peng, Y. Feng, X. Fu, and T. Xie, “Electric field calculation and grading ring optimization of composite insulator for 500kV AC transmission lines,” in Proceedings of the 2010 IEEE International Conference on Solid Dielectrics. ICSD, vol. 2010, 2010, pp. 1–4. [CrossRef]
10. M. S. Kalimurugan, and R. V. Maheswari, “Investigation of electric field distribution on A C composite insulator using corona ring,” in ICIIECS 2015 - 2015 IEEE International Conference on Innovations in Information, Embedded and Communication Systems, 2015, pp. 1–6. [CrossRef]
11. B. M’Hamdi, M. Teguar, and A. Mekhaldi, “Optimal design of corona ring on HV composite insulator using PSO approach with dynamic population size,” *IEEE Trans. Dielect. Electr. Insul.*, vol. 23, no. 2, pp. 1048–1057, 2016. [CrossRef]
12. S. Ilhan, A. Ozdemir, and H. Ismailoglu, “Impacts of corona rings on the insulation performance of composite polymer insulator strings,” *IEEE Trans. Dielectr Electr. Insul.*, vol. 22, no. 3, pp. 1605–1612, 2015. [CrossRef]
13. E. Akbari, M. Mirzaie, M. B. Asadpoor, and A. Rahimnejad, “Effects of disc insulator type and corona ring on electric field and voltage distribution over 230-kV insulator string by numerical method,” *Iran. J. Electr. Electron. Eng.*, vol. 9, no. 1, pp. 58–66, 2013.
14. B. Alboyacı, M. A. Çınar, Y. B. Demirol, and M. Uzar, “Reducing the failures with adding glass insulators to composite insulators of 400 kV transmission line at high altitude,” *Eng. Fail. Anal.*, vol. 141, p. 106678, 2022. [CrossRef]

cigre Turkey

TEPES
TURKISH JOURNAL OF
ELECTRICAL POWER
AND ENERGY SYSTEMS

TEPES, Vol. 3, Issue. 1, 28-38, 2023 **DOI:** 10.5152/tepes.2023.22032

RESEARCH ARTICLE

Design of Four-Switch Buck-Boost Converter for Light Electric Vehicles: A Cost and Efficiency Perspective

Orkun Akın[1], Çağatay Bilgin[1], Samed Celik[2], Mehmet Onur Gülbahçe[1,3]

[1]Department of Electrical Engineering, Istanbul Technical University, Istanbul, Turkey
[2]Department of Electrical Engineering, Politecnico di Milano, Milan, Italy
[3]ITU Advanced Vehicle Technologies Application and Research Center, ILATAM, Istanbul, Turkey

Cite this article as: O. Akın, Ç. Bilgin, S. Çelik and M. O. Gülbahçe, "Design of four-switch buck-boost converter for light electric vehicles: a cost and efficiency perspective," *Turk J Electr Power Energy Syst.*, 2023; 3(1), 28-38.

ABSTRACT

Light electric vehicles (LEV) necessitate power electronic converters that have a high-power density and a high efficiency in order to accommodate the limited space available. The input voltage of a four-switch buck-boost converter can be increased or decreased across a wide range, allowing for energy to be transferred in either direction. This type of converter topology is particularly efficient. In this study, an algorithm is presented that proposes two different designs for a four-switch buck-boost converter within both efficiency and cost constraints. Two 96-12-5 V, 500 W converter that is powered by a 48 V battery have been developed for the purpose of determining whether or not the proposed algorithm is effective. The proposed algorithm chose the switches, inductance, and capacitance based on a previously created database.

Index terms— Four-switch buck-boost converter, efficient power electronics converters, light electric vehicles

I. INTRODUCTION

Light electric vehicles (LEV) encompass all types of low-speed electric vehicles, such as electric scooters, electric bicycles, forklifts, and electric motorcyclists and represent a substantial portion of the market for electric vehicles. Contrary to conventional internal combustion engine-powered vehicles, this type of vehicle is powered by batteries with bus voltages ranging from 28 V to 168 V [1]. LEVs share common features such as motor drives, battery management systems, battery chargers, and smart features and electronics which are gaining popularity because of increasing battery sizes. Since there is only one battery and one direct current (DC) bus in the car, DC-DC converters are required to get the various voltage levels required by the vehicle [2]. Integrated and efficient converters are necessary for LEVs due to their limited internal volume and rising power requirements. However, the efficiency and power density requirements for power electronics converters are contradicting [3]. Researchers are becoming increasingly interested in finding the optimal balance between the two.

Four-switch buck-boost converters are high-efficiency converter topologies that may increase or decrease the input voltage across a broad range and provide bidirectional energy transfer [4]. There are two fundamental operational states: buck and boost. Four-switch buck-boost converters can regulate output voltage without reversing the direction of the input voltage. Due to the ongoing operation of one of the switching components on the high side, these converter's conduction losses are its greatest weakness. Optimizing these losses is possible by selecting various semiconductor devices. The preference for this converter in LEV applications is due to the high variable voltage requirements [5]. In addition, the research [6, 7] indicates that the four-switch buck-boost topology is strongly recommended in solar converters and micro-grid applications.

In addition to studies on the design of the four-switch buck-boost converter, there are numerous studies on its control in the literature. In these studies, various control approaches, including the quadrilateral control method [8] and model predictive control, were investigated. None of the articles published on design and control has the four-switch buck-boost converter designed using a design method that takes into consideration the losses of all components and allows the selection of components from a database.

Corresponding author: Orkun Akın, **E-mail:** akinor17@itu.edu.tr

Received: December 29, 2022
Accepted: January 10, 2023
Publication Date: January 25, 2023

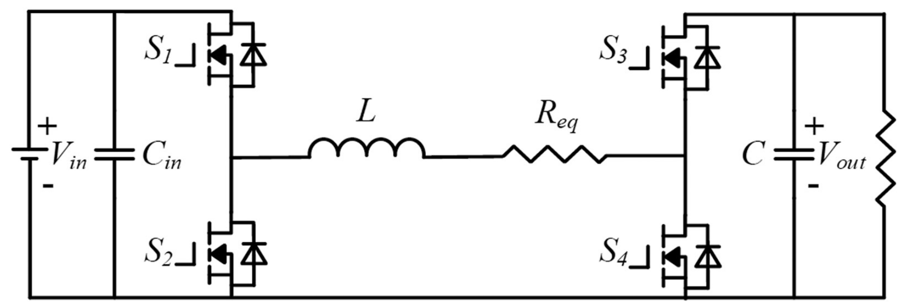

Fig. 1. Four-switch buck-boost circuit topology [9].

In contrast to previous research, the four-switch buck-boost converter for the LEV is designed in this work using an algorithm based on the selection of components from a particular database, taking into consideration losses in all components or the prices. The design algorithm minimizes the losses of the converter, its cost, and any other determinable constraints. Four-switch buck-boost converter topology is shown in Fig. 1.

In this study, by using the proposed algorithm, two different converter designs for LEVs have been designed that can operate at 500 W output power, 48 V input voltage, and 96 V-12 V-5 V output voltages. The proposed algorithm chooses the components based on the chosen constraints such as high efficiency or low-cost prioritization. The components are chosen from previously created databases. In the second section of the study, the topological analyses and the mathematical fundamentals of four-switch buck-boost converter design are presented. In the third section, mathematical models of the losses incurred by the two designed converters are created. Lastly, in the fourth section, to test the proposed algorithm, a case study is conducted and the results regarding the study are given in tables and radar graphs. The most valuable contribution of this paper is the proposed algorithm, the effectiveness of which is confirmed by the case study.

Main Points

- An algorithm that can choose components for the design based on chosen constraints such as efficiency and price is proposed.
- Mathematical models of the losses caused by the components and databases of the components are created.
- Two 500 W 48 V/96-12-5 V four-switch buck-boost converters are designed using the proposed algorithm.

II. DESIGN OF A FOUR-SWITCH BUCK-BOOST CONVERTER

A four-switch buck-boost circuit is a non-inverting topology that may increase and decrease voltage. In contrast to the typical buck-boost circuit, this circuit utilizes semiconductor switches instead of diodes. Due to this difference, the diodes do not incur voltage drops in this circuit. In this manner, system efficiency is increased and the circuit functions synchronously [9].

This converter operates in two fundamental states. The circuit operates in boost mode if the input voltage is less than the desired output voltage, and in buck mode, if the input voltage is more than the desired output voltage. Due to non-ideal functioning states of semiconductor elements and other components, dead zones may exist when operating in various operational modes. This dead zone typically arises when the input voltage and output voltage are close. This

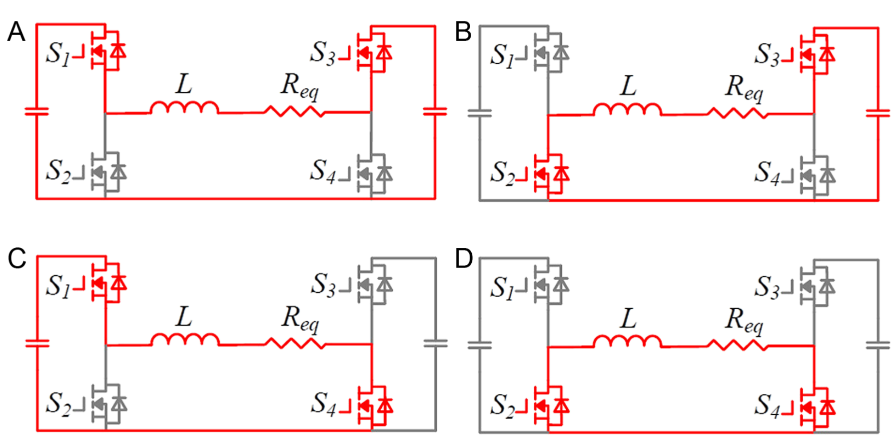

Fig. 2. (a) First operating condition, (b) second operating condition, (c) third operating condition, (d) fourth operating condition [9].

dead zone can result in numerous state transitions, an increase in output ripple voltage, and system instability [10].

A. Operating States of Four-Switch Buck-Boost Converter

Operating states of four-switch buck boost converter is given in Fig. 2. In the first operational condition, S1 and S3 are switched on, and the source is directly connected to the load. In the second state, switches S2 and S3 are on the source and load are no longer connected. The load is supplied with energy via the inductance. When the converter transitions from state 1 to state 2, it operates in the buck mode. In the third state of operation, switches S1 and S4 are active. In this scenario, the inductance is charged by the source. When the converter transitions from state 1 to state 3, it will operate in boost mode. When the converter transitions from state 2 to state 3, it operates in the buck-boost mode. In the fourth operational state, the S2 and S4 switches are conducting; in this scenario, soft switching can be used to improve system efficiency [9].

B. Parameter Calculations of the Four-Switch Buck-Boost Converter

Minimum and maximum input voltages, output voltage, output current, switching frequency, gate voltage of the switch, junction temperature, and ambient temperature are necessary design parameters. Using the proposed design algorithm, the relevant computations are performed after determining these values.

The proposed algorithm identifies the operating states of the converter before calculating the duty cycle for the identified operating states. Then, the necessary inductance and capacitance values for the relevant operating circumstances are determined. The maximum switch current, inductance current, root mean square (RMS) values of switch currents, and capacitance current are computed. Using these quantities, the proper core for the inductance is picked, and then, the conduction and core losses of the inductance are computed. Then, the selection of the capacitor with the lowest resistance or the lowest price is made using the compiled database, and the capacitor loss is computed. The switching and conduction losses of the switches that match the converter's rated values are calculated. From the several switches whose losses are calculated, the switch with the lowest losses or lowest price is chosen. In the final step of the thermal design process, the thermal resistance of the heat sink is calculated using the ambient and joint temperatures acquired as inputs previously, and the dimensions of the heat sink can be selected based on these calculations. Proposed algorithm's flow chart is shown in Fig. 3.

1) Determining the Duty Cycle

Since the four-switch buck-boost converter can operate in both buck and boost modes, different duty cycles (D_{buck} and D_{boost}) are determined for each case according to (1) and (2). Here, V_{OUT} represents the output voltage, V_{INmax} represents the maximum input voltage, V_{INmin} represents the minimum input voltage, and η represents the estimated efficiency.

$$D_{buck} = \frac{V_{OUT}}{V_{INmax} \cdot \eta} \tag{1}$$

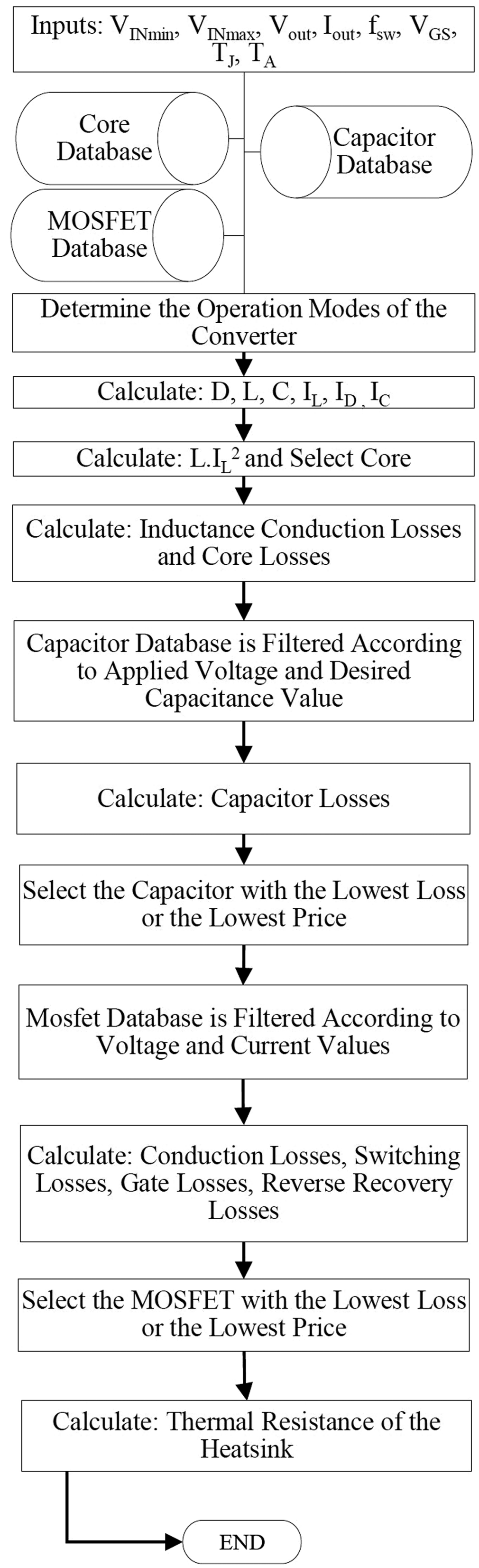

Fig. 3. Flow chart of the design algorithm.

$$D_{boost} = 1 - \frac{V_{INmin} \cdot \eta}{V_{OUT}} \quad (2)$$

2) Determining the Required Inductance

The selection of inductance is determined by the inductance current ripple. Therefore, the inductance value is computed separately for the buck and boost operating modes, and the biggest inductance value is chosen to accomplish the desired inductance current ripple in both states. The needed inductance values for the design can be calculated utilizing (3) and (4). In (3) and (4), f_{sw} represents the switching frequency (Hz), whereas K_{ind} is the ratio between the inductance current ripple and the maximum output current.

$$L_{buck} \geq \frac{V_{OUT} \cdot (V_{INmax} - V_{OUT})}{K_{ind} \cdot f_{sw} \cdot V_{INmax} \cdot I_{OUT}} \quad (3)$$

$$L_{boost} \geq \frac{V_{INmin}^2 \cdot (V_{OUT} - V_{INmin})}{K_{ind} \cdot f_{sw} \cdot V_{OUT}^2 \cdot I_{OUT}} \quad (4)$$

3) Determining the Peak Switch Current

In order to choose the switches, it is necessary to know the maximum current and voltage going through them. In the buck mode, the highest switch current occurs when the input voltage is at its maximum, whereas, in the boost mode, the highest value occurs when the input voltage is at its minimum. In whichever of these two scenarios has the higher current value, the switches are selected based on this value. Using (5), (6), (7), and (8), the highest switching currents for both operating states can be computed. In (5), (6), (7), and (8), ΔI_{max} represents the maximum ripple current and I_{SWmax} represents the maximum switch current.

For the buck mode:

$$\Delta I_{max} = \frac{(V_{INmin} - V_{OUT}) \cdot D_{buck}}{f_{sw} \cdot L} \quad (5)$$

$$I_{SWmax} = \frac{\Delta I_{max}}{2} + I_{OUT} \quad (6)$$

For the boost mode:

$$\Delta I_{max} = \frac{V_{INmin} \cdot D_{boost}}{f_{sw} \cdot L} \quad (7)$$

$$I_{SWmax} = \frac{\Delta I_{max}}{2} + \frac{I_{OUT}}{1 - D_{boost}} \quad (8)$$

4) Determining the Output Capacitance

The selection of capacitors is based on the output voltage ripple determined by the designer. In buck and boost operational states,

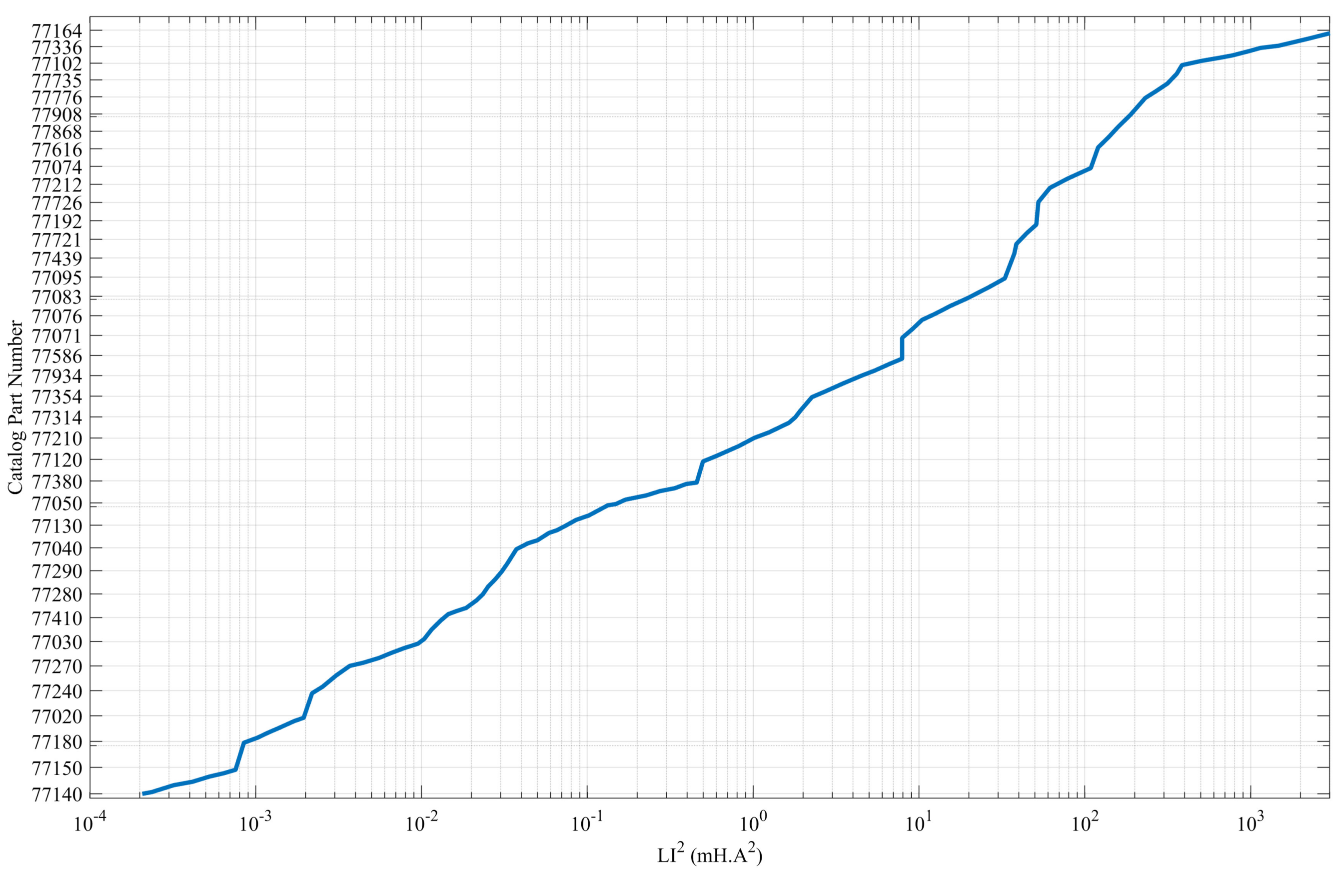

Fig. 4. $L.I^2$ values of toroid cores owned by the magnetics [11]

voltage ripple values vary. Therefore, the capacitance value is chosen with the worst-case possible scenario in mind. The minimal amount of capacitance (C_{buck} and C_{boost}) required for both operational conditions can be determined using (9) and (10). $V_{OUTripple}$ represents the output voltage ripple in the equations.

$$C_{buck} = \frac{K_{ind}.I_{OUT}}{8.f_{sw}.V_{OUTripple}} \tag{9}$$

$$C_{boost} = \frac{I_{OUT}.D_{boost}}{f_{sw}.V_{OUTripple}} \tag{10}$$

III. LOSS MODELS OF FOUR-SWITCH BUCK-BOOST CONVERTER COMPONENTS

In this section of the study, loss models for the proposed converter are presented. In addition to describing the influence of inductance and capacitance resistance on losses, the inductance will also be designed. Then, the losses on the switching device were modeled mathematically, and the required heat sink volume is calculated for the thermal design.

A. Inductance Design and Loss Model

When designing an inductance, it is required to select the core, calculate the number of turns, and select the type of winding. Then, it is necessary to compute core and conduction losses.

After selecting the most suitable core type for the operating frequency, the LI^2 value is calculated and the core model is selected from the manufacturer's graph in Fig. 4 [11]. Then, the number of turns N is determined using the highest inductance factor (A_L) of the core, as shown in (11).

$$N = 10^3 \times \sqrt{\frac{L(mH)}{A_L\left(\frac{nH}{T^2}\right)}} \tag{11}$$

This calculated number of turns is valid in the no-load case. The magnetic field strength H is computed as A.T/cm with (12), where L_e is the average length of force lines.

$$H = \frac{N \times I}{L_e} \tag{12}$$

Using this result, the initial permeability value is determined as a percentage from the manufacturer-supplied graph in Fig. 5. This value is used to calculate the final number of turns by dividing the number of turns at no load by it. Prior to calculating the core losses, the maximum H_{max} and minimum H_{min} magnetic field strengths are determined by (13) and (14).

$$H_{max} = 4\pi \times \left[\frac{N}{L_e} \times \left(I_{DC} + \frac{\Delta I}{2}\right)\right] \tag{13}$$

$$H_{min} = 4\pi \times \left[\frac{N}{L_e} \times \left(I_{DC} - \frac{\Delta I}{2}\right)\right] \tag{14}$$

The variation of flux densities (ΔB) corresponding to these field strengths is obtained from the graph provided by the manufacturer in Fig. 6. The flux density ripple is calculated using B_{pk} (15).

$$B_{pk} = \frac{\Delta B}{2} \tag{15}$$

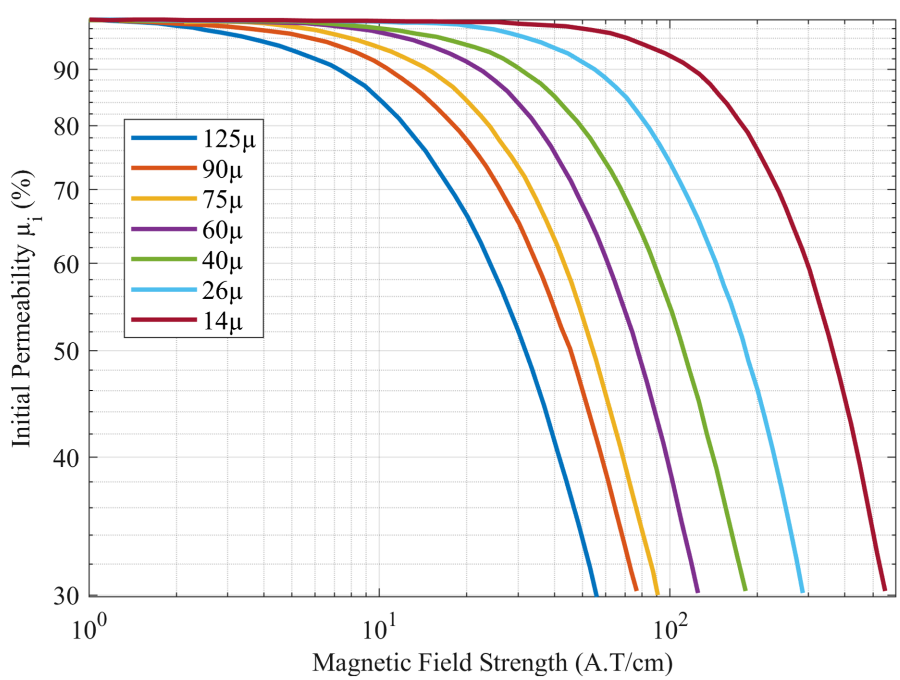

Fig. 5. Initial permeability selection graph [11].

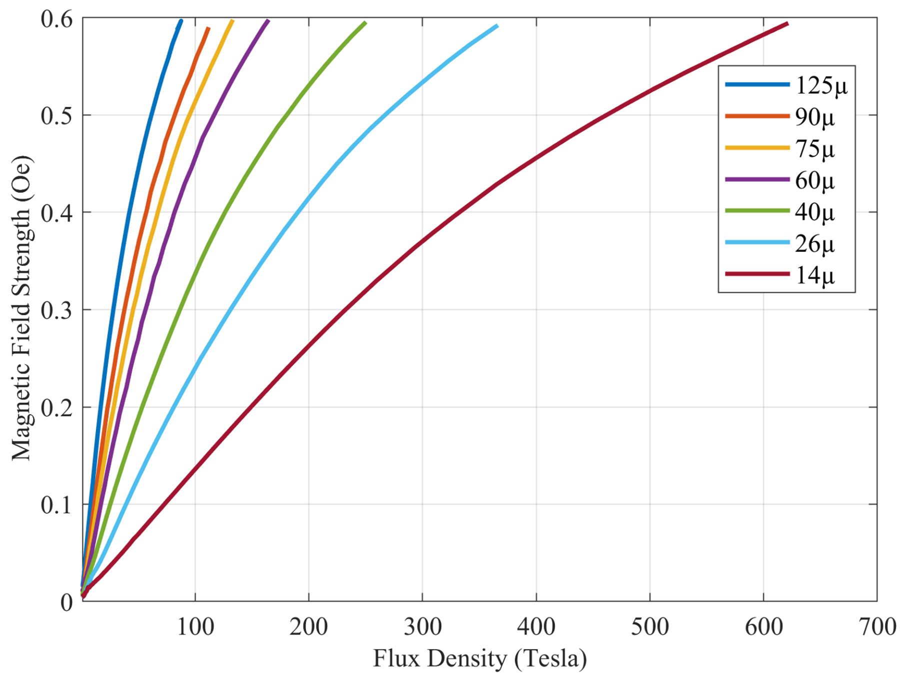

Fig. 6. Variation of flux density with magnetic field strength [11].

Then, the core loss density (PL) is obtained using (16). The coefficients a, b, and c can also be derived from the information on the datasheets.

$$PL = a \times B_{pk}^{b} \times f_{sw}^{c} \tag{16}$$

After determining the loss density, (17) determines the core losses P_{fe}. Here, A_e is the cross-sectional area of the core.

$$P_{fe} = PL \times L_e \times A_e \tag{17}$$

In the preceding computations, the smallest inductance value (L) necessary for the application is calculated. For the boost operating condition, the maximum current (I_{Lmax}) and the minimum current (I_{Lmin}) passing over the inductance are computed using (18), (19), and (20). ΔI_L is the value of the ripple in the inductance current.

$$\Delta I_L = \frac{V_{INmin}.D_{boost}}{f_{sw}.L} \tag{18}$$

$$I_{Lmax} = \frac{\Delta I_L}{2} + \frac{I_{OUT}}{1 - D_{boost}} \tag{19}$$

$$I_{Lmin} = -\frac{\Delta I_L}{2} + \frac{I_{OUT}}{1 - D_{boost}} \tag{20}$$

For the buck operating condition, the maximum current and the minimum current values are calculated with (21)–(23).

$$\Delta I_L = \frac{\left(V_{INmin} - V_{OUT}\right).D_{buck}}{f_{sw}.L} \tag{21}$$

$$I_{Lmax} = \frac{\Delta I_L}{2} + I_{out} \tag{22}$$

$$I_{Lmin} = -\frac{\Delta I_L}{2} + I_{out} \tag{23}$$

For the selection of the core, the maximum inductance current is used. This current value varies based on the operational state. Calculations are performed based on the operating condition with the greatest losses. The $L.I^2$ value is determined using the maximum inductance current. Using the determined $L.I^2$ value, the core type is chosen from the curve of magnetics firm, and the H value is computed using (11) and (12). With the given H value, the initial permeability value is determined from the graph in Fig. 5. In this study, the database contained just toroidal core data. By adding additional core types and materials to the database, it is possible to create designs with greater flexibility. The number of turns can be computed using the initial permeability value obtained from Fig. 5. The preceding stages are then repeated. The flux density, flux density ripple, core loss density, and core losses are calculated. After computing the core losses, using the entire length of the conductor and the DC current resistance of this conductor, the conduction losses are calculated. Adding the core and conduction losses yields the overall inductance losses denoted by $P_{totalinductance}$.

B. Loss Model of the Capacitor

The capacitor with the lowest resistance value or the lowest price is chosen from the capacitors contained in the database considering the capacitance and output voltage values calculated by the previous calculations. Loss values for the chosen capacitor value are calculated using (24)–(26). In (24), (25), and (26), ESR stands for equivalent series resistance, $P_{totalinductance}$ stands for total inductance losses and it is calculated in the previous section.

$$I_{Cout(rms)} = I_{out} \times \sqrt{\frac{V_{OUT}}{V_{INmin}} - 1} \tag{24}$$

$$P_{Cout} = I^2_{Cout(rms)} \times ESR \tag{25}$$

$$P_{total} = P_{totalinductance} + P_{Cout} \tag{26}$$

C. Loss Model of the Switch

In power electronic circuits, the losses of semiconductor switches are separated into conduction and switching losses. For the circuit to be within the specified efficiency range and for optimal thermal design, these losses must be precisely predicted.

1) Conduction Losses

The conduction losses of a semiconductor switch are calculated using the on resistance R_{Dson} and the current I_D flowing through it. This information is accessible through the components datasheet. Since metal-oxide semiconductor field-effect transistor (MOSFET) is used in this study as the switching device, the instantaneous conduction losses vary as shown in (27) [12].

$$P_{condM}(t) = u_{DS}(t).i_D(t) = R_{DSon}.i_D^2(t) \tag{27}$$

The instantaneous loss power expression is integrated over the switching period T_{sw} to obtain the average conduction loss [12].

$$P_{condM} = \frac{1}{T_{sw}} \int_0^{T_{sw}} (R_{DSon}.i_D^2(t))dt = R_{DSon}.I^2_{Drms} \tag{28}$$

2) Switching Losses

When the gate voltage of a switch exceeds a specific threshold value, the switch turns on, and depending on parasitic capacitances, the current rises to the conduction current. Meanwhile, the MOSFET voltage drops to the transmission voltage. When the switch is cut, the opposite of the same events occurs, and switching losses occur [12].

The datasheet provides the current rising time t_{ri}, the fall time t_{fi}, the gate resistance R_G, the parasitic capacitance C_{GD} between the gate and drain, and the reverse recovery charge Qrr. C_{GD} has been obtained from the data sheet as C_{GD1} and C_{GD2} for the voltages when the switch is on and off. Using the voltage on the switch U_{DD} and the gate voltage U_{Dr}, the rise time and fall time of the voltage are then calculated by (29)–(34). t_{fu} represents the voltage fall time and t_{ru} represents the voltage rising time in the equations. The V_{GS1} and V_{GS2} gate-source voltages are determined from the datasheet for the selected I_{D1} and I_{D2} currents. Then, the gate threshold voltage is obtained using the formula V_{TH} (35). Since gate plateau voltage $U_{plateau}$ is not provided in a large number of datasheets, it is derived from gate voltage-current curves using I_D drain current with (36).

$$tfu1 = (U_{DD} - R_{DSon}.I_{Don}).R_G.\frac{C_{GD1}}{U_{Dr} - U_{plateau}} \tag{29}$$

$$tfu2 = (U_{DD} - R_{DSon}.I_{Don}).R_G.\frac{C_{GD2}}{U_{Dr} - U_{plateau}} \tag{30}$$

$$tfu = \frac{tfu1 + tfu2}{2} \tag{31}$$

$$tru1 = (U_{DD} - R_{DSon}.I_{Don}).R_G.\frac{C_{GD1}}{U_{plateau}} \tag{32}$$

$$tru2 = (U_{DD} - R_{DSon}.I_{Don}).R_G.\frac{C_{GD2}}{U_{plateau}} \tag{33}$$

$$tru = \frac{tru1 + tru2}{2} \tag{34}$$

$$V_{TH} = \frac{V_{GS1}.\sqrt{I_{D2}} - V_{GS2}.\sqrt{I_{D1}}}{\sqrt{I_{D2}} - \sqrt{I_{D1}}} \tag{35}$$

$$U_{plateau} = V_{TH} + \sqrt{\frac{I_D}{\frac{I_{D1}}{(V_{GS1} - V_{TH})^2}}} \tag{36}$$

After doing the necessary calculations with these equations, the energy consumed during the turn-on (E_{onM}), and turn-off (E_{offM}) and the power losses are computed using (37)–(39), respectively.

$$E_{onM} = \int_0^{tri+tfu} u_{DS}(t).i_D(t)dt = U_{DD}.I_{Don}.\frac{tri + tfu}{2} + Q_{rr}.U_{DD} \tag{37}$$

$$E_{offM} = \int_0^{tru+tfi} u_{DS}(t).i_D(t)dt = U_{DD}.I_{Don}.\frac{tru + tfi}{2} \tag{38}$$

$$P_{swM} = (E_{onM} + E_{offM}).f_{sw} \tag{39}$$

3) Reverse Recovery Losses

During switching, the body diodes of MOSFETs generate losses, with the majority of these losses being reverse recovery losses.

$$E_{Drr} = \int_0^{tri+tfu} U_D(t).i_F(t) = \frac{1}{4}.Q_{rr}.U_{DD} \tag{40}$$

$$P_{Drr} = \frac{1}{4}.Q_{rr}.U_{DD}.f_{sw} \tag{41}$$

4) Gate Losses

MOSFET gate losses are caused by the energy necessary to charge the parasitic capacitances at the MOSFET gate. In (42), Q_g represents gate charge on the gate terminal of the switch which is provided in the datasheet of the semiconductor switch, and V_{GS} shows the gate-source voltage to be used.

$$P_g = Q_g.V_{GS}.f_{sw} \tag{42}$$

D. Thermal Design

The losses on semiconductor switches cause them to produce heat. The rise in temperature caused by heating has a direct effect on the performance of semiconductors. The conduction resistance and the conduction losses increase as the temperature rises, as do the

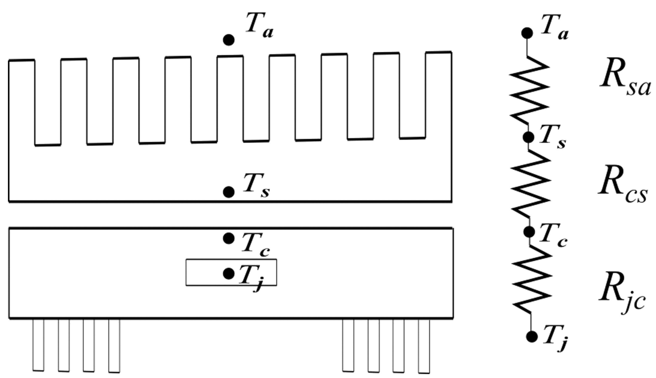

Fig. 7. Thermal equivalent circuit

switching losses and the maximum withstand current rating of the switch. Heat sinks are used to defend against all of these negatives. The simplest thermal circuit consists of the thermal resistances R_{SA} between the heat sink and the ambient, R_{CS} between the switch case and the heat sink, and R_{JC} between the junction and the switch case. Thermal equivalent circuit is shown in Fig. 7.

For junction temperature T_J and ambient temperature T_A, the one-dimensional heat transfer equation between temperature, losses, and thermal resistances is given by (43).

$$T_J = T_A + P_{loss}\left(R_{JC} + R_{CS} + R_{SA}\right) \tag{43}$$

While the R_{JC} value is provided in the datasheet of the semiconductor switch, the R_{CS} varies based on the thickness of the thermal material used, its area of usage, and its thermal conductivity.

$$R_{CS} = \frac{Width}{Area\,x\,Thermal\,Conductivity} \tag{44}$$

After calculating the desired junction and ambient temperatures, the R_{SA} value is calculated and the dimensions of the heat sink can be chosen based on this value.

IV. CASE STUDY

To examine the performance of the suggested design algorithm, two converters with the operational parameters listed in TABLE I were designed. In these designs, while considering the price and efficiency constraint, the volume constraint is not taken into account.

A. Price-Constrained Design

In the algorithm-generated design, choices have been made to minimize the power losses or the prices in the inductance, capacitance, and switch components. As shown in TABLES II-IV, the price-constrained design led to the selection of Kool Mμ Toroid number 77076 from Magnetics as the inductance core, 336CKS200MLU from Illinois Capacitor as the output capacitor, and RD3S100AAFRA from ROHM as the switch. In Figs. 8 and 9, the radar chart displays the lost power levels of price-constrained design. The most significant portion of the total loss is attributable to the total switch losses, while the output capacitor results in the minimum loss value. When examining the graph of switching losses, it is evident that conduction

TABLE I.
DESIGN PARAMETERS OF THE CONVERTER

Parameters	Symbols	Values
Input voltage	V_{IN}	48 V
Output voltages	V_{OUT1}	96-12-5 V
Switching frequency	f_{sw}	100 kHz
Output current	I_{OUT}	5.208 A
Output power	P_{OUT}	500 W
Applied gate voltage	V_{GS}	15 V
Output voltage ripple	$V_{OUTripple}$	0.96 V
Inductor ripple current relative to the maximum output current	K_{ind}	0.4
Junction temperature	T_J	125 °C
Ambient temperature	T_A	40 °C

TABLE II.
PARAMETERS OF THE BOTH CONVERTERS' INDUCTANCE

Calculated Inductance	Selected Core	Number of Turns	Conduction Losses	Core Losses	Total Inductance Losses
57.6 μ H	Magnetics 77076	46	1.8922 W	0.9386 W	2.8308 W

TABLE III.
PARAMETERS OF THE PRICE-CONSTRAINED CONVERTER'S CAPACITOR

Calculated Capacitance Value	Selected Capacitor	Capacitor Losses	Price
27.12 μ F	336CKS200MLU 200 V, 33 μ F	0.262 W	$0.222

TABLE IV.
PARAMETERS OF THE PRICE-CONSTRAINED CONVERTER'S SWITCHING COMPONENTS

Selected MOSFET	Conduction Losses	Switching Losses	Reverse Recovery Losses	Gate Losses	Total MOSFET Losses	Calculated Thermal Resistance of the Heat Sink	Price
RD3S100AAFRA 190 V, 10 A	29.1663 W	19.885 W	0.015 W	0.1560 W	49.22 W	3.448 °C/W	$1.28 × 4

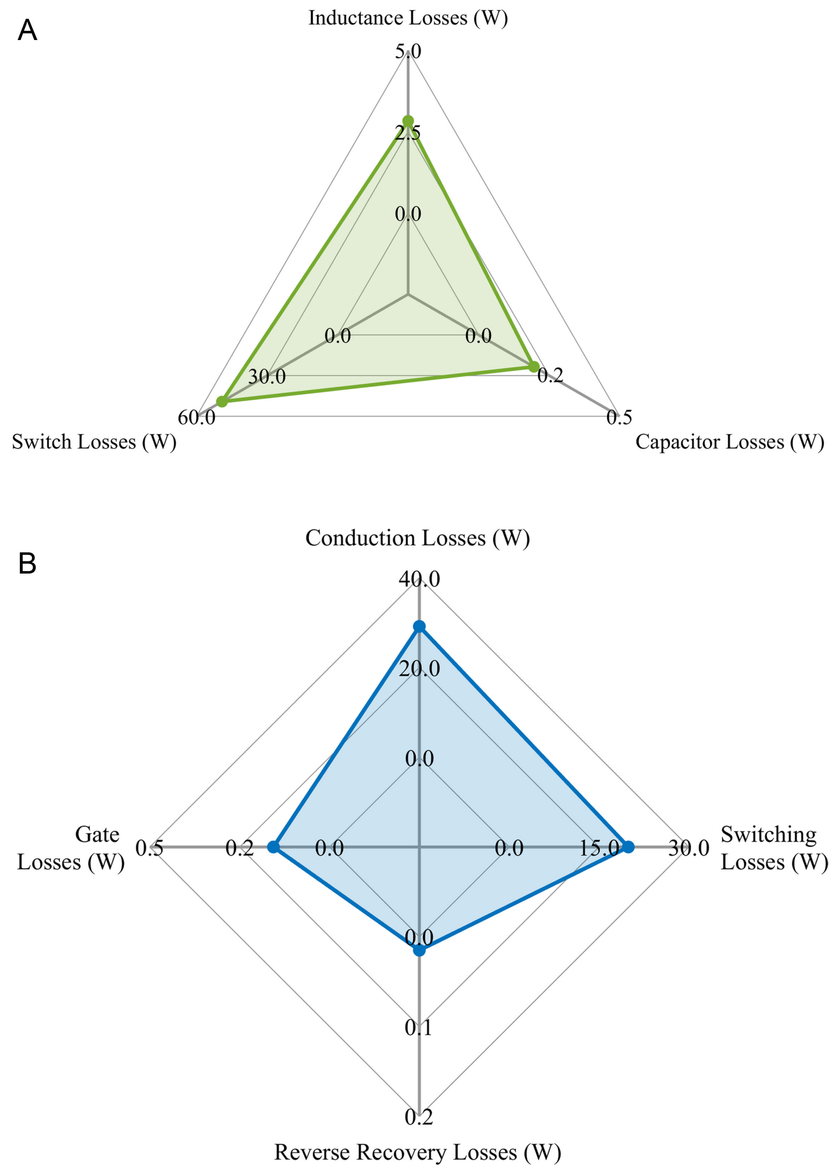

Fig. 8. (a) Total losses of the price-constrained design. (b) Semiconductor losses of the price-constrained design

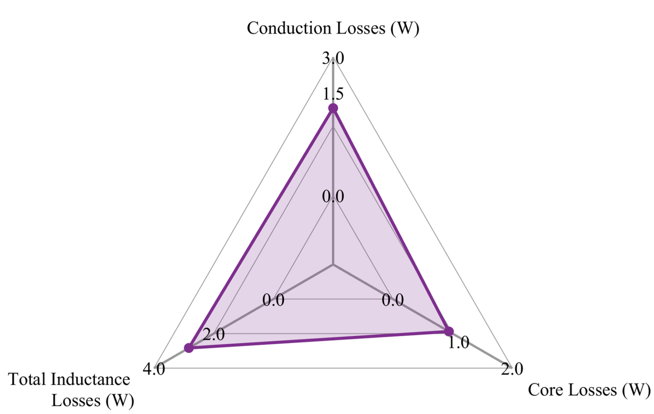

Fig. 9. Inductance losses of the both designs

losses is the greatest, followed by switching losses, and reverse recovery losses is the least.

Examining the inductance losses reveals that the conduction losses are the greatest loss. In the price-constrained design, the total loss is 52.25 W, the total price is $5.34 (inductance not included), and the efficiency is calculated to be 89.55%.

TABLE V.
PARAMETERS OF THE EFFICIENCY-CONSTRAINED CONVERTER'S CAPACITOR

Calculated Capacitance Value	Selected Capacitor	Capacitor Losses	Price
27.12 μ F	107CKS160M 160V, 100 μ F	0.086 W	$0.52

TABLE VI.
PARAMETERS OF THE EFFICIENCY-CONSTRAINED CONVERTER'S SWITCHING COMPONENTS

Selected MOSFET	Conduction Losses	Switching Losses	Reverse Recovery Losses	Gate Losses	Total MOSFET Losses	Calculated Thermal Resistance of the Heat Sink	Price
TSM650N15CS 150 V, 9 A	10.1316 W	6.8602 W	0.4656 W	0.0720 W	17.5294 W	3.65 °C/W	\$5.01 × 4

B. Efficiency-Constrained Design

Same inductance core is also used in efficiency-constrained design since the price information for the core is not available. As shown in TABLES II, V and VI, the efficiency-constrained design led to the selection of Kool Mµ Toroid number 77076 from Magnetics as the inductance core, 107CKS160M from Illinois Capacitor as the output capacitor, and TSM650N15CS from Taiwan Semiconductor as the switch. For the efficiency-constrained design, it is clear from the radar graphs in Figs. 9 and 10 that the most significant portion of the total losses is caused by the total switch losses, while the output

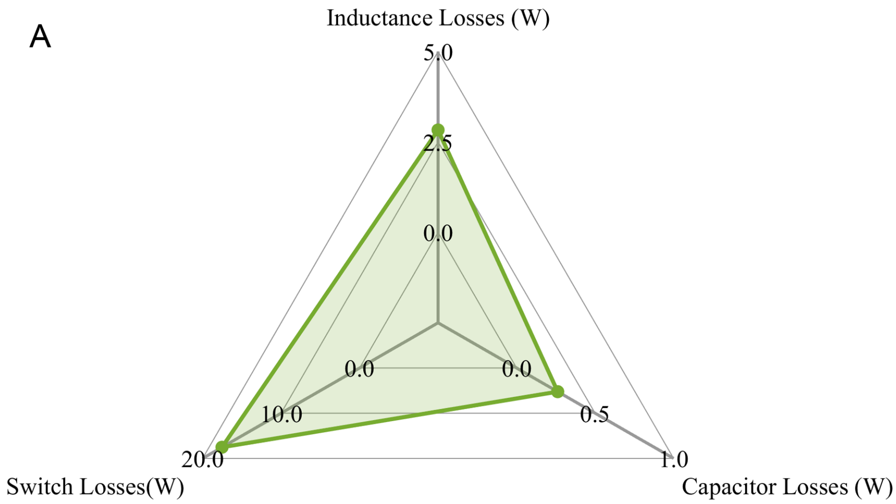

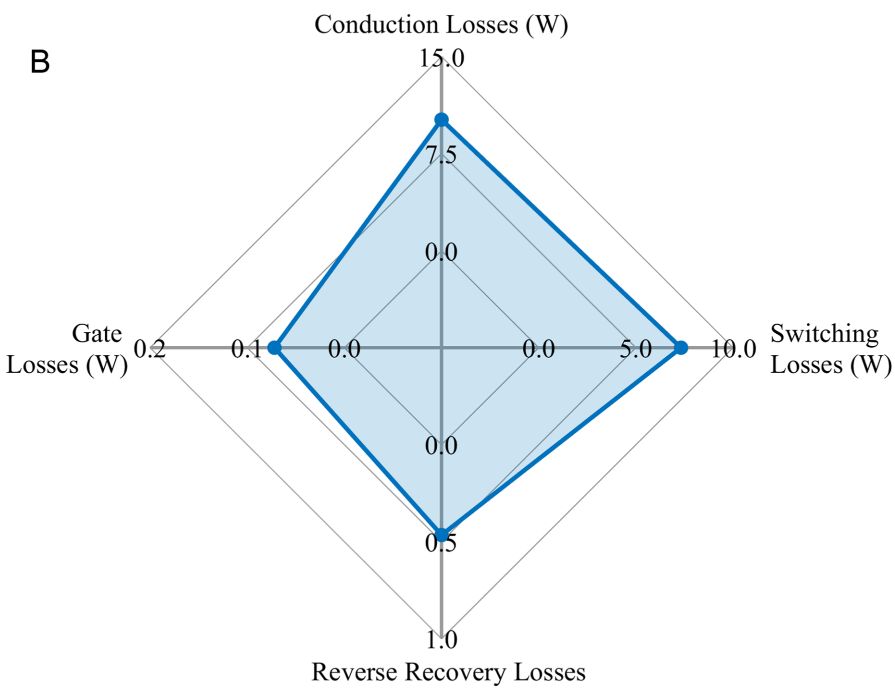

Fig. 10. (a) Total losses of the efficiency-constrained design. (b) Semiconductor losses of the efficiency-constrained design

capacitor results in the minimum loss value. In the graph of switching losses, it can be seen that the conduction loss is the greatest, followed by switching loss, and reverse recovery loss is the least.

In the efficiency-constrained design, the total loss is 20.44 W, the total price is $20.56 (inductance not included), and the efficiency is calculated as 95.9%.

V. DISCUSSION

This study proposes a new approach to the design of a four-switch buck-boost converter with a high-power density under efficiency and cost constraint for the LEV. In this study, an algorithm that can choose components for the design based on chosen constraints is proposed. In order to test the performance of the proposed algorithm, two different four-switch buck-boost converters that are fed by a 48 V battery and have output 500 W at 96-12-5 V are designed. The mathematical infrastructure of the suggested design algorithm is given and its fundamental concepts are presented. The copper and core losses of the inductor, losses of the output capacitor and the conduction, and switching losses of the switches are calculated. The reverse recovery losses of the body diodes of the MOSFET and gate losses of the MOSFET are calculated separately. The switches, inductor, and capacitor required to obtain the lowest possible converter losses or the lowest price were selected from a database with the proposed algorithm. Since the price for the inductor core was not available, the algorithm chose the same inductor core for both cases. Junction temperature of the semiconductor switches is decided to be 125°C, while the ambient temperature is 40°C. For this operation, the required heat sink thermal resistance calculations are made. The loss tables and radar charts for the losses are given for 100 kHz operation. It was seen that the MOSFET losses and its conduction losses were the most dominant losses. For the price-constrained design, a $5.34 four-switch buck boost converter with 52.25 W total loss and 89.55% efficiency and for the efficiency-constrained design a $20.56 four-switch buck boost converter with 20.44 W total loss and 95.9% efficiency are designed.

Peer-review: Externally peer-reviewed.

Declaration of Interests: The author has no conflicts of interest to declare.

Funding: The author declared that this study has received no financial support.

REFERENCES

1. B. Bilgin, A. Emadi, and M. Krishnamurthy, "Design considerations for a universal input battery charger circuit for PHEV applications," IEEE International Symposium on Industrial Electronics, 2010, pp. 3407–3412. [CrossRef]
2. B. Lin, "Analysis and implementation of a frequency control DC–DC converter for light electric vehicle applications," *Electronics*, vol. 10, no. 14, p.1623, 2021. [CrossRef]
3. A. Lordoglu, M. O. Gulbahce, D. A. Kocabas, and S. Dusmez, "System-Level Design Approach for LLC Converters," PCIM Europe Digital Days 2021; International Exhibition and Conference for Power Electronics, Intelligent Motion, Renewable Energy and Energy Management. 2021, pp. 1–8.
4. O. Akin, C. Bilgin, S. Celik, and M. O. Gulbahce, "Design of Four-Switch Buck-Boost Converter with High Efficiency for Light Electric Vehicle Applications," ELECO 2022 National Conference on Electrical, Electronics and Biomedical Engineering, 2022, pp.1-7.
5. C. Nan, T. Yao, and R. Ayyanar, "A 1 MHz eGaN FET based 4-switch buck-boost converter for automotive applications," 3rd Workshop on Wide Bandgap Power Devices and Applications (WiPDA). IEEE Publications, 2015. [CrossRef]
6. L. L. O. Carralero, G. S. Barbara da S. e Silva, F. F. Costa, and A. P. N. Tahim, "PV emulator based on a four-switch buck-boost DC-DC converter," 15th Braz. Power Electron. Conference and 5th IEEE Southern Power Electronics Conference (COBEP/SPEC). IEEE Publications, 2019. [CrossRef]
7. M. Schulz, N. Schleippmann, K. Gosses, B. Wunder, and M. Marz, "Four Switch buck/boost converter for DC microgrid applications," 22nd Eur. Conference on Power Electronics and Applications (EPE'20 ECCE Europe), 2020, pp. 1–10. [CrossRef]
8. Q. Liu, Q. Qian, M. Zheng, S. Xu, W. Sun, and T. Wang, "An improved quadrangle control method for four-switch buck-boost converter with reduced loss and decoupling strategy," *IEEE Trans. Power Electron.*, vol. 36, no. 9, pp. 10827–10841, 2021. [CrossRef]
9. Y. Bai, S. Hu, Z. Yang, Z. Zhu, and Y. Zhang, "Model predictive control for four-switch buck-boost converter based on tuning-free cost function with smooth mode transition," *IEEE J. Emerg. Sel. Top. Power Electron.*, vol. 10, no. 6, pp.6607–6618, 2021. [CrossRef]
10. K. Kim, H. Lee, S. Hong, and G. Cho, "A noninverting buck–boost converter with state-based current control for li-ion battery management in mobile applications," *IEEE Trans. Ind. Electron.*, vol. 66, no. 12, pp.9623–9627, 2019. [CrossRef]
11. "MAGNETICS Core Selector Charts Access Address". Available: https://www.mag-inc.com/getattachment/Design/Design-Guides/Inductor-Design-with-Magnetics-Powder-Cores/CoreSelectionChart2017.pdf?lang=en-US.
12. D. Graovac, M. Purschel, A. Kiep, and M. Power, *Losses Calculation Using the Data-Sheet Parameters / Infineon: Application Note 2006–07, V1.1*. Infineon Technologies AG, 2006, p. 23.

cigre Turkey

TEPES
TURKISH JOURNAL OF
ELECTRICAL POWER
AND ENERGY SYSTEMS

TEPES, Vol. 3, Issue. 1, 39-46, 2023 **DOI:** 10.5152/tepes.2023.23002

RESEARCH ARTICLE

Economic and Environmental Analysis of Grid-Connected Rooftop Photovoltaic System Using HOMER

Mikail Pürlü, Umut Özkan

Department of Electrical and Electronic Engineering, Sivas Cumhuriyet University, Sivas, Turkey

Cite this article as: M. Pürlü, U. Özkan, "Economic and environmental analysis of grid-connected rooftop photovoltaic system using HOMER," *Turk J Electr Power Energy Syst.*, 2023; 3(1), 39-46.

ABSTRACT

Due to the increasing energy demand and the climate crisis in the world, the importance of alternative energy generation techniques, which are clean and cheap, is increasing. Since renewable energy sources are clean and sustainable, their integration into the grids at transmission or distribution levels as distributed generation sources provides significant benefits both economically and environmentally. Rooftop solar panels are also an application of small-power renewable distributed generation technologies. In this study, the economic and environmental analysis of the rooftop photovoltaic system designed to increase the green energy usage rate and reduce the greenhouse gases released to the environment has been made. Considering the electricity consumption data and roof area of an office building of a factory located in the north of Turkey, solar radiation data obtained from three different sources such as the General Directorate of Meteorology, National Aeronautics and Space Administration, and Photovoltaic Geographical Information System were used during the analyses carried out in the Hybrid Optimization Models for Energy Resources program. By providing an annual average of 160 000 kWh (11%) clean energy generation, the annual release of pollutants such as 101.353 kg of carbon dioxide, 0.439 kg of sulfur dioxide, and 0.215 kg of nitrogen oxide to the environment has been prevented.

Index Terms— HOMER, grid connected, renewable energy.

I. INTRODUCTION

The world has been struggling with two major problems, energy crisis and climate crisis, for decades [1]. Microgrid and nanogrid applications, in which renewable energy sources (RESs) are integrated, have become increasingly popular in order to meet the increasing energy demand of societies with large populations and reduce their carbon footprint. Off-grid (standalone) hybrid energy systems (HES), which are independent of the grid and include RESs, non-renewable energy sources, and energy storage systems (ESSs) together, are one of the most suitable solutions for electrification of undeveloped or rural areas that are far from the grid or where there is no electricity grid. On-grid (grid-connected) HESs are designed with concerns such as increasing the renewable fraction, emission mitigation, voltage profile improvement, technical loss reduction, and meeting energy demand reliably.

HESs include RESs such as solar, wind, biomass, and geothermal and hydro energy, fossil fuel-based production technologies such as diesel generator (DG), and ESSs such as batteries, pumped storage, and flywheel, which are suitable for the design region. The selection, sizing, and placement of the correct components are performed as a result of the analyses made to provide technical, economic, and environmental contribution.

Many optimization algorithms and tools are used to design HESs. Also, various computer simulation software are available to analyze HESs, and their features can be summarized as in Table I [2].

In order to provide cheaper electricity to Burkina Faso, off-grid microgrid design including battery, photovoltaic (PV), maximum power point tracking, and inverter has also been realized in Hybrid Optimization Models for Energy Resources (HOMER) pro [3]. A renewable HES based on PV/fuel cell/battery energy storage system (BESS) to support the irrigation of paddy fields in Bihar, India, was designed and modeled in the LabVIEW environment [4]. Using genetic algorithm, particle swarm optimization algorithm, and artificial bee colony algorithms, the authors in [5] designed a HES with PV/BESS/DG for a region in Southwest Nigeria. In [6], off-grid and

Corresponding author: Mikail Pürlü, **E-mail:** mikailpurlu@cumhuriyet.edu.tr

Received: January 2, 2023
Accepted: January 11, 2023
Publication Date: February 15, 2023

TABLE I.
SIMULATION PROGRAMS FOR THE DESIGN OF ENERGY SYSTEMS

Software	Wind	Solar	Free trial	Technical	Economic	Optimization
RETScreen	✓	✓	✓	✓	✓	×
Hybrid2	✓	✓	✓	✓	×	×
SolSim	×	✓	×	✓	✓	✓
HYBRIDS	✓	✓	×	✓	×	✓
HYDROGEMS	✓	✓	×	✓	✓	✓
TRNsys	✓	✓	✓	✓	×	×
Ihoga	✓	✓	×	✓	✓	✓
pvSYSST	×	✓	✓	✓	×	✓
SAM	✓	✓	✓	✓	✓	×
HOMER	✓	✓	✓	✓	✓	✓

on-grid HESs based on PV/wind turbine/hydropower plant/hydrogen storage system for a rural area in Turkey were designed using the HOMER software. HES designs consisting of all and different combinations of PV/biogas generator/DG/BESS for a village in Xuzhou, China, were carried out in HOMER and compared in terms of cost and emissions [2].

To meet the energy demand of Maulana Azad National Institute of Technology Campus in Bhopal, Madhya Pradesh, India, the battery-included and off-grid rooftop PV system was designed using software such as SAM, Sunny Design, and Blue Sol [7]. Hillshade analysis was used to design an on-grid rooftop solar energy system for the building in Gangnam, Korea [8]. PVsyst and HOMER [9], PV*SOL, PVGIS, SolarGIS, and SISIFO [10] were used to analyze the performance of grid-connected rooftop PV systems.

In this paper, the design of a feasible grid-connected rooftop PV system, which takes into account real constraints such as roof area, component constraints, and annual load variation, is carried out in the HOMER program. This system, which is designed to provide emission mitigation and minimum energy costs, is modeled in Fig. 1. The design does not include any ESS, and when solar generation does not meet demand, energy is purchased from the grid, while excess solar energy is sold to the grid.

Main Points

- Increasing the use of renewable energy and reducing dependency on the grid and hence the dependence on fossil fuels.
- Providing more reliable analysis by using solar radiation data from three different sources such as the General Directorate of Meteorology, NASA, and PVGIS.
- Obtaining a feasible design by using real limit values such as roof area, photovoltaic panel dimensions, and component costs.
- Analyzing economic and environmental contributions using HOMER.
- As a future work, it is recommended to strengthen the design with components such as rooftop/wall-mounted wind turbines and battery energy storage systems.

The remainder of this paper is organized as follows. In Section II, the HOMER software and selected components are explained with their mathematical models. Section III covers the study location, energy consumption profile, and solar radiation data. The economic and environmental analysis of the grid-connected rooftop PV system is given in Section IV. Finally, the conclusion of this study and future work proposal are included in Section V.

II. METHODOLOGY AND COMPONENT MODELLING

A. HOMER Software

In this study, the HOMER software was used for rooftop PV system design and analysis. HOMER is an optimization tool developed by National Renewable Energy Laboratory for microgrid designs [11, 12]. Imitation, optimization, and sensitivity analysis are the basic functions in the HOMER software. HOMER considers the power

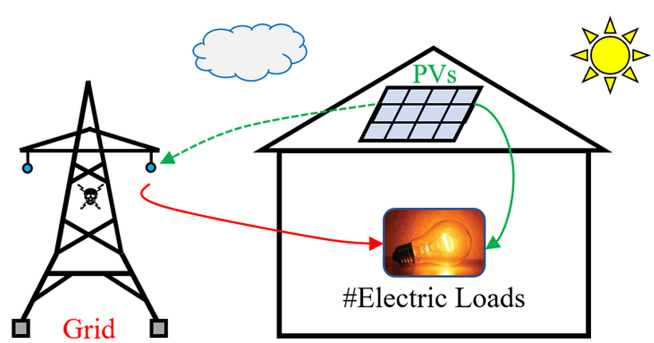

Fig. 1. Modeling of grid-connected rooftop PV system.

balance, load profile, location-specific tools, and system components all together and comprehensively and use the performance indicator such as cost of unit energy (CoE), net present cost (NPC), operational cost (OC), and initial cost [13].

CoE, which represents the cost of producing 1 kWh of electrical energy (unit energy), is the most critical indicator and is calculated as follows [14]:

$$CoE(\$/kWh) = \frac{TAC(\$/\text{year})}{TAEC(kWh/\text{year})} \tag{1}$$

where TAC represents the total annual cost and TAEC represents the total energy consumption per year.

NPC is the total of all expenses including capital, replacement, operation and maintenance, and fuel expenditures minus the salvage cost at the end of the project's lifetime. It is calculated as follows [13]:

$$NPC(\$/\text{year}) = \frac{TAC(\$/\text{year})}{CRF} \tag{2}$$

$$CRF(i,n) = \frac{i(1+i)^n}{(1+i)^n - 1} \tag{3}$$

where the capital recovery factor is represented by CRF, *i* is equal to the interest rate (%), and *n* is the lifetime of the components (year).

OC is calculated from the difference between the capital investment and the total annual cost and is expressed as follows [13, 14]:

$$OC(\$/\text{year}) = TAC(\$/\text{year}) - ACC(\$/\text{year}) \tag{4}$$

where ACC refers to the annual capital cost.

The solar savings fraction or solar fraction is the ratio of the energy supplied to the system by the PV panels to the total demand of the system and is calculated as a percentage as follows:

$$f_{solar} = \frac{E_{solar}}{E_{solar} + E_{grid}} \times 100 \tag{5}$$

where f_{solar} is the solar savings fraction, E_{solar} is the amount of solar energy generation, and E_{grid} is the amount of energy supplied from the grid.

B. PV Module

Since radiation and temperature are not constant in PV systems, also known as solar power systems, the output power also varies with time and can be calculated as follows:

$$P_{pv}(t) = N_{pv} \cdot P_{pv_r} \cdot f_{pv} \cdot \frac{G(t)}{G_n}\left[1 + \alpha_p\left(T_C(t) - T_{C_n}\right)\right] \tag{6}$$

where $P_{pv}(t)$ is the power output of the solar power system at time *t* (kW), N_{pv} is the number of the PV modules, P_{pv_r} is the nominal power of each PV module (kW), f_{pv} is the PV derating factor (%), $G(t)$ is the irradiation at the operating temperature at time *t* (kW/m^2), G_n is the irradiation at the standard test condition $(1kW/m^2)$, α_p is the temperature coefficient (%/°C), $T_C(t)$ is the cell temperature at time t (°C), and T_{C_n} is the nominal operating (test condition) temperature of the PV module (25°C).

TABLE II.
DATA OF SELECTED PV MODULES

Parameter	Specification
Manufacturer	Solar Energy SE 250/60P
Cell type	6″ polycrystalline
Cell dimension (H/W) (mm)	156 × 156
Number of cells	60 (10 × 6)
Panel dimension (H/W/D) (mm)	1640 × 992 × 40
Maximum power (W_p)	250
Weight (kg)	18
Open circuit voltage [U_{oc}] (V)	38.7
Short circuit current [I_{sc}] (A)	8.7
Voltage at maximum power [U_{mpp}] (V)	30.5
Current at maximum power [I_{mpp}] (A)	8.2
Panel efficiency (%)	15.4
Capital cost ($/kWp)	67.5
Replacement cost ($/kWp)	54
O&M cost ($/kWp/year)	10
Lifetime (years)	25

O&M, operating and maintenance; PV, photovoltaic.

TABLE III.
DATA OF THE INVERTER

Parameter	Specification
Manufacturer	CHINT POWER CPS SC100KT
Efficiency (%)	97.6
Capital cost ($/kWp)	8100
Replacement cost ($/kWp)	8100
O&M cost ($/kWp/year)	15
Lifetime (years)	15

O&M, operating and maintenance.

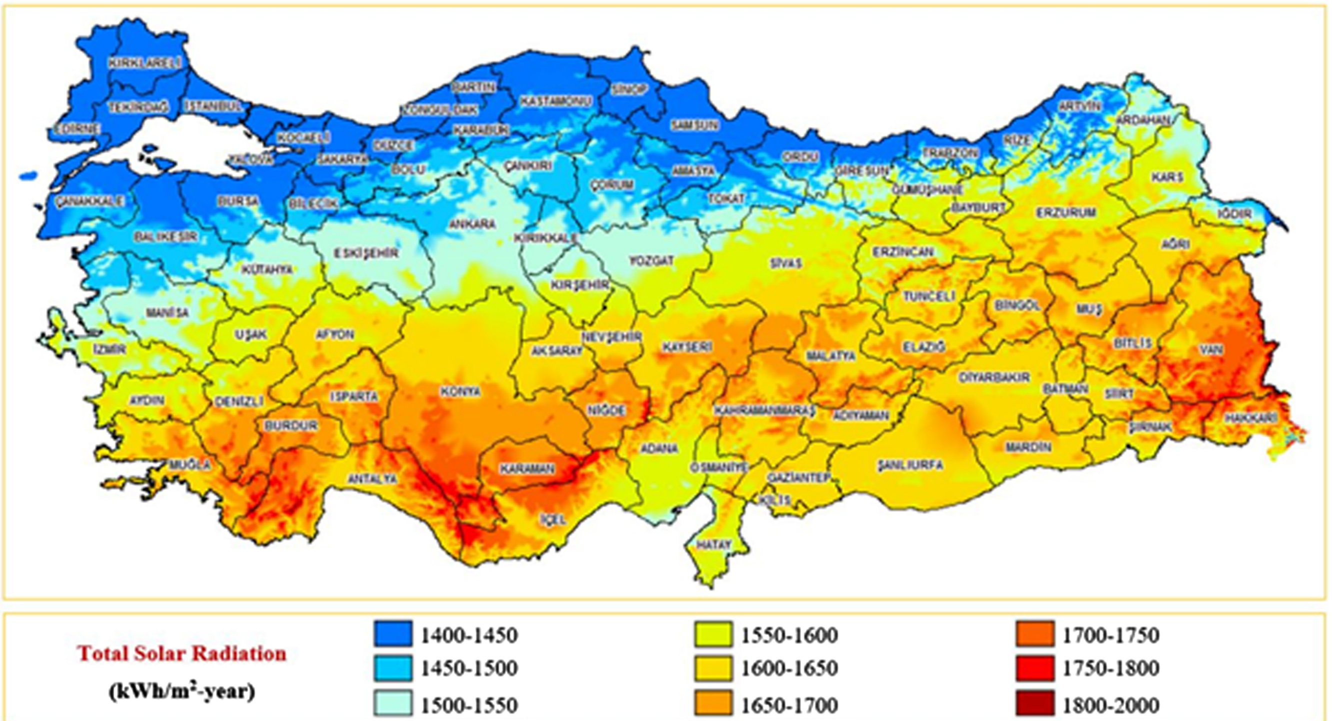

Fig. 2. Turkey's solar energy potential map.

In this study, the Solar Energy SE 250/60P model was selected from the HOMER database as the PV modules. Technical and economic data for the PV are given in Table II.

C. Converter

There are two types of energy conversion devices in HESs. The first converts from DC to AC and is called the inverter. The second converts from AC to DC and is called the rectifier [15].

In this study, the CHINT POWER CPS SC100KT model was selected from the HOMER database as the converter. Data for the converter are given in Table III.

III. STUDY LOCATION AND DATA

In this study, a grid-connected rooftop PV system was designed for the office building of a factory in Çerkezköy city, Tekirdağ province in Turkey. The location of Tekirdağ province and the solar potential map of Turkey are shown in Fig. 2 [16]. The office is located at 41°16′43′′ North latitude and 27°58′54′′ East longitude. Approximately 200 people work in the office building, which consists of office areas and test rooms, and electricity consumption is higher, especially between 08:00 and 18:00 during working hours. The monthly electricity consumption in the building in 2019 and 2020 is shown in Table IV and compared in Fig. 3.

Fig. 3 shows that the highest electricity consumption was in July for both years. This is due to the increase in air conditioning usage with the increase in temperatures in the summer months. On the other hand, there is a decrease in the electricity consumption data of 2020 compared to the consumption data of 2019, and this is explained as a result of the efforts made to save energy in the building.

TABLE IV.
MONTHLY TOTAL ELECTRICITY CONSUMPTION DATA OF THE OFFICE BUILDING

Months	2019 (kWh)	2020 (kWh)
January	103 638	117 092
February	96 694	108 310
March	113 292	111 533
April	106 081	96 744
May	128 826	97 139
June	132 056	115 020
July	136 603	141 758
August	136 551	134 996
September	135 407	137 504
October	123 919	129 012
November	123 043	106 771
December	118 212	105 861
Annual total	1 454 322	1 401 740

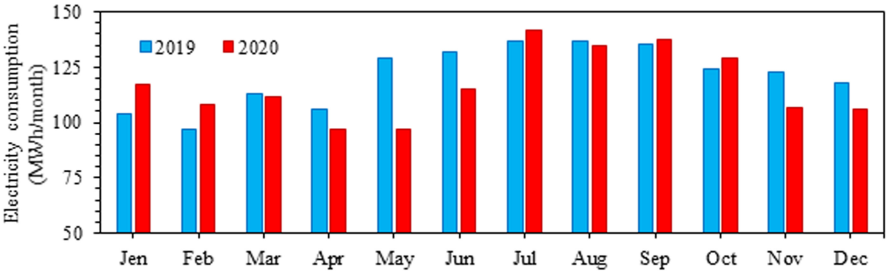

Fig. 3. Monthly electricity consumption data for 2019 and 2020.

In the HOMER software, it is required to enter the daily electricity consumption data hourly. By dividing the monthly consumption data by the number of days in each month, the average daily consumption data for each month can be obtained, and the average of these calculated values is equal to the average daily consumption of the whole year. The calculated average daily consumption values are given in Table V, and HOMER analyses were performed by taking the general average daily consumption of 3900 kWh.

Tekirdağ province temperature data is shown in Fig. 4, and the measurement period covers the years 1939–2020. By taking the average of the monthly temperature values measured during these years, the average temperature was determined as 14.1°C [17].

The measurement intervals for radiation data from the General Directorate of Meteorology (GDM), NASA, and PVGIS cover the years 2004–2018, 1983–2005, and 2005–2016, respectively. The average daily irradiance values were calculated as 3.92 kWh/m^2/day, 3.93 kWh/m^2/day, and 4.20 kWh/m^2/day, respectively. The average daily radiation and clearness indexes for the office building are shown in Fig. 5.

TABLE V.
DAILY AVERAGE ELECTRICITY CONSUMPTION DATA OF THE OFFICE BUILDING

Months	2019 (kWh)	2020 (kWh)
January	3343.16	3777.16
February	3453.36	3734.83
March	3654.58	3597.84
April	3536.03	3224.80
May	4155.68	3133.52
June	4401.87	3834.00
July	4406.55	4572.84
August	4404.87	4354.71
September	4513.57	4583.47
October	3997.39	4161.68
November	4101.43	3559.03
December	3813.29	3414.87
Annual average	3981.81	3829.06

IV. ANALYSIS AND RESULTS

From the image obtained from the Google Earth system, the PV panel applicable roof area was calculated as 2613.75 m^2. The roof area was divided into six parts named A, B, C, D, E, and F as shown in Fig. 6, and a separate module layout calculation was made for each area. While placing the PV modules, the modules were placed facing south in terms of location. The area, number of panels, and installed power are calculated for each zone and listed in Table VI.

Solar modules with 250 W power were used for the system design. The total number of modules calculated for the system is 485. Considering the power of the PV module used, it is predicted that the installed power of the system will be 485 × 250 = 121.250 kW.

HOMER designs the system by taking into account the economic data. The economic data entered are important for the accuracy of the simulation. As economic data, interest rate, inflation, real

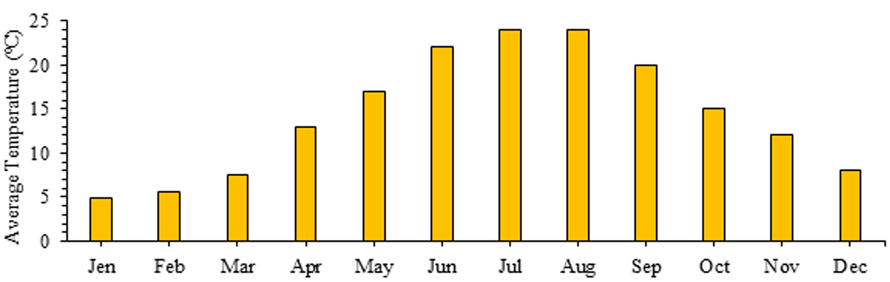

Fig. 4. Monthly average temperature values.

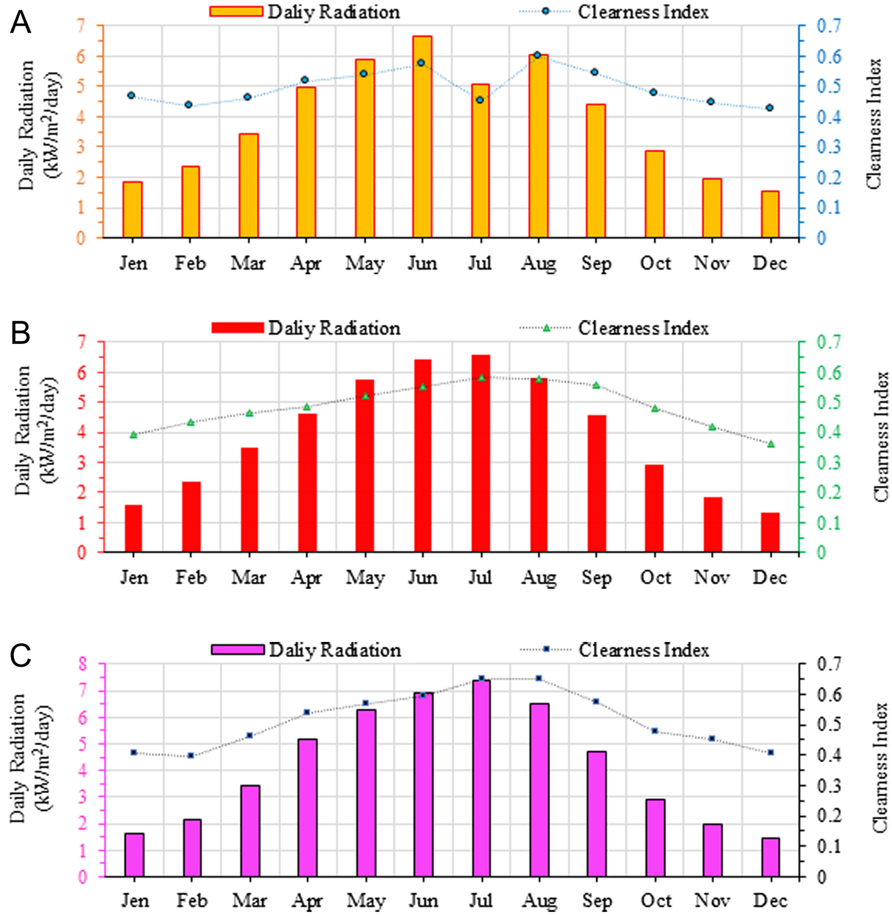

Fig. 5. Solar radiation data and clearness indexes from a) GDM, b) NASA, c) PVGIS.

interest rate, and project life data are required. Project life is taken as 25 years. This period is determined as the lifetime of the PV panel. Considering the data of the Central Bank of the Republic of Turkey for the last 10 years, the interest rate is 8% and the inflation rate is 10%. The real interest rate was found to be –1.82%. According to the electricity tariff effective as of April 1, 2021, announced by the Energy Market Regulatory Authority, the one-time electricity purchase price is 0.10634 $/kWh, and

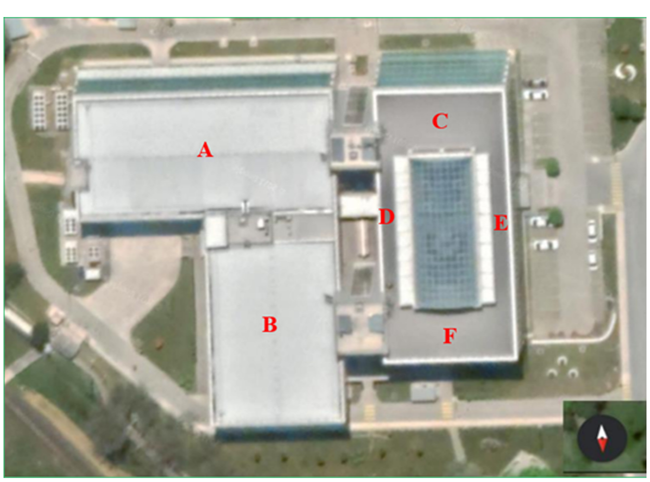

Fig. 6. Office building roof divided into 6 zones.

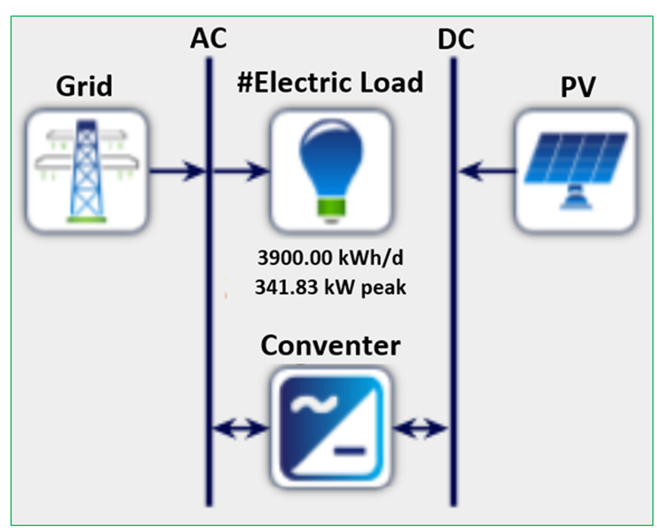

Fig. 7. On-grid PV system.

TABLE VI.
PLACEMENT OF PV MODULES IN REGIONS

Zone	Width (m)	Height (m)	Area (m²)	Number of arrays	Number of PVs in the array	Total number of PVs	Installed power (kWp)
A	46	24	1104	8	27	216	54
B	34	24	816	12	13	156	39
C	23.5	12.5	293.75	4	13	52	13
D	30	2.5	75	11	1	11	2.75
E	30	3	90	11	1	11	2.75
F	23.5	10	235	3	13	39	9.75
Total	–	–	2613.75	–	–	485	121.25

PV, photovoltaic.

TABLE VII.
THE RESULT OF THE COST ANAYLSIS

Data from	Component	Initial investment cost ($)	Replacement cost ($)	Operating & Maintenance cost ($)	Grid payment ($)	Scrap cost ($)	Total cost ($)
GDM	PV	121 250	0	38 816.20	0	0	160 066.20
	Grid	0	0	0	4 316 900.98	0	4 316 900.98
	Converter	21 375	28 142.52	41 057.13	0	11 272.19	79 302.46
	System	142 625	28 142.52	79 873.33	4 316 900.98	11 272.19	4 556 269.64
NASA	PV	121 250	0	38 816.20	0	0	160 066.20
	Grid	0	0	0	4 325 028.74	0	4 325 028.74
	Converter	21 375	28 142.52	41 057.13	0	11 272.19	79 302.46
	System	142 625	28 142.52	79 873.33	4 325 028.74	11 272.19	4 564 397.40
PVGIS	PV	121 250	0	38 816.20	0	0	160 066.20
	Grid	0	0	0	4 293 568.18	0	4 293 568.18
	Converter	21 375	28 142.52	41 057.13	0	11 272.19	79 302.46
	System	142 625	28 142.52	79 873.33	4 293 568.18	11 272.19	4 532 936.84

GDM, General Directorate of Meteorology; PV, photovoltaic.

TABLE VIII.
METRIC COMPARISON OF THE SIMULATION RESULT

Data from	PV (kW)	Converter (kW)	CoE ($/kWh)	NPC (M$)	OC ($)	IC ($)	Solar fraction (%)
GDM	121	85.5	0.1000	4.56	137 869	142 625	10.6
NASA	121	85.5	0.1000	4.56	138 123	142 625	10.5
PVGIS	121	85.5	0.0995	4.53	137 140	142 625	11.1

CoE, cost of energy; GDM, General Directorate of Meteorology; IC, initial cost; NPC, net present cost; OC, operating cost; PV, photovoltaic.

TABLE IX.
EMISSION COMPARISON BY DIFFERENT SOURCES OF RADIATION DATA

Emissions	Carbon dioxide (kg/year)	Sulfur dioxide (kg/year)	Nitrogen oxides (kg/year)
GDM	804.089	3.486	1.705
NASA	805.584	3.493	1.708
PVGIS	799.737	3.467	1.696

GDM, General Directorate of Meteorology.

the electricity sales price for unlicensed PV systems is 0.07354 $/kWh.

The system designed at HOMER to perform the economic and environmental analyses of the grid-connected rooftop solar energy system is shown in Fig. 7.

The results of the simulations made according to the GDM, NASA, and PVGIS data, cost analysis, and emission values are given in Tables VII, VIII, and IX, respectively.

Looking at these tables, since the roof area does not change, the number of PV, PV power, and converter power are the same for three different radiation data. Accordingly, the initial investment cost, replacement cost, operation and maintenance cost, and scrap costs of these components are the same. The solar fraction has increased in proportion to the average radiation value, and therefore the purchase of electrical energy from the grid has decreased. This situation led to a decrease in the total operating cost and thus a decrease in the CoE. In addition, for all three cases, the CoE is cheaper than the grid price, and there has been a significant reduction in emissions.

V. CONCLUSION

In this study, the economic and environmental benefits of installing a PV system with an installed power of 121.25 kW on the roof of a building in Çerkezköy, Tekirdağ, in Turkey were analyzed. Although the rooftop solar panel could not meet the entire energy demand of the office, a reduction of $8726 in annual bills and a reduction of 101.353 kg in emissions were calculated as a result of approximately 11% solar fraction obtained. It has been observed that even small applications of rooftop solar panels will have positive effects on our world in combating the devastating effects of both the energy crisis and the climate crisis. The renewable fraction and efficiency of the project can be increased by supporting the system with roof/wall type wind turbines or a suitable RES and ESSs.

Peer-review: Externally peer-reviewed.

Declaration of Interests: The authors haveno conflicts of interest to declare.

Funding: The authors declared that this study has received no financial support.

REFERENCES

1. M. Purlu, "Mikrobiyal Yakıt Hücreleri: Enerji Krizini Yenmek İçin Tercih Edilen Bir Teknoloji," içinde TEKNOBİLİM-2022: Enerji Krizi ve Yenilenebilir Enerji-II, C. Karaman, Ed. Türkiye; İstanbul: Efe Akademi Yayınları, 2022, ss. 83-100.
2. C. Li, L. Zhang, F. Qiu, and R. Fu, "Optimization and enviro-economic assessment of hybrid sustainable energy systems: The case study of a photovoltaic/biogas/diesel/battery system in Xuzhou, China," Energy Strategy Rev., vol. 41, p. 100852, 2022. [CrossRef]
3. Ö. Merev, "Feasibility of PV-based islanded microgrids for affordable electricity in sub-Saharan Africa," Turk J. Electr. Power Energy Syst., vol. 1, no. 2, pp. 60–68, 2021.
4. K. Buts, L. Dewan, and M. Prasad, "Design and control of a PV-FC-BESS-based hybrid renewable energy system working in LabVIEW environment for short/long-duration irrigation support in remote rural areas for paddy fields," Turk J. Electr. Power Energy Syst., vol. 1, no. 2, pp. 75–83, 2021.
5. T. O. Ajewole, O. Oladepo, K. A. Hassan, A. A. Olawuyi, and O. Onarinde, "Comparative study of the performances of three metaheuristic algorithms in sizing hybrid-source power system," Turk J. Electr. Power Energy Syst., vol. 2, no. 2, pp. 134–146, 2022.
6. M. Purlu, S. Beyarslan, and B. E. Turkay, "Optimal design of hybrid grid-connected microgrid with renewable energy and storage in a rural area in Turkey by using Homer," in 13th International Conference on Electrical and Electronics Engineering (ELECO), IEEE Publications, 2021, pp. 263–267. [CrossRef]
7. A. K. Shukla, K. Sudhakar, and P. Baredar, "Design, simulation and economic analysis of standalone roof top solar PV system in India," Sol. Energy, vol. 136, pp. 437–449, 2016. [CrossRef]
8. T. Hong, M. Lee, C. Koo, J. Kim, and K. Jeong, "Estimation of the available rooftop area for installing the rooftop solar photovoltaic (PV) system by analyzing the building shadow using hillshade analysis," Energy Procedia, vol. 88, pp. 408–413, 2016. [CrossRef]
9. N. Anang, S. N. A. Azman, W. M. W. Muda, A. N. Dagang, and M. Z. Daud, "Performance analysis of a grid-connected rooftop solar PV system in Kuala Terengganu, Malaysia," Energy Build., vol. 248, p. 111182, 2021. [CrossRef]
10. C. Dondariya et al., "Performance simulation of grid-connected rooftop solar PV system for small households: A case study of Ujjain, India," Energy Rep., vol. 4, pp. 546–553, 2018. [CrossRef]
11. J. Kumari, P. Subathra, J. E. Moses, and D. Shruthi, "Economic analysis of hybrid energy system for rural electrification using Homer," International Conference on Innovations in Electrical, Electronics, Instrumentation and Media Technology (ICEEIMT), IEEE Publications, 2017, pp. 151–156. [CrossRef]
12. S. Chauhan, R. Pande, and S. Sharma, "Techno-economic study of offgrid renewable energy system in Darma valley, Uttarakhand, India," Curr. Sci., vol. 9, p. 121, 2021.
13. M. Pürlü, S. Beyarslan, and B. E. Türkay, "On-grid and off-grid hybrid renewable energy system designs with Homer: A case study of rural electrification in Turkey," Turk J. Electr. Power Energy Syst., vol. 2, no. 1, pp. 75–84, 2022.
14. A. Abbassi, R. B. Mehrez, R. Abbassi, S. Saidi, S. Albdran, and M. Jemli, "Improved off-grid wind/photovoltaic/hybrid energy storage system based on new framework of Moth-Flame optimization algorithm," Int. J. Energy Res., vol. 46, no. 5, pp. 6711–6729, 2022. [CrossRef]
15. J. Huang, W. Li, L. Guo, X. Hu, and J. W. Hall, "Renewable energy and household economy in rural China," Renew. Energy, vol. 155, pp. 669–676, 2020. [CrossRef]
16. GEPA [online]. Available: https://gepa.enerji.gov.tr/MyCalculator/Default.aspx.
17. Meteoroloji Genel Müdürlüğü [online]. Available: https://www.mgm.gov.tr/veridegerlendirme/il-ve-ilceler-istatistik.aspx?m.

TEPES
TURKISH JOURNAL OF
ELECTRICAL POWER
AND ENERGY SYSTEMS

TEPES, Vol. 3, Issue. 1, 47-60, 2023 **DOI:** 10.5152/tepes.2023.23001

RESEARCH ARTICLE

Sensitivity and Cost Analysis of a Microgrid With a Day-Ahead Energy Management System

Sezai Polat[1], Emrah Bıyık[2], Hacer Şekerci Öztura[3]

[1]Department of Electrical and Electronics Engineering, Graduate School, Yaşar University, İzmir, Turkey
[2]Department of Energy Systems Engineering, Yaşar University, İzmir, Turkey
[3]Department of Electrical and Electronics Engineering, Yaşar University, İzmir, Turkey

Cite this article as: S. Polat, E. Bıyık and H. Şekerci Öztura, Sensitivity and cost analysis of a microgrid with a day-ahead energy management system, *Turk J Electr Power Energy Syst.,* 2023; 3(1), 47-60.

ABSTRACT

The use of renewable energy sources (RESs) can ensure both lower cost of energy and improvement in voltage levels in the grid. Likewise, batteries can help achieve technical improvement and cost reduction. However, the full benefits of integrating RESs and batteries into the grid can only be realized by a suitable energy management system (EMS). In this work, a predictive EMS is developed to optimally operate a microgrid (MG) with photovoltaics and batteries while satisfying voltage constraints in the distribution grid. First, mathematical models of the MG components are obtained. Then, proper load flow method is selected for the network structure. Using component models and the load flow method, a day-ahead EMS is posed as an optimization problem. Since the power flow calculations are nonlinear, the optimization problem is constructed as a nonlinear program. Simulation studies are performed to analyze the sensitivity of the cost of operation and power loss in the grid, with respect to different system parameters. It is confirmed that the purchase price of electricity and the amount of photovoltaic panels were the most effective factors on the daily energy cost.

Index Terms— Battery, day-ahead, microgrid

I. INTRODUCTION

The share of renewable energy sources (RESs) which represents the sum of solar and wind energies in the world increased from 2% in 2011 to 10% in 2021 [1]. Increasing use of renewable energy can help to reduce the energy costs as well as energy loss. Besides these benefits, some technical issues arise with the integration of distributed generation (DG) [2]. The increase in the number of equipment used, such as photovoltaic (PV) panel, wind turbine, and battery, complicates power dispatch problem [3]. The power dispatch problem can be solved by day-ahead scheduling [4]. There are some technical limits and constraints that should be taken into account while tackling this problem. In order to offer cost-effective and technical options to power systems, day-ahead energy management systems (EMSs) are frequently used. Since the effect of energy sources and loads on system security should be estimated, power flow calculations (PFCs) are important for power dispatch scheduling in EMS. Power flow calculation needs to be considered when operating within technical limits and achieving low energy cost in grid.

There are different methods developed in the literature for PFCs [5]. In [6], the authors analyzed the reduction of energy cost in a radial distribution system (RDS) by using the DistFlow PFC method. In [7], the authors carried out a study aiming to reduce energy costs in an RDS with different DG sources by using direct current PFC. In [8], instead of cost minimization, line loss and voltage fluctuations were aimed to be minimized by using the Newton–Raphson PFC method. In [9], the authors carried out a study aimed at minimizing the total voltage regulation cost for RDS, including mobile battery system and on-load tap changer, by using the DistFlow method. Another PFC method is a direct approach-based load flow solution. [10]. In addition to energy cost reduction, PFC is also used for the placement problem of the DG [11], for the optimum operation of the battery [12], for the improvement of voltage profile [13], for optimal network reconfiguration in [14], and for optimal placement of battery storage systems and capacitor banks in grid [15].

Forecast of energy cost is as important as estimation for staying within electrical specifications. Therefore, EMS optimization is a

Corresponding author: Sezai Polat, **E-mail:** sezaipolat@gmail.com

Received: January 2, 2023
Accepted: January 18, 2023
Publication Date: February 28, 2023

very important issue. Day-ahead EMS performs economic dispatch for each hour of the following day. A robust and efficient PFC method is required when considering the number and size of the system equipment. Direct approach-based load flow solution is a rapid and enough precision method for RDS [16, 17].

To this direction, integration of PV and battery energy storage systems (BESSs) into the grid can help to decrease energy cost and energy losses and improve voltage profiles [18, 19].

This study aims to decrease the energy cost by integrating PVs and BESSs into the IEEE 33 bus test system. The decrease in the daily operating cost includes minimizing the line losses, the cost of energy bought from the grid, and the BESS operating cost and maximizing the revenue of sales to the grid. In this paper, various simulation studies are carried out by creating an optimization model that purposes at the lowest energy cost and losses without exceeding the voltage limits of buses for 24 h, according to the load and RESs obtained by day-ahead EMS.

This paper expands the work reported in [20] in three directions: 1) comparison of the power flow algorithm with the literature, 2) minimization of power loss and daily energy cost, and 3) sensitivity analysis of the cost and power loss characteristics of the EMS.

The major contributions of this study, as compared to similar studies, are:

1) Tackling operational cost optimization and power quality (voltage regulation) concurrently in the EMS by using the distribution load flow (DLF) technique for a multi-period power flow in a microgrid (MG).
2) Analyzing the effects of system parameters (electricity prices, PV parameters, and BESS cost and capacities) for sensitivity analysis for daily energy cost and power loss.

The rest of this paper is organized as follows. The MG structure is presented in Section II. Power flow analysis is stated in Section III. Section IV presents the day-ahead optimization model of a MG. The case studies, analysis of the results, and sensitivity analysis are given in Section V. Lastly, conclusions are given in Section VI.

Main Points

- A predictive energy management system (EMS) is developed to optimally operate a microgrid with photovoltaics (PVs) and battery energy storage systems (BESSs), while voltage constraints are satisfied in the distribution grid.
- The operational cost optimization and power quality (voltage regulation) are tackled concurrently in the EMS by using the distribution load flow technique for a multi-period power flow.
- The effects of the system parameters (e.g., electricity prices, PV parameters, and BESS cost and capacities) are analyzed for sensitivity analysis, daily energy cost, and power loss.

II. MICROGRID

The MG is defined Distributed Energy Resources (DER) and interconnected loads, whose electrical properties are defined within certain limits, which can be controlled and acted as a single controllable network equipment [21]. A simple structure of an MG is shown in Fig. 1.

Microgrids may include RESs such as PV and wind energy when geographic location is considered. In addition, it may also include a battery and/or generator to supply the energy requirement of the load uninterruptedly at a lower cost.

An EMS fulfills the role to supply the loads within electrical technical limits in the MG. In addition, EMS objectives include reducing the cost of energy and even making a profit. In other words, the MG needs a control system which is responsible for operating the equipment optimally while fulfilling the required quality parameters of electricity.

The day-ahead planning allows power dispatch in the MG for the following day by using RES forecast and load forecast data. This planning should calculate the power generations, loads, and energy loss in the MG.

Because of the reasons explained above, a precise and simple modeling is the most important issue for EMS. In this study, mathematical models are formulated for objective function, including constraints, PV model, BESS model, and PFC for MG and also for constraints.

A. Photovoltaic System

Different calculation methods for PV power output estimation were investigated in [22, 23]. However, (1) can be used for PV power calculation at time t for its simplicity, low computational burden, and faster computation [24]. Photovoltaics generate electricity in a direct proportion to the global solar radiation and surface area by means of (1).

$$P_t^{PV} = \eta_{pv}.A_{pv}.G_t^{PV} \qquad \forall t \tag{1}$$

where P_t^{PV} is the generated power by PV panel, η_{Pv} and A_{Pv} are the efficiency and area of PV panel, respectively, and G_t^{PV} is the solar irradiance.

B. Battery Energy Storage System

Renewable energy source power outputs may be intermittent because of the uncertain nature of renewable energy. Battery energy store system can be used for energy supply when energy generation is intermittent and fluctuating. Additionally, BESS can provide economic benefits because it can reduce the cost of the energy purchased from the grid and increase the sales revenue to the grid. The energy balance in the BESS is given in (2) [25].

$$SoC_{t+1}^{BESS} = SoC_t^{BESS} + \eta_{BC}.P_t^{BC}.\Delta t - \frac{P_t^{BD}}{\eta_{BD}}.\Delta t \qquad \forall t \tag{2}$$

where SoC_t^{BESS} means the battery state of charge. η_{BC} and η_{BD} are the charge/discharge efficiency of the BESS. P_t^{BC} and P_t^{BD} are charge/discharge power of the BESS, and Δt is the time interval.

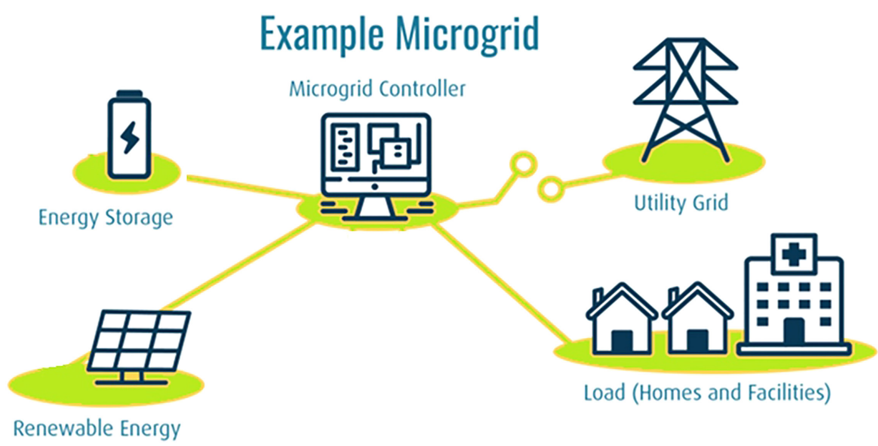

Fig. 1. Structure of studied MG in this paper (modified from [22]).

BESS charge and discharge powers must be within a certain range in (3) and (4).

$$0 \leq P_t^{BC} \leq P^{BC,max} \qquad \forall t \tag{3}$$

$$0 \leq P_t^{BD} \leq P^{BD,max} \qquad \forall t \tag{4}$$

where $P^{BC,\max}$ and $P^{BD,\max}$ are the maximum power of the BESS in charging/discharging mode, respectively.

III. POWER FLOW ANALYSIS

The Newton–Raphson, Gauss–Seidel, and fast-decoupled methods, which are known power flow models, cannot be applied because of the high R/X ratio of distribution systems [26]. These techniques do not give high precision results, and it takes a long time [27]. For this reason, other PFC methods are used for RDS in the literature. Distribution load flow is one of the mostly used methods for RDS [10].

A. Distribution Load Flow Method

The DLF method is recommended for RDS. In this method, calculations are carried out by creating the bus injection to branch current (BIBC) and the branch current to bus voltage (BCBV) matrices.

The apparent power is calculated at bus i at t time in a distribution network by (5).

$$S_{i,t} = P_{i,t} + jQ_{i,t} \qquad \forall t, i \tag{5}$$

where $P_{i,t}$ and $Q_{i,t}$ mean the active and reactive power at bus i, at time t, respectively.

Since the apparent power S_i and V_i voltage of bus i are known, the load currents I_i can be calculated by (6).

$$I_{i,t} = \left(\frac{S_{i,t}}{V_{i,t}}\right)^* \qquad \forall t, i \tag{6}$$

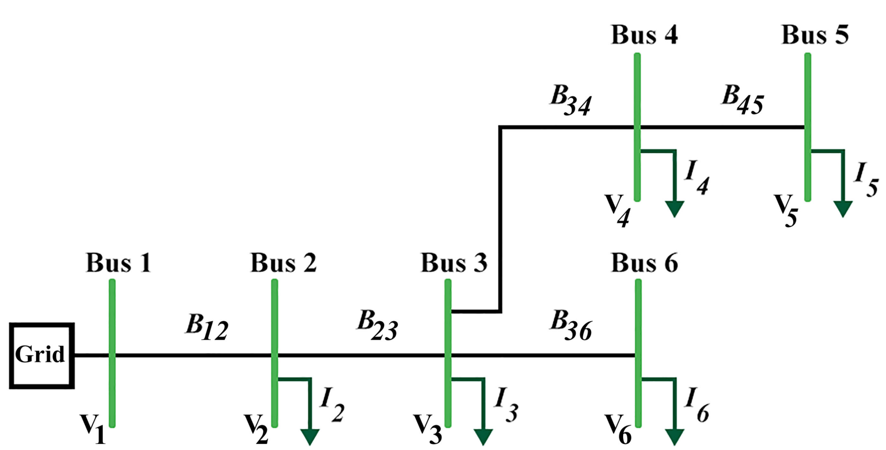

Fig. 2. Example of an RDS with six buses.

Fig. 2 represents a six-bus radial system. If the recommended DLF technique is applied, the calculation is performed in the following steps.

The line currents B_{ij} are calculated using the bus currents I_i, by applying Kirchhoff's law of currents. Line currents are obtained from (7);

$$\begin{aligned} B_{12} &= I_2 + I_3 + I_4 + I_5 + I_6 \\ B_{23} &= I_3 + I_4 + I_5 + I_6 \\ B_{34} &= I_4 + I_5 \\ B_{45} &= I_5 \\ B_{36} &= I_6 \end{aligned} \tag{7}$$

Equation (8) given above can be written in a matrix form as follows:

$$\begin{bmatrix} B_{12} \\ B_{23} \\ B_{34} \\ B_{45} \\ B_{36} \end{bmatrix} = \begin{bmatrix} 1 & 1 & 1 & 1 & 1 \\ 0 & 1 & 1 & 1 & 1 \\ 0 & 0 & 1 & 1 & 0 \\ 0 & 0 & 0 & 1 & 0 \\ 0 & 0 & 0 & 0 & 1 \end{bmatrix} . \begin{bmatrix} I_2 \\ I_3 \\ I_4 \\ I_5 \\ I_6 \end{bmatrix} \tag{8}$$

$$[B] = [BIBC].[I] \tag{9}$$

Equation (10) using line currents to calculate bus voltages is given below.

$$\begin{aligned} V_2 &= V_1 - B_{12}.Z_{12} \\ V_3 &= V_2 - B_{23}.Z_{23} \\ V_4 &= V_3 - B_{34}.Z_{34} \\ V_4 &= V_1 - B_{12}.Z_{12} - B_{23}.Z_{23} - B_{34}.Z_{34} \end{aligned} \tag{10}$$

where V_i is voltage magnitude at bus i and Z_{ij} is the line impedance between bus i and j. Similarly, the voltage difference in terms of line currents can be obtained from (11).

$$\begin{bmatrix} V_1 \\ V_1 \\ V_1 \\ V_1 \\ V_1 \end{bmatrix} - \begin{bmatrix} V_2 \\ V_3 \\ V_4 \\ V_5 \\ V_6 \end{bmatrix} = \begin{bmatrix} Z_{12} & 0 & 0 & 0 & 0 \\ Z_{12} & Z_{23} & 0 & 0 & 0 \\ Z_{12} & Z_{23} & Z_{34} & 0 & 0 \\ Z_{12} & Z_{23} & Z_{34} & Z_{45} & 0 \\ Z_{12} & Z_{23} & 0 & 0 & Z_{36} \end{bmatrix} . \begin{bmatrix} B_{12} \\ B_{23} \\ B_{34} \\ B_{45} \\ B_{36} \end{bmatrix} \tag{11}$$

$$[\Delta V] = [BIBC].[B] \tag{12}$$

$$\left[\Delta V\right] = \left[BCBV\right].\left[BIBC\right].\left[I\right] \tag{13}$$

$$[\Delta V] = [DLF].[I] \tag{14}$$

The voltage differences between first bus and other buses can be obtained by the DLF matrix consisting of BIBC and BCBV matrices. The voltage differences and voltage magnitude at all buses are calculated iteratively as follows:

$$\left[\Delta V^{k+1}\right] = \left[DLF\right].\left[I^k\right] \tag{15}$$

$$\left[V^{k+1}\right] = V^0 - \left[\Delta V^{k+1}\right] \tag{16}$$

Fig. 3 gives the flowchart of a PFC procedure.

The line current B_{ij} of each branch is calculated using PFC, and the losses in the lines can easily be calculated by using (17).

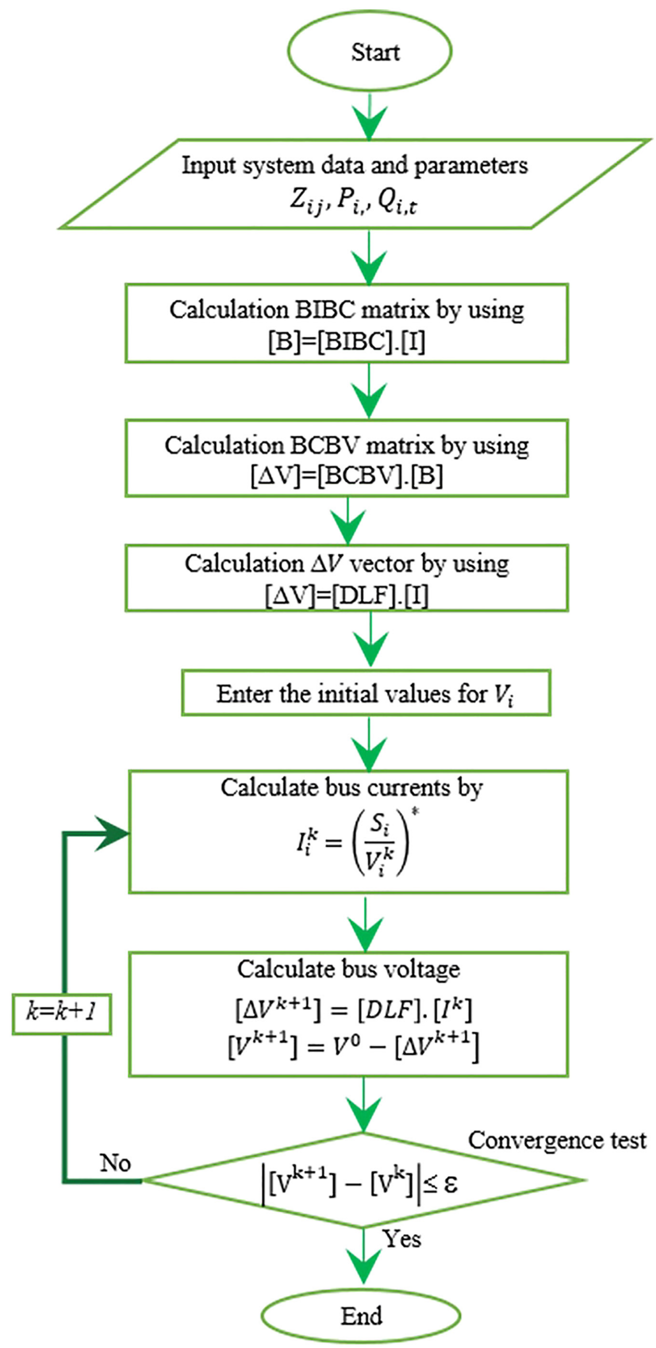

Fig. 3. Simplified flowchart of power flow.

$$P_{ij,t}^{loss} = r_{ij}.B_{ij,t}^{2} \qquad \forall i,j,t \tag{17}$$

where $P_{ij,t}^{loss}$, $B_{ij,t}$, and r_{ij} are line loss, line current at time t, and line resistance between bus i and j, respectively.

B. Demonstration of Distribution Load Flow Method

The recommended PFC is simulated on the IEEE 33 bus radial distribution test system in Fig. 4. The system has contains 32 lines and 33 buses, a voltage of 12.66 kV, 3.715 MW and 2.3 MVar load. The data of the test system can be seen in [11].

There are different power flow studies in the literature appropriate for the radial system. The new analytical formulations (analytical method) were developed for solving RDS in [14]. The backward and forward sweep method was presented in [28] for solving RDS. The dynamic data matrix method was proposed for calculating the voltages of buses by the authors in [29]. In [30], the authors proposed the direct backward/forward sweep solution technique to solve for PFC.

For the sake of recommended methodology (DLF technique) validation, the bus voltages and total power loss are tabulated in Table I and Table II, respectively. The comparison of voltages at each bus for different power flow methods is represented in Fig. 5.

It is seen that there is a negligible difference between the method applied in this study and the other methods. The used approach is validated with the results of the other methods in the test system.

This study is currently being expanded to include multi-period PFCs. In this paper, an optimization model to arrive at a day-ahead optimal plan for EMS is proposed and discussed. The model was simulated with historical weather data and forecasted load given in [31]. The forecasted load and power losses are depicted in Fig. 6. Total energy loss was calculated as 2733 kWh for 1 day.

IV. DAY-AHEAD OPTIMIZATION MODEL

A. The Objective Function

Fig. 7 illustrates the input–output scheme of a MG EMS system. It is aimed to minimize the operating costs by using the optimization problem in (18)–(20). The objective function includes minimizing expenses for power bought from grid, minimizing BESS operational cost, and maximizing revenue from selling to grid and also reducing line losses.

$$\min F = C_{GC} + C_{BC} \tag{18}$$

$$C_{GC} = \sum_{t=1}^{T}\left(\underbrace{P_t^{GB}.\lambda_t^{pp}}_{cost} - \underbrace{P_t^{GS}.\lambda_t^{SP}}_{revenue}\right).t \qquad \forall t \tag{19}$$

$$C_{BC} = \sum_{t=1}^{T}\sum_{n=1}^{N_{BESS}}\underbrace{\left(P_t^{BC}.\beta_{CC} + P_t^{BD}.\beta_{DC}\right)}_{cost}.t \qquad \forall t,n \tag{20}$$

where C_{GC} and C_{BC} are grid and BESS operational costs, respectively. P_t^{GB} and P_t^{GS} are power bought from grid and power sold to grid. λ_t^{pp} and λ_t^{SP} are the buying and selling price electricity. β_{CC} and β_{DC} are the charged and discharged degradation cost of BESS, respectively.

B. Constraints

1) Power Balance Constraint

The power balance equation is given in (21):

$$P_t^{GB} - P_t^{GS} - \sum_{n=1}^{N_{BESS}} P_t^{BC} + \sum_{n=1}^{N_{BESS}} P_t^{BD} + \sum_{n=1}^{N_{PV}} P_t^{PV} = \sum_{Load} P_{i,t}^{Load} + \sum_{Loss} P_{ij,t}^{loss} \qquad \forall t,i,j,n \tag{21}$$

where $\sum P_{i,t}^{Load}$ is equivalent to total active power at all buses at time t. Similarly, $\sum_{n=1}^{N_{BESS}} P_t^{BC}$ and $\sum_{n=1}^{N_{BESS}} P_t^{BD}$ mean sum of the charge and

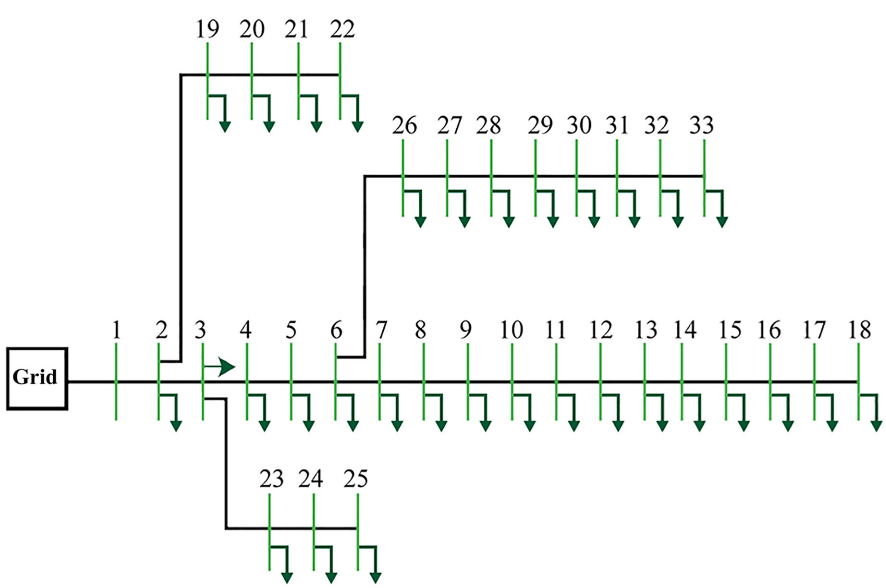

Fig. 4. IEEE 33 bus test system.

TABLE I.
COMPARISON OF BUS VOLTAGES OF DLF TECHNIQUE WITH OTHER POWER FLOW TECHNIQUES FOR IEEE-33 BUS TEST SYSTEM

Bus No.	DLF Method (p.u.)	Analytical Method (p.u.)[14]	Dynamic Data Matrix Method (p.u.) [29]	Direct Backward/ Forward Sweep Technique (p.u.) [30]
1	1.0	1.0000	1.0000	1.0000
2	0.9970	0.9970	0.9970	0.9970
3	0.9829	0.9829	0.9829	0.9829
4	0.9754	0.9754	0.9755	0.9754
5	0.9680	0.9680	0.9681	0.9679
6	0.9496	0.9496	0.9497	0.9494
7	0.9461	0.9461	0.9462	0.9459
8	0.9413	0.9412	0.9413	0.9322
9	0.9350	0.9350	0.9351	0.9259
10	0.9292	0.9292	0.9292	0.9200
11	0.9283	0.9283	0.9284	0.9192
12	0.9268	0.9268	0.9269	0.9177
13	0.9207	0.9207	0.9208	0.9115
14	0.9185	0.9185	0.9185	0.9092
15	0.9170	0.9171	0.9171	0.9078
16	0.9157	0.9157	0.9157	0.9064
17	0.9136	0.9137	0.9137	0.9043
18	0.9130	0.9131	0.9131	0.9037
19	0.9965	0.9965	0.9965	0.9964
20	0.9929	0.9929	0.9929	0.9929
21	0.9922	0.9922	0.9922	0.9922
22	0.9915	0.9916	0.9916	0.9915
23	0.9793	0.9793	0.9794	0.9792
24	0.9726	0.9727	0.9727	0.9726
25	0.9693	0.9693	0.9694	0.9692
26	0.9477	0.9477	0.9477	0.9475
27	0.9451	0.9451	0.9452	0.9449
28	0.9337	0.9338	0.9337	0.9335
29	0.9255	0.9256	0.9255	0.9253
30	0.9219	0.9220	0.9220	0.9217
31	0.9177	0.9178	0.9178	0.9175
32	0.9168	0.9169	0.9169	0.9166
33	0.9165	0.9166	0.9166	0.9163

DLF, distribution load flow.

TABLE II.
SUMMARY OF POWER LOSS RESULTS FOR DIFFERENT METHODS

Method	Total Active Power Loss (kW)
DLF method	202.677
The new analytical formulation [14]	202.771
Dynamic data matrix method [29]	202.7
The direct backward/forward sweep technique [30]	211

DLF, distribution load flow.

discharge power for all BESS, respectively. $\sum_{n=1}^{N_{PV}} P_t^{PV}$ defines the sum of generated power by all PV panels.

Battery energy storage systems have different efficiencies in charging and discharging modes. Therefore, discharge and charge powers are modeled as separate variables.

2) BESS Constraint

The charging/discharging processes of BESS simultaneously are prevented by using (22).

$$P_t^{BC}.P_t^{BD} = 0 \qquad \forall t \tag{22}$$

The state of charge (SoC) of a battery is its available capacity expressed as a percentage of its rated capacity.

$$SoC^{min} \le SoC_t^{BESS} \le SoC^{max} \qquad \forall t \tag{23}$$

where SoC^{min} and SoC^{max} are the lower and upper permissible SoC limits. In this study, SoC was determined as 20% lower limit and 80% upper limit.

3) Buying and Selling Constraint

An MG is prevented buying and selling electricity simultaneously at each time step by using (24).

$$P_t^{GB}.P_t^{GS} = 0 \qquad \forall t \tag{24}$$

4) Voltage Constraints

The bus voltages at each bus is bound by a specified lower and upper limit by (25).

$$V_i^{min} \le V_{i,t} \le V_i^{max} \qquad \forall t,i \tag{25}$$

V_i^{min} and V_i^{max} mean lower/upper permissible voltage limits.

The lower and upper voltage limits which are set at 0.9 p.u. and 1.1 p.u., respectively as follows: (26).

$$0.90(p.u) \le V_{i,t} \le 1.1(p.u) \qquad \forall t,i \tag{26}$$

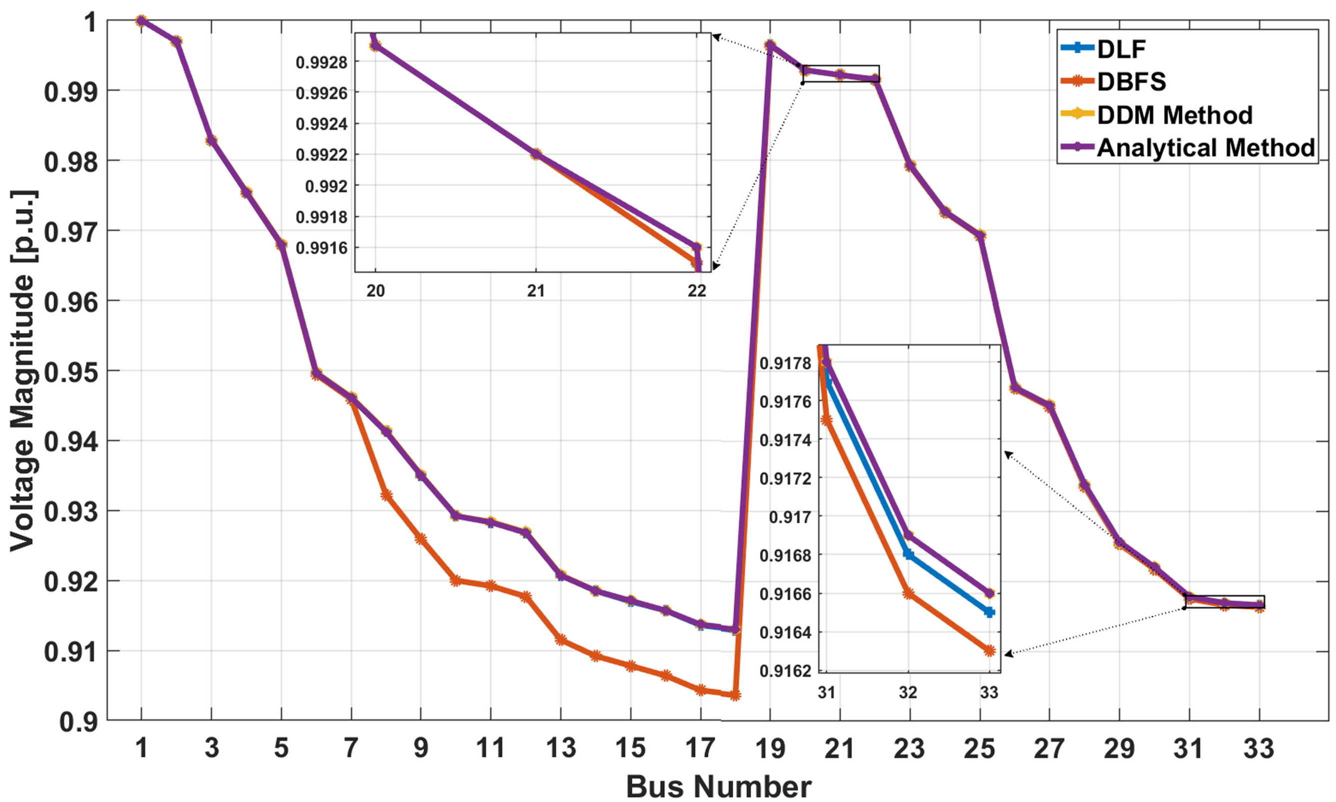

Fig. 5. Comparison of voltages at each bus for different power flow methods.

The final optimization problem takes the form as follows:

$$min\ F = \sum_{t=1}^{T}\left(\sum_{n=1}^{N_{BESS}}\left(P_t^{GB}.\lambda_t^{pp} - P_t^{GS}.\lambda_t^{SP} + P_t^{BC}.\beta_{CC} + P_t^{BD}.\beta_{DC}\right)\right).t \qquad \forall t,n \tag{27}$$

subject to (2)–(4) and (21)–(26).

The aim of this paper is to reduce the cost of energy bought from the grid and the operating costs of the BESSs and also to increase the energy sales to the grid.

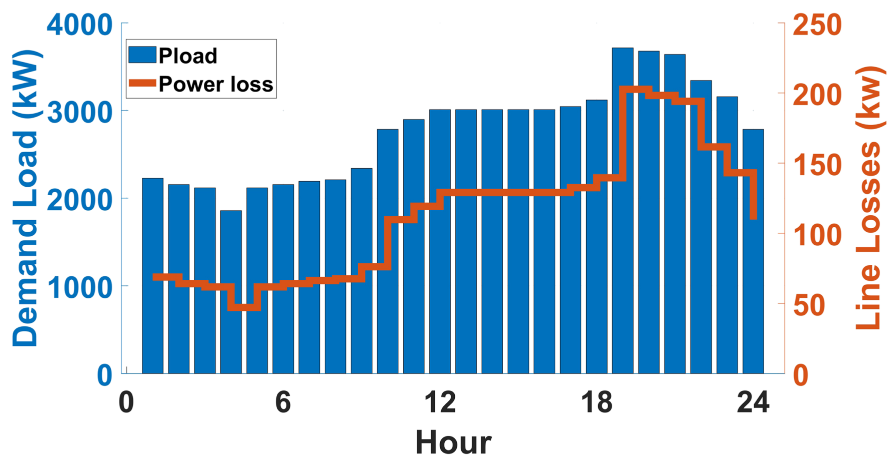

Fig. 6. Twenty-four-hour load profile and base case line losses.

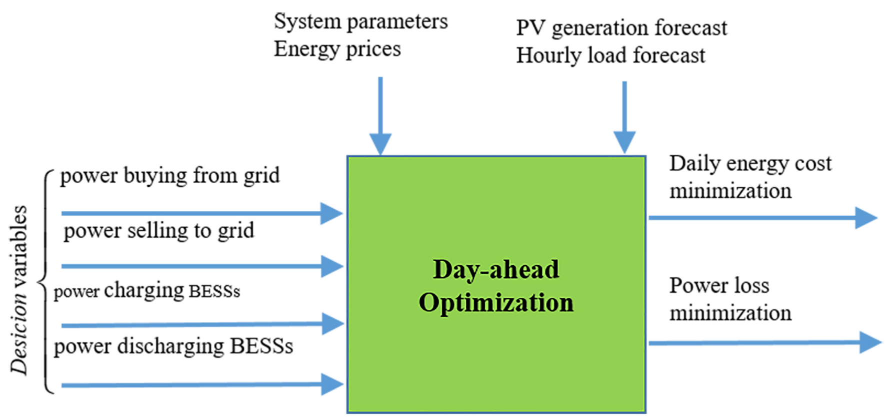

Fig. 7. Input–output scheme.

The last term (P_{Loss}) of the power balance equation given in (21) is obtained from PFC. Power flow calculation includes the set of nonlinear equations. Thus, the proposed day-ahead EMS scheduling transforms to a nonlinear optimization problem.

V. SIMULATION STUDIES AND RESULTS

A. System Configuration

The study aims at the lowest cost of energy by integrating PV and BESS in the test system. Moreover, revenues can be increased through more PV generations. Battery energy storage systems contribute to revenues or lower expense for buying energy from grid when the market prices are volatile. The modified test system in [32] is depicted in Fig. 8.

Photovoltaics and BESS parameters are shown in Table III and IV.

The proposed approach requires the forecast data of the loads, PV generations, and the spot price data of the grid. This study assumes that the PV generation forecasted by historical data is available for EMS. The placement problem of PV and BESS is beyond the scope of this paper, because we focus on the optimal operating of MG.

Fig. 9 illustrates the electrical energy price of buying and selling in day-ahead spot market.

The hourly variation of the power to be generated by the PV panels used in the day-ahead EMS and the total active power demand are demonstrated in Fig. 10.

B. Simulation Results

To assess practically the effects of integrating PV and BESS into the IEEE 33 bus test system, PV and BESS should be integrated separately.

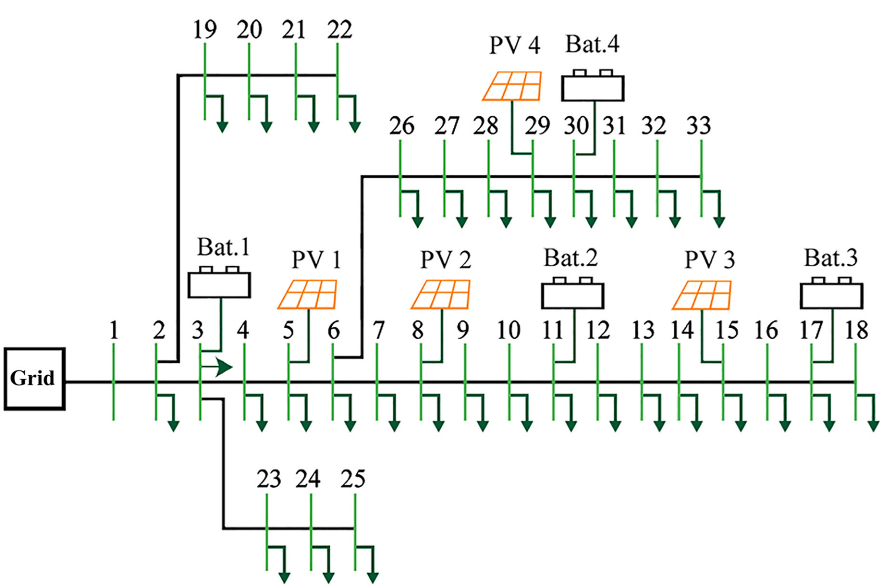

Fig. 8. IEEE 33 bus test system (modified from [33]).

TABLE III.
BESS PARAMETERS

Equipment	Location	Maximum Power (MW) [34] $(P^{BC,max}, P^{BD,max})$	Maximum Capacity (MWh) [34] (SoC)	Charge Efficiency (η_{BC}) [15]	Discharge Efficiency (η_{BD}) [15]	Degradation Cost (\$/kWh) (β_{CC}, β_{DC}) [15]
BESS-1	Bus 3	2	2	0.95	0.90	0.042
BESS-2	Bus 11	1	1	0.95	0.90	0.042
BESS-3	Bus 17	1	1	0.95	0.90	0.042
BESS-4	Bus 30	2	2	0.95	0.90	0.042

BESS, battery energy storage system.

Therefore, only PVs are integrated first, and then only BESSs are integrated and finally both PVs and BESSs are integrated simultaneously the last.

Case 1: Only PVs are integrated,

Case 2: Only BESSs are integrated,

Case 3: Both PVs and BESSs are integrated.

Nonlinear programming solver, MATLAB's fmincon solver, was used for finding the minimum of the nonlinear optimization problem in the case studies simulations.

1) Case 1
The demanded power by the load was supplied from both PV and grid instead of only from grid. The cost of energy was calculated as \$3761. Thus, the cost was reduced to approximately 56% compared to the base case. Moreover, the daily energy loss was calculated as 2442 kWh. Hence, approximately 10% daily energy loss reduction was achieved when compared with the base case.

2) Case 2
Only the BESSs were integrated in the system, and the cost of energy for 1 day was calculated as \$8507. This shows a reduction of 2% in the cost of energy compared to the base case. Furthermore, the energy loss was calculated as 2628 kWh, with a decrease of 4% compared to the base case.

TABLE IV.
PV GENERATION SYSTEM PARAMETERS

Equipments	Location	Rated Power (MW) (P_r^{PV})	Panel Area (m²) (A_{pv})	Panel Efficiency (η_{pv})
PV-1	Bus 5	1	5000	0.20
PV-2	Bus 8	0.8	4000	0.20
PV-3	Bus 15	1.2	6000	0.20
PV-4	Bus 29	1.4	7000	0.20

PV, photovoltaic.

3) Case 3
In the last case, by integrating both the PVs and the BESSs into the MG, the cost of energy was obtained as \$3646, which resulted in an energy cost advantage of approximately 58%.

The results described above are that the objective function is to minimize the cost of energy. Different case studies, such as by integrating only PVs, only BESSs, and both PVs and BESSs into the test system, are carried out to investigate the effects of the aim of objective function in each case on the cost of energy and the energy loss in order to reveal the differences of the costs and the losses. To summarize

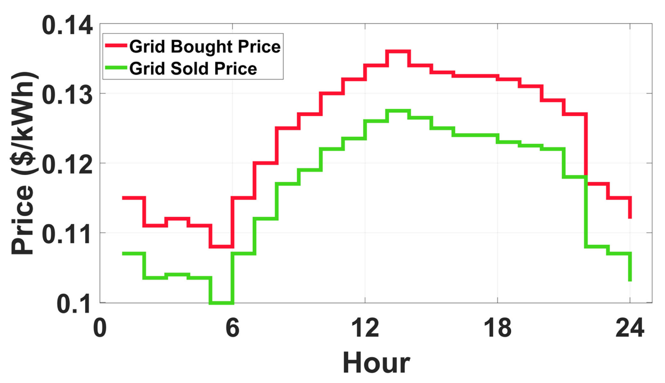

Fig. 9. Day-ahead purchase and sales electricity prices [12].

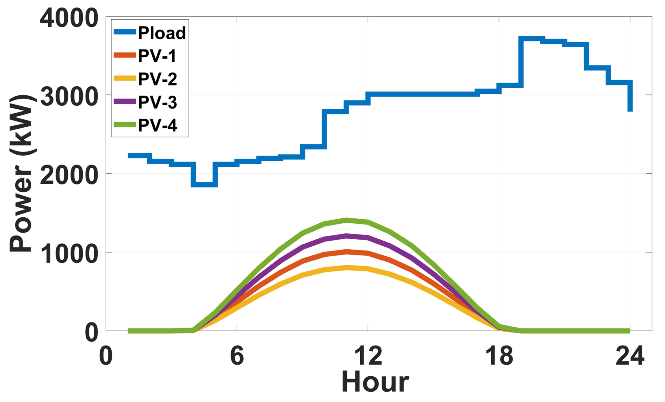

Fig. 10. Load [32] and PV power [34] profile.

TABLE V.
COMPARISON OF CASE STUDIES RESULTS

Outputs	Base Case		Case 1		Case 2		Case 3	
	OF-1	OF-2	OF-1	OF-2	OF-1	OF-2	OF-1	OF-2
Cost ($)	8660	8660	3761	3761	8507	8566	3646	3938
Losses (kWh)	2733	2733	2442	2442	2628	2606	2312	1955
Time (s)	25	34	35	23	1058	931	864	728

OF-1, the objective function is to determine cost; OF-2, the objective function is to determine energy loss.

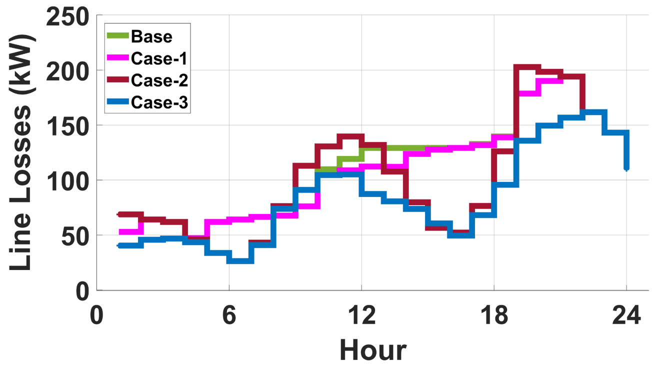

Fig. 11. Hourly variation of total line losses.

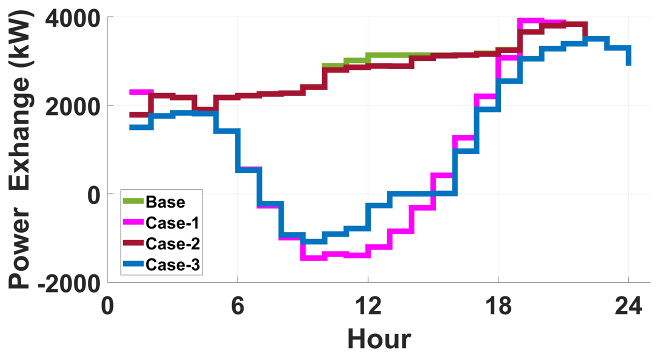

Fig. 12. The comparison of power exchange to grid.

briefly, it is simulated with two different objective functions: the objective function is to determine cost (OF-1) and the objective function is to determine energy loss (OF-2). The simulation results of different objective functions are given separately in Table V.

In case 2, the energy loss was calculated as 2606 kWh in the case whose objective function was to minimize energy loss, while energy loss was 2628 kWh in the case whose objective function was to minimize the energy cost. Here, an important feature is that energy loss can change according to the objective function. Moreover, the cost of energy was decreased from $8566 to $8507 compared to the objective function which was to minimize the energy loss. This implies to supply energy from the BESS instead of of purchase energy the grid, which increases more line loss. The demand loads are supplied by the BESS in order to minimize the energy cost.

Similarly, in case 3, although the energy loss increased, the total energy cost was calculated as lower when the objective function was

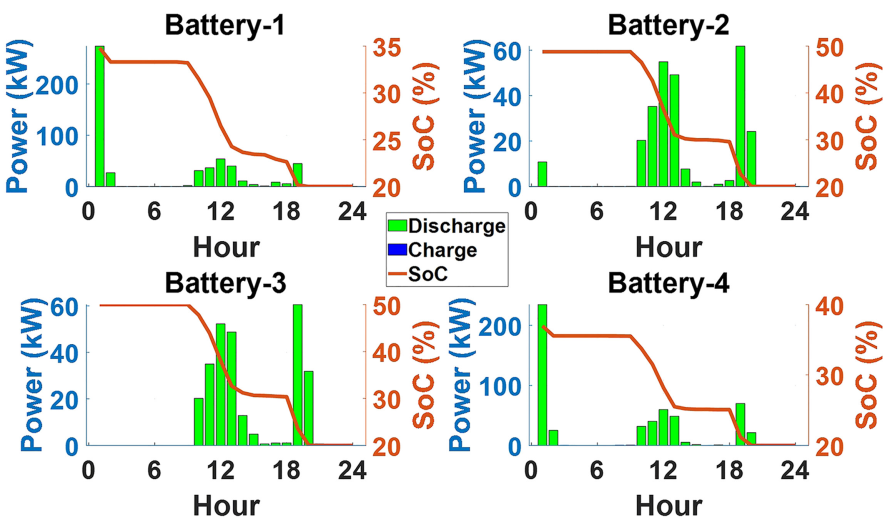

Fig. 13. Battery energy storage system power and SoC at case 2.

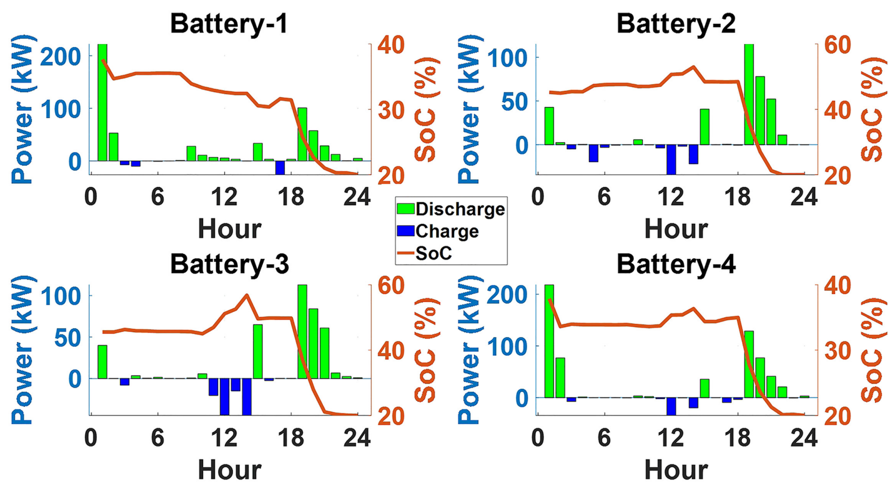

Fig. 14. Battery energy storage system power and SoC at case 3.

to minimize the energy cost. All analyses in the following parts of the study have been considered as objective function to minimize the cost of energy. Figs 11 and 12 give the line losses and energy exchange with grid according to the cases, respectively.

Fig. 13 illustrates the charge/discharge power and also SoC of the BESS in case 2.

The demand loads were supplied from the BESSs in order to get the highest profits when purchase prices are highest. Similarly, when the load was at the peak level, the loads were supplied by BESS; thus, the cost of energy was reduced. Battery energy storage systems discharged power until SoC reached 20%, which was the lower energy limit of BESS.

The powers and SoC of BESSs are seen in case 3 in Fig. 14. The BESSs kept a large amount of its energy until the evening when the load and market price were high. The BESSs discharged power until they emptied own energies.

The bus voltages given in Fig. 15 are obtained by solving the PFC according to the case studies.

Because the buses 6, 13, and 31 were near the PV system, the voltage fluctuation was caused by the PV power. Therefore, it was seen that bus voltage fluctuation was very high compared to the other buses.

Rise in bus voltage profiles in case 1 and case 3 were observed at noon by considering the generation of PV after integrating the PV to test system. The bus voltage magnitudes in case 3 were less than that in case 2 due to decreasing bus voltages because of the BESS in charging mode acting like a load. Voltage magnitudes at the specified buses were improved with BESS integration. Improvement in bus voltages at nearly all buses can be seen in case 2 compared to the base case especially around noon. The BESS injected the power into MG instead of buying from the grid, improving the voltage level due to the high energy price of purchase from the grid. Minimum bus voltage deviation was seen at bus 22 due to the fact that there is not any integration of PV or BESS between bus 22 and the grid bus.

C. Sensitivity Analysis

A comprehensive sensitivity analysis is performed to assess the robustness and sensitivity of the system. Solar irradiation is an important parameter that affects the cost of energy. The solar irradiation is historical data for the period from January 1, 2006, to December 31, 2006, in İzmir/ Turkey (38.471N, 27.169E) for

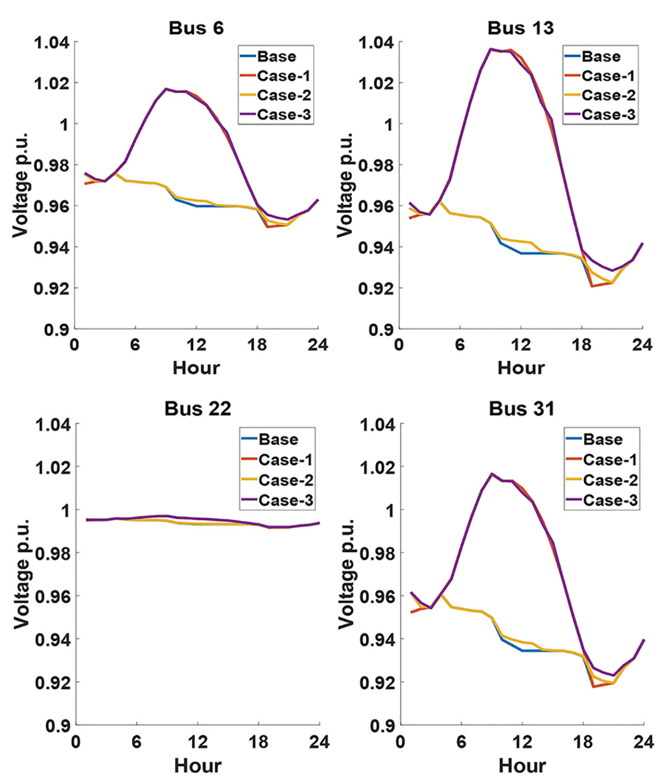

Fig. 15. Bus 6, 13, 22 and 31 voltage profile according to case studies.

sensitivity analysis [33]. Fig. 16 shows the solar energy profile illustrating the amount of solar radiation in different days of a year for the selected location. It is evident that on the summer days, there is more solar irradiance than on the winter days. This difference affects the cost of energy.

To evaluate this parameter, the modified system was modeled and simulated based on the values of the daily weather data, which implies the best and worst weather conditions like the cloudy winter and clear summer days.

The cost of energy and the power loss are given in Table VI, which are obtained from the simulation results for the modified IEEE 33 bus test system.

The cost of energy was calculated as the lowest level since PV generation was at maximum levels on a clear summer day, which was the day with the highest irradiance. On the other hand, the lowest irradiance day, which was a partially cloudy winter, was calculated as the highest energy cost. With regard to energy loss, the highest energy loss was calculated on a partially cloudy winter day, while the lowest energy loss was calculated on a partially cloudy summer day.

TABLE VI.
COMPARISON OF ENERGY COST AND LOST ENERGY FOR DIFFERENT DAYS

Types of Day	Cost ($)	Energy Loss (kWh)
Clear summer	3646	2312
Clear winter	6970	2163
Partially cloudy summer	4727	2255
Partially cloudy winter	7449	2246

Other important factors affecting the cost of energy and the power loss are electricity price, PV capacity powers, and degradation costs.

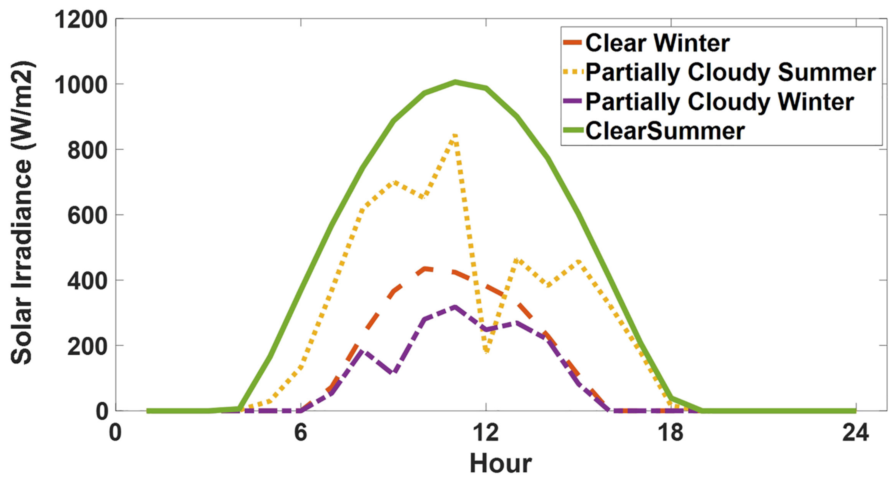

Fig. 16. Solar irradiance for four selected days.

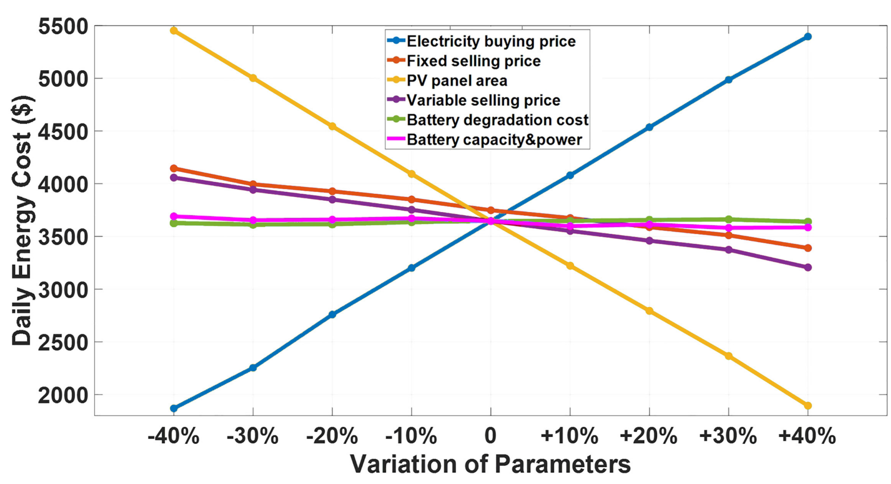

Fig. 17. Daily energy cost versus variation of parameters.

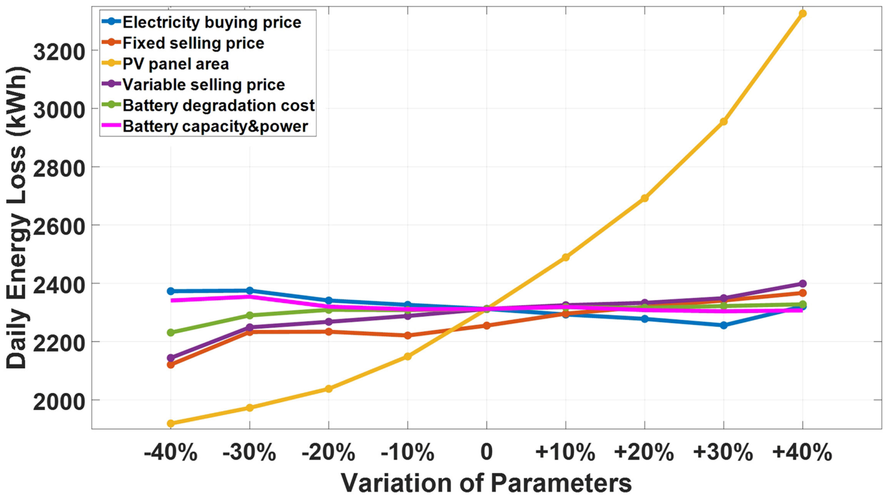

Fig. 18. Daily energy loss versus variation of parameters.

The day-ahead EMS uses electricity purchase price, electricity variable/fixed selling price, PV panel area, BESS degradation cost, BESS capacity, and power for six different sensitivity cases.

Figs 17 and 18 show the sensitivity analysis results of the daily cost of energy and the daily energy loss. The fixed selling price means that the feed-in rate is assumed as 0.11$/kWh for the entire day.

This sensitivity analysis was performed with the system configuration specified in case 3 and on a clear summer day. The results reveal that two most important parameters affecting the daily energy cost are electricity purchase price and the energy generated by PV panels.

As anticipated, the daily energy cost becomes lower as the fixed and variable selling prices increase. It is seen that the capacity, the power, and the degradation cost of the BESS are the parameters that affect the daily energy cost the least.

In terms of daily energy loss, an increase in the area of PV panels, which means an increase in the amount of energy generated by PV panel, increases the energy loss. When the electricity sales prices increased, the loss of energy increased slightly due to a slight increase in the sales to the grid. Because of the increase in the price of the energy bought from the grid, the amount of energy bought from the grid reduced. So, the energy loss decreased.

VI. CONCLUSION

The increase in the diversity of DG resources and in the number of equipment used, such as BESSs and PV systems, complicates the problem that needs to be solved in the day-ahead EMS. Energy management system is the practical way of decreasing the cost of energy and ensuring the technical limits of MG. With the nonlinear equation, sets were formulated in this study and by means of these formulations, EMS scheduling problem was solved for a base IEEE 33 bus test system. Then, case studies were carried out by creating a system with the addition of only PVs to the system. Later, only BESSs and finally both PVs and BESS were integrated into the MG.

The analyses in which the energy costs of the objective functions were minimized and in which the energy losses were minimized in four different case studies were made. It showed that the hybrid system configuration in which PV and BESS integrated to MG is the the lowest cost system configuration in terms of daily cost of energy and line loss. Moreover, the addition of BESS provided advantage on the cost and energy loss as well as improvements in the voltage profile. Then, the energy cost and energy loss were calculated on cloudy or non-cloudy days in summer and winter months using the realistic data of different irradiance.

As expected, the lowest energy cost was calculated during the clear summer day, whereas the highest energy cost was calculated on a cloudy winter day. In the sensitivity analysis, it was seen that the most impact on the daily energy cost was the cost of purchasing electricity and the PV panel area. Similarly, it was evaluated that the parameter affecting the energy loss the most was the PV panel area.

Peer-review: Externally peer-reviewed.

Declaration of Interests: The authors declare that they have no competing interest.

Funding: This study received no funding.

REFERENCES

1. REN21, *Renewables 2022 Global Status*. Paris: REN21 Secretariat, 2022. ISBN 978-3-948393-04-5.
2. G. Pepermans, J. Driesen, D. Haeseldonckx, R. Belmans, and W. D'haeseleer, "Distributed generation: Definition, benefits and issues," *Energy Policy*, vol. 33, no. 6, pp. 787–798, 2005. [CrossRef]
3. M. Fathi, and H. Bevrani, "Statistical cooperative power dispatching in interconnected microgrids," *IEEE Trans. Sustain. Energy*, vol. 4, no. 3, pp. 586–593, 2013. [CrossRef]
4. K. P. Kumar, and B. Saravanan, "Day ahead scheduling of generation and storage in a microgrid considering demand Side management," *J. Energy Storage*, vol. 21, pp. 78–86, 2019. [CrossRef]

5. J. A. Martinez, and J. Mahseredjian, "Load flow calculations in distribution systems with distributed resources. A review," in 2011 IEEE Power and Energy Society General Meeting, pp. 1–8, 2011. [CrossRef]
6. B. V. S. Vardhan, M. Khedkar, and I. Srivastava, "Effective energy management and cost effective day ahead scheduling for distribution system with dynamic market participants," *Sustain. Energy Grids Netw.*, vol. 31, p. 100706, 2022. [CrossRef]
7. M. Rahimi, F. J. Ardakani, O. Olatujoye, and A. J. Ardakani, "Two-stage interval scheduling of virtual power plant in day-ahead and real-time markets considering compressed air energy storage wind turbine," *J. Energy Storage*, vol. 45, p. 103599, 2022. [CrossRef]
8. G. Huang, H. Wu, Z. Feng, Y. Ding, and J. Wang, "Day-ahead reactive-voltage optimization for active distribution network with energy storage," in 2021 3rd International Conference on Electrical Engineering and Control. Technologies (CEECT), 2021, pp. 170–174. [CrossRef]
9. X. Sun, J. Qiu, Y. Yi, and Y. Tao, "Cost-effective coordinated voltage control in active distribution networks with photovoltaics and mobile energy storage systems," *IEEE Trans. Sustain. Energy*, vol. 13, no. 1, pp. 501–513, 2022. [CrossRef]
10. J. H. Teng, "A direct approach for distribution system load flow solutions," *IEEE Trans. Power Deliv.*, vol. 18, no. 3, pp. 882–887, 2003. [CrossRef]
11. V. Vita, "Development of a decision-making algorithm for the optimum size and placement of distributed generation units in distribution networks," *Energies*, vol. 10, no. 9, p. 1433, 2017. [CrossRef]
12. F. H. Aghdam, N. T. Kalantari, and B. Mohammadi-Ivatloo, "A chance-constrained energy management in multi-microgrid systems considering degradation cost of energy storage elements," *J. Energy Storage*, vol. 29, p. 101416, 2020. [CrossRef]
13. A. Waqar *et al.*, "Analysis of optimal deployment of several DGs in distribution networks using plant propagation algorithm," *IEEE Access*, vol. 8, pp. 175546–175562, 2020. [CrossRef]
14. R. Srinivasa Rao, S. V. L. Narasimham, M. Ramalinga Raju, and A. Srinivasa Rao, "Optimal network reconfiguration of large-scale distribution system using harmony search algorithm," *IEEE Trans. Power Syst.*, vol. 26, no. 3, pp. 1080–1088, 2011.
15. H. A. Taha, M. H. Alham, and H. K. M. Youssef, "Multi-objective optimization for optimal allocation and coordination of wind and solar DGs, BESSs and capacitors in presence of demand response," *IEEE Access*, vol. 10, pp. 16225–16241, 2022. [CrossRef]
16. U. Sur, "Impact study of distributed generations in voltage sag mitigation using an improved three-phase unbalanced load flow for active distribution network," *Turk. J. Electr. Power Energy Syst.*, vol. 2, no. 2, pp. 124–133, 2022. [CrossRef]
17. S. Gupta, V. K. Yadav, and M. Singh, "Optimal allocation of capacitors in radial distribution networks using Shannon's entropy," *IEEE Trans. Power Deliv.*, vol. 37, no. 3, pp. 2245–2255, 2022. [CrossRef]
18. S. Koohi-Fayegh, and M. A. Rosen, "A review of energy storage types, applications and recent developments," *J. Energy Storage*, vol. 27, p. 101047, 2020. [CrossRef]
19. S. Bacha, D. Picault, B. Burger, I. Etxeberria-Otadui, and J. Martins, "Photovoltaics in microgrids: An overview of grid integration and energy management aspects," *IEEE Ind. Electron. Mag.*, vol. 9, no. 1, pp. 33–46, 2015. [CrossRef]
20. S. Polat, E. Bıyık, and H. Şekerci Öztura, "Batarya ve PV Sistemi İçeren Bir Mikro Şebekenin Gün Öncesi Enerji Yönetim Sistemi ile Optimum İşletilmesi," in CIGRE Türkiye - III. Power Systems Conference, GSK 2022. Ankara, 2022.
21. D. T. Ton, and M. A. Smith, "The U.S. Department of Energy's microgrid initiative," *Electr. J.*, vol. 25, no. 8, pp. 84–94, 2012. [CrossRef]
22. "Microgrids State working group | NASEO." [Online]. Available: https://www.naseo.org/issues/electricity/microgrids. [Accessed: December 9, 2022].
23. A. Dolara, S. Leva, and G. Manzolini, "Comparison of different physical models for PV power output prediction," *Sol. Energy*, vol. 119, pp. 83–99, 2015. [CrossRef]
24. T. Ma, H. Yang, and L. Lu, "Solar photovoltaic system modeling and performance prediction," *Renew. Sustain. Energy Rev.*, vol. 36, pp. 304–315, 2014. [CrossRef]
25. M. R. B. Khan, R. Jidin, and J. Pasupuleti, "Multi-agent based distributed control architecture for microgrid energy management and optimization," *Energy Convers. Manag.*, vol. 112, pp. 288–307, 2016. [CrossRef]
26. S. Cao, H. Zhang, K. Cao, M. Chen, Y. Wu, and S. Zhou, "Day-ahead economic optimal dispatch of microgrid cluster considering shared energy storage system and P2P transaction," *Front. Energy Res.*, vol. 9, 2021. [CrossRef]
27. K. Prakash, and M. Sydulu, "Topological and primitive impedance based load flow method for radial and weakly meshed distribution systems," *Iran. J. Electr. Comput. Eng.*, vol. 10, no. 1, pp. 10–18, 2011.
28. T. Thakur, and J. Dhiman, "A new approach to load flow solutions for radial distribution system," in 2006 IEEE PES Transmission and Distribution Conference and Exposition: Latin America, TDC'06, pp. 1–6, 2006. [CrossRef]
29. M. V. Kirthiga, S. A. Daniel, and S. Gurunathan, "A methodology for transforming an existing distribution network into a sustainable autonomous micro-grid," *IEEE Trans. Sustain. Energy*, vol. 4, no. 1, pp. 31–41, 2013. [CrossRef]
30. W. A. Vasquez, and F. L. Quilumba, "Load flow method for radial distribution systems with distributed generation using a dynamic data matrix," 2016 IEEE Ecuador Technical Chapters Meeting, ETCM 2016, pp. 16–20, 2016. [CrossRef]
31. G. Diaz, J. Gomez-Aleixandre, and J. Coto, "Direct backward/forward sweep algorithm for solving load power flows in AC droop-regulated microgrids," *IEEE Trans. Smart Grid*, vol. 7, no. 5, pp. 2208–2217, 2016. [CrossRef]
32. T. Tewari, A. Mohapatra, and S. Anand, "Coordinated control of OLTC and energy storage for voltage regulation in distribution network with high PV penetration," *IEEE Trans. Sustain. Energy*, vol. 12, no. 1, pp. 262–272, 2021. [CrossRef]
33. X. Li, L. Wang, N. Yan, and R. Ma, "Cooperative dispatch of distributed energy storage in distribution network with PV generation systems," *IEEE Trans. Appl. Supercond.*, vol. 31, no. 8, pp. 1–4, 2021. [CrossRef]
34. "JRC Photovoltaic Geographical Information System (PVGIS) - European Commission." [Online]. Available: https://re.jrc.ec.europa.eu/pvg_tools/en/#api_5.2. [Accessed: December 2, 2022].